IntechOpen

Advanced Engineering Testing

Edited by Aidy Ali

ADVANCED ENGINEERING TESTING

Edited by **Aidy Ali**

Advanced Engineering Testing
http://dx.doi.org/10.5772/intechopen.74186
Edited by Aidy Ali

Contributors

Alessandro Grazzini, Turbadrakh Chuluunbat, Andrii Kostryzhev, Dakeshwar Verma, Jonathan Becedas, Andrés Caparrós, Pablo Morillo, Antonio Ramírez, Esther Sarachaga, Almudena Martín-Moreno, Muzamal Hussain, Muhammad Nawaz Naeem

Notice

First published in London, United Kingdom, 2018 by IntechOpen
eBook (PDF) Published by IntechOpen, 2019
IntechOpen is the global imprint of INTECHOPEN LIMITED, registered in England and Wales, registration number: 11086078, The Shard, 25th floor, 32 London Bridge Street
London, SE19SG – United Kingdom
Printed in Croatia

British Library Cataloguing-in-Publication Data
A catalogue record for this book is available from the British Library

Additional hard and PDF copies can be obtained from orders@intechopen.com

Advanced Engineering Testing
Edited by Aidy Ali

p. cm.

Print ISBN 978-1-78984-243-2

Online ISBN 978-1-78984-244-9

eBook (PDF) ISBN 978-1-83881-780-0

Meet the editor

Aidy Ali is a Professor of Mechanical Engineering at the National Defence University of Malaysia (NDUM), known as Universiti Pertahanan Nasional Malaysia (UPNM). He received his first degree in Mechanical Engineering from Universiti Putra Malaysia, 1999. He then pursued his PhD degree in 2003 researching the improvement of fatigue life of aircraft components by using surface engineering at Sheffield University. He was then appointed as lecturer at Universiti Putra Malaysia in 2006 and was rapidly promoted to senior lecturer in 2008, Associate Professor in 2010 and Professor in 2012, all within 6 years. Professor Aidy has more than 18 years of experience in research and teaching in the field of mechanical engineering especially in Mechanical Fatigue and Fracture of Materials. He has published more than 140 articles in scopus and ISI indexed journals , 20 books, and has secured more than 24 research grants. He has graduated 16 PhD students, 38 master students and 31 bachelor students. His expertise is related to mechanical materials for defence applications, fatigue, fracture of materials, failure assessment, failure prevention analysis, reliability engineering prediction and crash analysis.

Contents

Preface

Advanced Engineering Testing is the technology and engineering achievement that includes services to all users in determining the structural integrity of a product. Most companies that provide world class technical innovation, engineering, testing and manufacturing services to deliver energy-efficient performance to customers require knowledge in fundamental testing. The capabilities of Advanced Engineering Testing provides ideas in new materials, electrification and battery technology, aerodynamics and thermodynamics, business performance and specialist low volume manufacturing, which is applicable across all sectors, from automotive and motorsport to aerospace and defence or energy and sports science to healthcare.

Engineers and scientists must work in close collaboration with their prospective users or customers to help them meet the engineering challenges of the 21st century, which are mobility, sustainability and efficiency. Engineering testing has gradually become the crucial method in determining whether or not the engineering components or machine are safe and reliable. The cost to redesign and retest the engineering products give designers, engineers and manufactures an alarming sign whether or not to keep the existing testing method, redesign the test method, or to use a different or advanced apparatus with advanced formulations.

This book covers recent advances in the method used in testing especially in the case of structural integrity that includes fatigue and fracture testing, vibrations testing and surface engineering testing that are crucial and widely used by engineers and industries.

The book will take the reader on a tour of how to apply the advanced formulation, advanced theory and advanced method of testing that are relevant to all engineering fields: mechanical, electrical, civil, materials and surface engineering. The topics are explained comprehensively with the reliable test being performed in order to effectively investigate the strength and validation of the development theory or model. The first part of the book focuses on how to perform fatigue and fracture tests. The second part of the book focuses on how the vibration tests are carried out. The last part of the book focuses on how to perform the surface analysis test.

I hope the material is not too theoretical and that the reader finds the case study, the formulation, the testing method, and the analysis helpful in tackling their own engineering and science-based studies. Last but not least, I would like to thank all of the authors who contributed to and supported the production of this book.

Prof. Dr. Aidy Ali
Department of Mechanical Engineering
Faculty of Engineering
National Defence University of Malaysia (NDUM)
Universiti Pertahanan Nasional Malaysia (UPNM)

Section 1

Fatigue and Fracture Advanced Testing

Chapter 1

Experimental Fatigue Test for Pre-Qualification of Repair Mortars Applied to Historical Masonry

Alessandro Grazzini

Additional information is available at the end of the chapter

http://dx.doi.org/10.5772/intechopen.79543

Abstract

Restoration work on historical masonry buildings requires new repair materials capable of providing adequate durability over time. The interface between strengthening mortar and historical masonry can be the site of various stresses due to mechanical and thermo-hygrometric actions, also causing delamination actions. At the Non-Destructive Testing Laboratory of the Politecnico di Torino, an experimental methodology has been developed through static, freezing-thawing and cyclic tests on mixed mortar-bricks specimens. The aim of the laboratory tests was to select a durable and compatible repair mortar before the application. Fatigue tests simulated all main stresses that can be generated at the interface between repair mortar and original masonry, both mechanical and thermo-hygrometric aspects. The experimental results were interpreted by evaluating the variation of deformation parameters over time during the tests. From a range of four strengthening mortars, the experimental procedure was able to select the one with the greatest guarantees of durability and compatibility. A similar experimental procedure has also been developed to test the durability of dehumidified mortars suitable for the recovery of historical plasters subjected by rising dump effects. The same selected mortars have been used successfully at prestigious restoration sites, demonstrating their validity over time.

Keywords: strengthening mortars, historical masonry, durability, fatigue test, plaster detachment

1. Introduction

The architectural heritage requires significant recovery and strengthening work due to the high degradation to which it was abandoned. In particular, historical buildings present a lot of damage caused by mechanical stresses (seismic actions, structural failures, overloads) and

thermo-hygrometric stresses (freezing-thawing cycles, rising dump effects) that have reduced the masonry strength. Often the refurbishment projects require historical buildings to change their intended use with necessary structural retrofit. This study aims to focus on the use of structural mortars, useful both in the field of strengthening work (reinforced plasters, reinforcement of vaults, grout injections in the masonry textures) and in the restoration work (dehumidified plasters). The choice of new strengthening products must pay attention to their compatibility of the mechanical characteristics compared to those of the original masonry structures, often very heterogeneous [1]. The market offers many types of structural mortars, some with high mechanical performance, of which only short-term resistance values are declared, but nothing is known about their durability when applied to very heterogeneous masonry structures.

The historical masonries have very different mechanical characteristics due to the variegated building textures and the specific degradation's level. Therefore, a single structural mortar cannot have the mechanical and thermo-hygrometric characteristics compatible with all diverse historical masonries. Unfortunately, some restoration works, carried out by high-performance cement mortars, have failed registering detachments of the strengthening products from the masonry supports.

Recent earthquakes have shown the clear failure of restoration work performed with the use of concrete materials, the excessive stiffness of which has completely distorted the original characteristics of historical masonry buildings. **Figure 1** shows the ineffectiveness of the cementitious insertion materials inside historical walls of the St. Agostino church, collapsed during the last great Italian earthquake of Amatrice, just in correspondence with the previous stitching made by cement injections.

In many instances, the strengthening work, performed with the parameters of modern technologies, has modeled the buildings through static schemes that are not suitable for old structures. They can produce a notable difference in mechanical performances compared to historical masonry, which can generate dangerous stresses to the interfaces among the materials. On the contrary, it is necessary to prefer the use of mortars based on hydraulic lime with mechanical characteristics similar to those of historical masonries. In addition, each wall texture deserves an ad hoc experimentation in order to evaluate, among a range of products offered by the market, which structural mortar has the most compatible mechanical and thermo-hygrometric characteristics, and therefore ensure greater durability of the intervention. Therefore, only the coupling between two materials with the same characteristics and similar elastic modulus will guarantee the mutual collaboration between the two materials, avoiding detachments.

At the Non-Destructive Testing Laboratory of the Politecnico di Torino, an experimental procedure was set up to select the new structural mortars and test their durability when applied to a specific historical masonry texture. The goal of this research is to show the fundamental importance of preliminary tests to identify the most compatible product for each specific restoration work. The procedure can be useful for the designer who needs to choose the best mortar, which guarantees durability over time when applied to a specific masonry structure. The tests are intended to simulate stresses under different mechanical and thermo-hygrometric actions that may occur in the useful life of the restored building. The tests are both static and cyclical, and start from single specimens to characterize the single material up to mixed

http://dx.doi.org/10.5772/intechopen.79543

Figure 1. Collapse of the St. Agostino church in Amatrice after the Central Italy earthquake 2016 (image courtesy of the Curia of Rieti).

mortar-brick specimens that have the function of simulating the real stresses that over time can undermine the structural binomial.

A first part of the tests concerns the validation of structural mortars for strengthening work, which must be carried out at the restoration site of the Royal Palace of Venaria. The second part concerns a similar methodology to test the adhesion of dehumidified plasters applied to historical masonry walls of the Sacro Monti di Varallo heritage site. Two important restoration sites have demonstrated over time the validity of the use of the repair mortars selected during the experimental procedure that will be described.

2. Validation of structural mortar for strengthening work at the Royal Palace of Venaria

The Royal Palace of Venaria, a UNESCO site near Turin, is one of the most famous monuments in Italy. His recovery project was among the most important in Europe (**Figure 2**). The restoration site has also been the place of experimentation with new techniques and materials for structural reinforcement methods. Within the restoration site, a research agreement was set up in collaboration with the Non-Destructive Testing Laboratory of the Politecnico di Torino, with the aim of validating the durability of the repair mortars used in subsequent strengthening and restoration work [2].

Figure 2. The Royal Palace of Venaria.

2.1. Experimental materials and setup

To determine the main mechanical characteristics of the individual materials, that is, the compressive strength and the elastic modulus, six specimens 40 × 40 × 160 mm were manufactured for each single material. Four different types of mortars were tested (codified as "A," "B," "C," "D"), suitable for the following restoration techniques: reinforcement by structural plaster (A; C), joint closing (A; D), jacketing of masonry walls or reinforcement of vaults (D), consolidation by grout injection (B). In addition to these, six more specimens 40 × 40 × 160 mm made from historic bricks of the Royal Palace of Venaria were tested (**Figure 3**). Each mortar test piece was labeled with "XM" where "X" stands for the code of the relative mortar (A–D); the brick test piece was labeled with "LT."

The next step of this experimental procedure was the manufacturing of particular mixed brick-mortar specimens measuring 223 × 57 × 83 mm (**Figure 4**). The mixed specimens were made from historical cut on which a 30 mm thick layer of strengthening mortar was applied. The brick surface was treated by means of a drill to facilitate the mortar's adhesion. The treatments simulate roughness and irregularity of the masonry surface that in the real executive

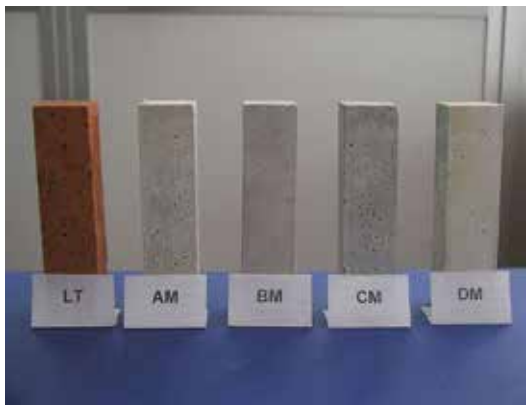

Figure 3. Single specimens.

http://dx.doi.org/10.5772/intechopen.79543

phases can improve the adhesion of strengthening plaster, or the irregular inside masonry texture that can improve the adhesion of a fluid injection mortar.

Each mixed test piece was labeled with "XL" where "X" stands for the code of the relative mortar (A–D).

Altogether eight mixed pieces were manufactured for each "XL" series: two for preliminary static tests, three for freezing-thawing tests and three for cyclic loading tests. The vertical and horizontal displacements were recorded respectively by means of a couple of vertical transducers and a horizontal transducer (**Figure 4**). The horizontal transducer served to measure the displacements due to bulging. The mixed specimens were instrumented also with a pair of electrical strain gauges on the opposing vertical faces measured transverse strains. In this manner, it is possible to measure the axial deformations (in vertical, horizontal and transverse directions), whose algebraic sum yields the volumetric deformation.

Cyclic and static compressive tests were carried out by means of a 250 kN model 810 MTS. Freezing-thawing cycles were performed through a laboratory oven and a refrigerator cell.

2.2. Mechanical and thermo-hygrometric characteristics of single materials

The results of static tests on single materials are shown in **Table 1**. Because of a technical hitch in the number of manufactured specimens, only for mortar B and D, the evolution of

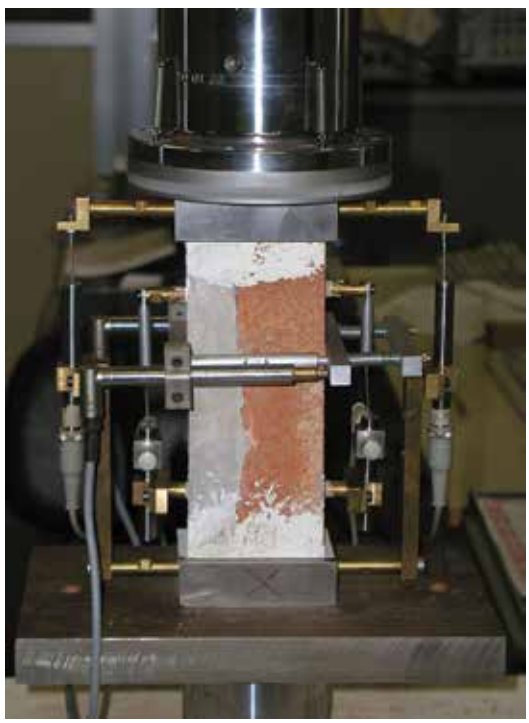

Figure 4. Mixed brick-mortar test pieces.

mechanical characteristics in the time due to the maturation effects has been analyzed, verifying that the changes in mechanical behavior are remarkable (**Tables 2** and **3**).

The analysis of the effects of the adverse environmental conditions (seasonal temperature ranges) was carried out by freezing-thawing tests on mortars B and D specimens (**Table 4**). None of the test piece B remained intact to reach the minimum threshold of 25 cycles. On the contrary, mortar D after 25 cycles showed a significant increase in resistance (+34.27%). After 50 cycles, there is a decrease in compressive strength again, bringing the average values close to the virgin reference (−3.12%). The reason for these substantial changes in mechanical properties may be due to thermal changes in the chemical base of the product [3]. However, these changes are very important and must be taken into account in the durability of the strengthening materials over time. These experimental results demonstrate the need to perform fatigue tests on repair materials before their use. A strong change in the mechanical characteristics of the strengthening materials can make it over time incompatible with the mechanical performance of the historical masonries on which it has been applied, favoring its detachment.

2.3. Experimental results of mixed test pieces

Table 5 shows the main mechanical characteristics of mixed test specimens. The mechanical performances after 28 freezing-thawing cycles are shown in **Table 6**, observing a great increase of strength.

The main phase of this validation procedure was the cyclic tests. The high value selected for cyclic load (70% of static load) was designed to make the test severe enough despite the short duration in the time (1,00,000 cycles—1.3 Hz), and to highlight the potential of several indicators monitored over time. The evolution of the volumetric deformation of mixed pieces was analyzed. Its propensity to negative values (increase in volume) can reflect a lesser degree of collaboration between the two materials, or even their detachment at the interface.

The test setup was performed through four steps:

- initial 70% loading-unloading test (3 cycles);
- 70% cyclic test (1,00,000 cycles);
- final 70% loading-unloading test (1 cycle);
- postcyclic compression test to failure.

Materials	E (N/mm²)	ν	σ (N/mm²)	Δ% σ
Mortar A	6208	0.12	8.27	−7.50
Mortar B	7534	0.19	10.91	+111.55
Mortar C	12,678	0.23	10.34	+146.39
Mortar D	12,274	0.32	24.95	+57.47
Historical brick (LT)	4099	0.08	8.09	—

E = elastic modulus, ν = Poisson's coefficient, σ = failure stress, Δσ = variation of σ.

Table 1. Elastic modulus and compression results of individual materials (40 × 40 × 160 mm).

Test piece	Days	σ (N/mm²)	Δ% σ (28 days)	E (N/mm²)	Δ% E (28 days)
BM 4.1	28	12.38		7262	
BM 7.3	28	12.54		6960	
BM 9.3	28	11.32		7944	
Average	**28**	**12.08**	**—**	**7389**	**—**
BM 3.3	90	19.74		10,676	
BM 1.3	90	19.59		10,089	
BM 10.2	90	20.37		11,290	
Average	**90**	**19.90**	**+64.71**	**10,685**	**+44.62**
BM 2.2	150	17.24		8347	
BM 6.1	150	20.02		7923	
BM 6.2	150	20.22		9046	
Average	**150**	**19.16**	**+58.61**	**8439**	**+14.21**
BM 2.3	210	17.47		12,000	
BM 8.1	210	17.94		10,223	
BM 3.1	210	19.02		9680	
Average	**210**	**18.14**	**+50.16**	**10,634**	**+43.92**

σ = failure stress, E = elastic modulus, Aσ = variation of σ, ΔE = variation of E.

Table 2. Mechanical characteristics during maturation of strengthening mortar B.

In the curve of a cyclic fatigue test (**Figure 5**), it is possible to identify three distinct stages:

- Stage I: Deformations are seen to increase rapidly (accounting for approximately 10% of the service life of test piece);
- Stage II: Deformations increase gradually at a virtually constant stress (10–80% of test piece life);
- Stage III: Deformations increase rapidly until failure [2].

Fatigue life of a material subjected to cyclic loading tests is linked to the evolution of the deformations during stage II [4–7]. By analogy with the method suggested for concrete [8], the evolution of vertical deformations over time was recorded for evaluating fatigue strength of material. The goal is to ascertain whether fatigue life of the mixed brick-mortar system also depends on the rate of increase of vertical deformations during stage II (termed secondary creep rate). **Figures 6–9** shows that the broken test pieces (before 1,00,000 cycles, as shown in **Table 7**) displayed a steeper slant in the stage II section of the curve, followed, at ca 80–90% of test piece life, by a sudden increase at stage III (failure). Conversely, the diagrams of the mixed specimens that passed 1,00,000 cycles mark displayed a lesser slant, reflecting an effective behavior still far from failure. From these results of cyclic tests, through linear interpolation between 20 and 80% of secondary creep values (**Figure 10**), derivatives $\partial\varepsilon_v/\partial n$ (i.e., the

Test piece	Days	σ (N/mm²)	Δ% σ (28 days)	E (N/mm²)	Δ% E (28 days)
DM 4.3	28	20.08		9886	
DM 6.2	28	20.97		10,957	
DM 7.3	28	20.87		11,231	
Average	**28**	**20.64**	—	**10,691**	—
DM 9.3	90	28.33		12,455	
DM 5.3	90	28.32		12,907	
DM 9.1	90	28.09		11,947	
Average	**90**	**28.25**	**+36.87**	**12,436**	**+16.32**
DM 1.1	150	28.99		12,849	
DM 10.2	150	28.46		13,152	
DM 6.2	150	28.10		10,448	
Average	**150**	**28.52**	**+38.18**	**12,150**	**+13.64**
DM 10.1	210	28.91		12,406	
DM 6.3	210	29.16		14,821	
DM 2.2	210	29.66		16,177	
Average	**210**	**29.24**	**+41.70**	**14,468**	**+35.32**

σ = failure stress, E = elastic modulus, Aσ = variation of σ, ΔE = variation of E.

Table 3. Mechanical characteristics during maturation of strengthening mortar D.

Test Piece	Cycles	σ_i (N/mm²)	σ_f (N/mm²)	Δσ% (0-cycles)	E_i (N/mm²)	E_f (N/mm²)	ΔE % (0-cycles)
DM 1.2	25	20.64	29.66	+43.70	13,557	11,119	−17.98
DM 8.2	25	20.64	25.59	+23.98	13,201	10,376	−21.40
DM 5.2	25	20.64	27.88	+35.08	11,066	11,257	+1.73
DM 3.2	25	20.64	—	—	11,841	13,386	+13.05
DM 4.2	25	20.64	—	—	8826	12,167	+37.85
DM 7.1	25	20.64	—	—	9003	7869	−12.59
Average	**25**	**20.64**	**27.71**	**+34.27**	**11,249**	**11,029**	**−1.95**
DM 3.2	50	20.64	24.08	+16.67	11,841	12,930	+9.20
DM 4.2	50	20.64	17.37	−15.84	8826	10,453	+18.43
DM 7.1	50	20.64	18.53	−10.22	9003	8418	−6.50
Average	**50**	**20.64**	**19.99**	**−3.12**	**11,249**	**10,600**	**−5.77**

σ_i = failure stress, σ_f = freezing-thawing cycles, Δσ% = variation of σ after freezing-thawing test, ΔE% = variation of E after freezing-thawing test.

Table 4. Static tests after freezing-thawing cycles on strengthening mortar D.

Series	Test piece	P_{max} (kN)	σ_{max} (N/mm²)	$\sigma_{average}$ (N/mm²)	E (N/mm²)
AL	AL02	102.75	19.30	15.40	11,988
	AL04	59.76	11.49		14,157
BL	BL01	108.51	22.17	16.89	16,940
	BL02	52.30	11.60		4400
CL	CL01	40.78	9.71	12.58	6597
	CL02	76.98	15.46		12,478
DL	DL01	58.50	12.10	12.04	6191
	DL02	60.45	11.98		8106

P_{max} = failure load, σ_{max} = failure stress, E = elastic modulus.

Table 5. Results of preliminary static tests on mixed test pieces.

Series	Test piece	Condition	P_{max} (kN)	σ_{max} (N/mm²)	$\sigma_{average}$ (N/mm²)	Δσ%	E (N/mm²)
AL	AL03	Cracked	95.54	19.78	15.88	+3.15	10,050
	AL06	Detached	81.00	15.83			8151
	AL08	Detached	59.30	12.03			6701
BL	BL07	Cracked	76.30	14.23	13.88	−17.81	6250
	BL10	Cracked	66.50	13.52			6582
CL	CL06	Whole	104.50	19.92	15.52	+18.25	10,604
	CL08	Whole	54.62	11.13			7191
DL	DL08	Whole	107.40	21.52	22.87	+89.93	35,358
	DL07	Whole	129.30	24.22			16,249

P_{max} = failure load, σ_{max} = failure stress, Δσ% = variation of σ after freezing-thawing tests, E = elastic modulus.

Table 6. Results of static tests after freezing-thawing cycles.

variations in the deformation versus time curve during stage II) were calculated. Through a linear regression on logarithmic scale, it is possible to plot the data in a diagram in order to obtain an analytical relationship (1) between secondary creep variations, $\partial\varepsilon_v/\partial n$, and the number of cycles (N) to fatigue failure:

$$N = 1839.92 \cdot \left(\frac{\partial \varepsilon_v}{\partial n}\right)^{-0.7284} \quad (1)$$

A valid correlation was established between secondary creep rate ($\partial\varepsilon_v/\partial n$) during stage II and fatigue life (number of cycles to failure, N). By performing a certain number of cycles on the material until deformations increase at a constant rate, it is possible to predict fatigue life with a good degree of approximation [9–11].

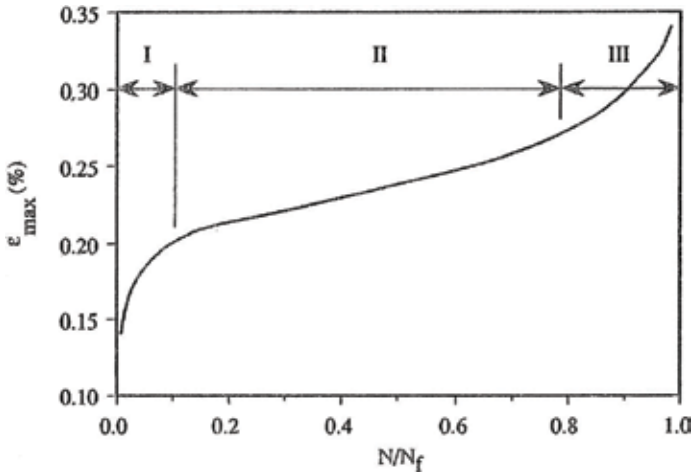

Figure 5. Monoaxial cycles compression test σ-ε curve.

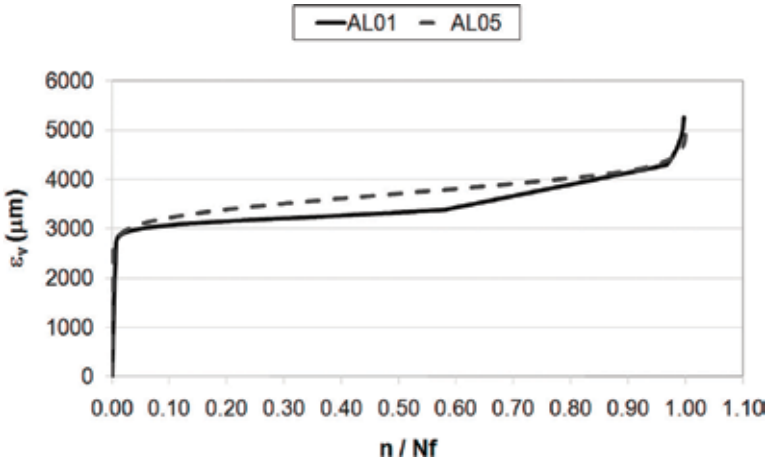

Figure 6. AL series cyclic tests: max vertical deformation.

In some samples, the theoretical value of cycles to failure N_{the} was found to be lower than that obtained from laboratory tests (**Table 7**). After the final value of cyclic test, the relationship (Eq. (1)) was useful to predict the failure on the detachment surface between brick and repair mortar. The measure of the volumetric deformations is in agreement with the theoretical value obtained from Eq. (1): the time when the volumetric deformations shifted to negative sign (propensity to bulge due to poor vertical collaboration or detachment at the interface between the two materials) was the failure time of the mixed brick-mortar specimen. The methodology and the numerical analysis proved very sensitive to the initial signs of weakening in the brick-mortar system, indicating clearly the onset of a crisis due to fatigue. **Figures 11–14** illustrate the static tests performed on mixed test pieces.

http://dx.doi.org/10.5772/intechopen.79543

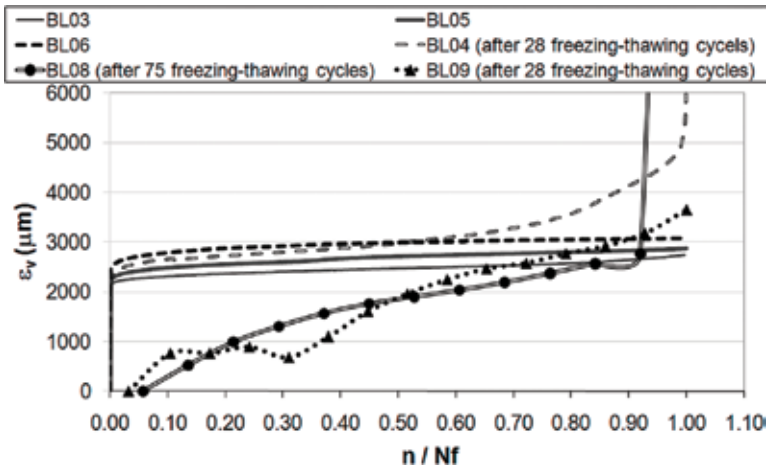

Figure 7. BL series cyclic tests: max vertical deformation.

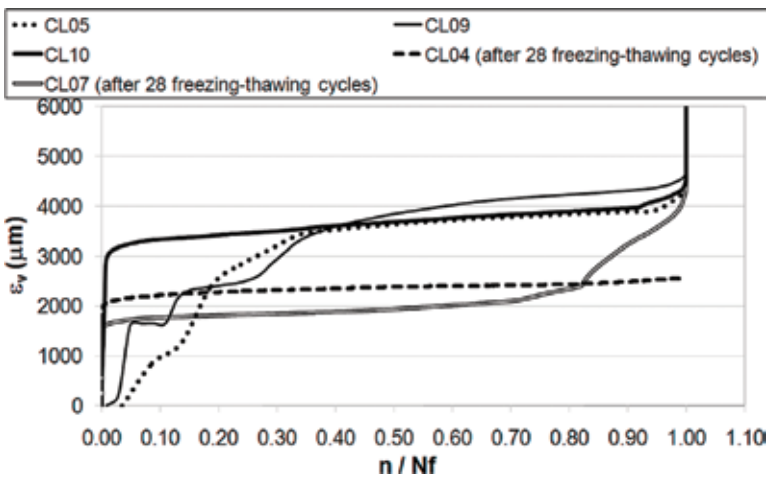

Figure 8. CL series cyclic tests: max vertical deformation.

The values obtained for a majority of the series remained within the average of the two preliminary tests, save for the series DL (**Figure 14**), which displayed a considerable increase in strength. In most cases, static curves after freezing-thawing revealed a more brittle behavior. Test pieces of BL and DL series that passed 1,00,000 cycles mark were tested to failure: the DL series displayed a noticeable increase of their mechanical properties. Some CL and DL test pieces were subjected both to freezing-thawing test and to cycling loading: CL maintained a static behavior similar to the weakest preliminary test result; instead in the DL series, an appreciable increase of strength was mated to a lesser degree of brittleness compared to the test pieces subjected to cyclic loading only.

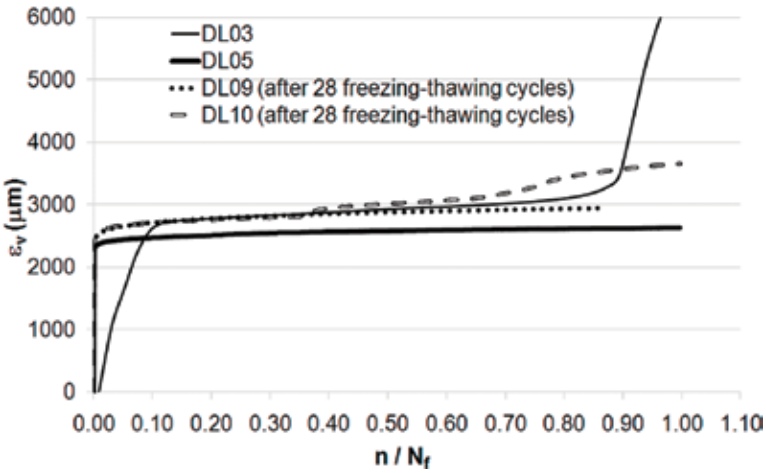

Figure 9. DL series cyclic tests: max vertical deformation.

Test piece	n	$\partial\varepsilon_v/\partial n$	LogN	$\text{Log}(\partial\varepsilon_v/\partial n)$	N_{the}
AL01	22,380	0.0270	4.350	−1.569	25,583
AL05	53,465	0.0198	4.728	−1.703	32,029
BL03	1,00,000	0.0047	5.000	−2.323	90,605
BL05	1,00,000	0.0040	5.000	−2.398	102,716
BL06	1,00,000	0.0024	5.000	−2.612	147,056
CL05	461	5.1818	2.664	0.714	555
CL09	1223	2.5110	3.087	0.400	941
CL10	15,835	0.0501	4.200	−1.300	16,294
DL03	1149	0.4704	3.060	−0.328	3187
DL05	1,00,000	0.0015	5.000	−2.813	206,028
DL06	1,00,000	0.0070	5.000	−2.155	68,328
BL04	40,993	0.0340	4.613	−1.469	21,612
BL09	360	9.4729	2.556	0.976	358
CL04	1,00,000	0.0035	5.000	−2.454	112,832
CL07	46,622	0.0192	4.669	−1.717	32,795
DL09	1,00,000	0.0025	5.000	−2.594	142,671
DL10	1,00,000	0.0113	5.000	−1.947	48,171

Table 7. Analysis of the data.

http://dx.doi.org/10.5772/intechopen.79543

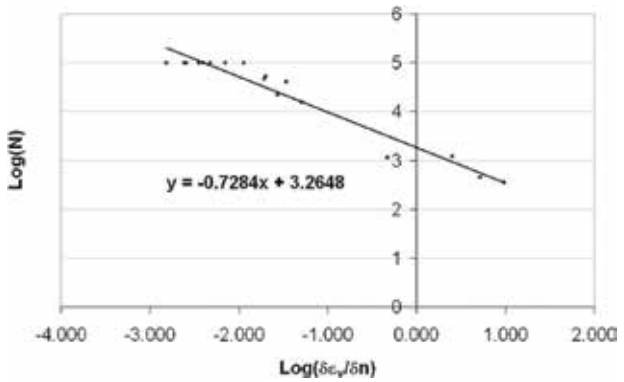

Figure 10. Fatigue life of mixed test pieces $\partial\varepsilon_v/\partial n$ chart.

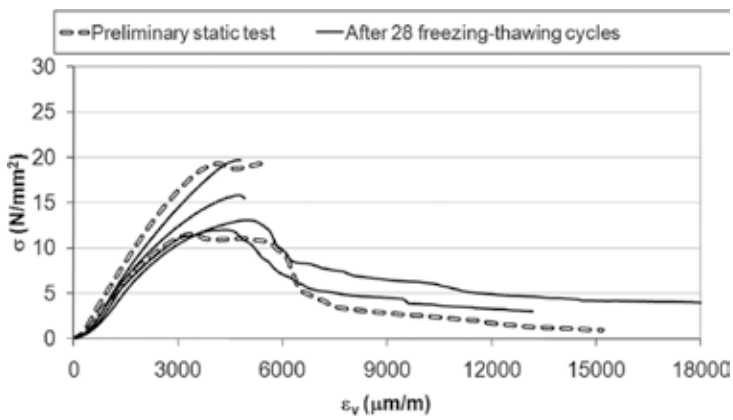

Figure 11. AL series static tests.

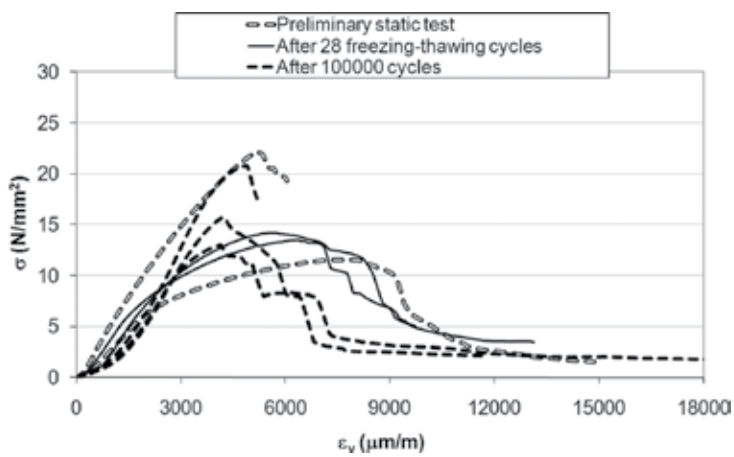

Figure 12. BL series static tests.

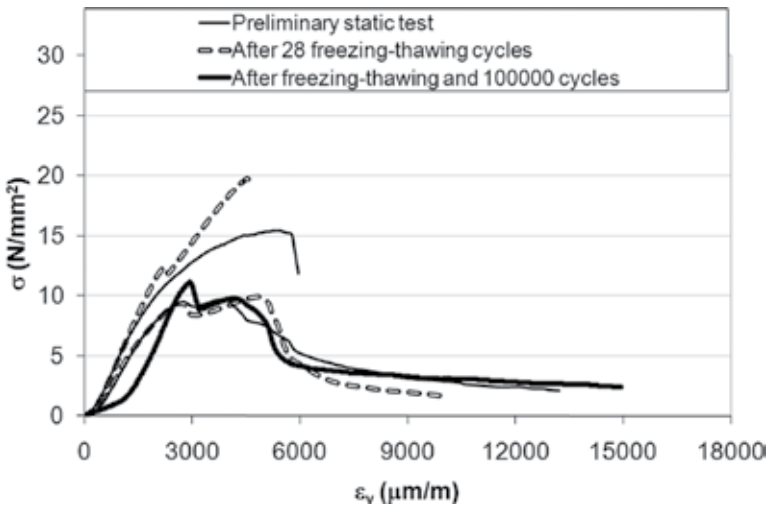

Figure 13. CL series static tests.

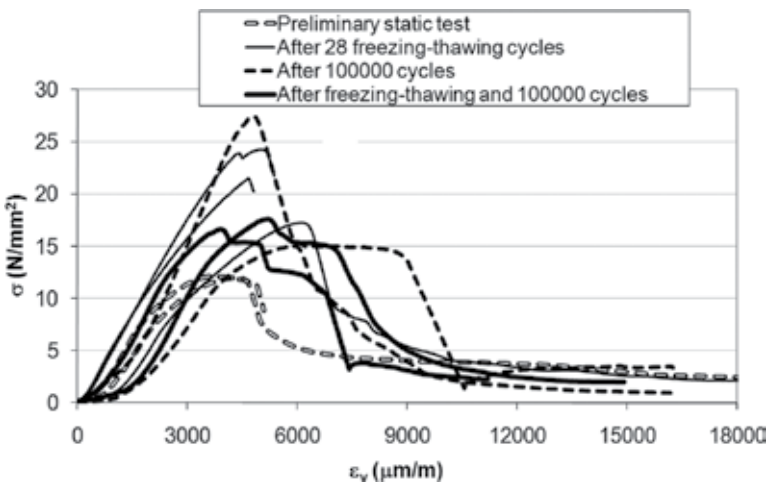

Figure 14. DL series static tests.

2.4. Selection of optimal mortar

From the results of this experimental procedure, mortar D was chosen for the best compatible characteristics because, compared with the other mortars, during fatigue and freezing-thawing tests, these strengthening materials showed the greatest number of cycles without excessive variations of mechanical characteristics.

The choice of mortar D also was confirmed by the good results of preliminary tests, performed in situ. From six double flat jack tests, a value of failure tension σ average was found equal to 1.91 N/mm^2 in accord with that (1.61 N/mm^2) obtained by laboratory tests on the big masonry walls, manufactured by original bricks and stones extracted in situ. The positive confirmation

http://dx.doi.org/10.5772/intechopen.79543

Figure 15. Application of mortar D as the reinforced plaster to Venaria's masonries.

came from the real application of mortar D as reinforced plaster retrofitting of some walls of the Royal Palace of Venaria (**Figure 15**). After 10 years, this plaster does not present any pathology of incompatibility.

3. Experimental procedure for selecting a durable dehumidified mortar

Often masonry walls of historical buildings are subject to rising damp effects due to capillary or rain infiltrations. In the time, their cyclic action produces decay and delamination of historical plasters. The restoration market offers a great number of dehumidified repair mortars to use as new transpiring plasters. Nevertheless, their mechanical and thermo-hygrometric characteristics have not been compared carefully with those of the historical masonry supports, often producing the failure of restoration work. Preventing this phenomenon is the main way of increasing the durability of repair work [12].

An innovative laboratory procedure, developed at the Non-Destructive Testing Laboratory of the Politecnico di Torino, is described for test mechanical adhesion of new repair mortars. Compression static tests were carried out on composite specimen stone block-repair mortar, which specific geometry can test the de-bonding process of mortar in adherence with a stone masonry structure. The methodology is being used at Sacro Monte di Varallo Special Natural Reserve. Situated at the top of the hill above the town of Varallo in Piedmont (Italy), Sacro Monte is an artistic-religious complex consisting of 45 chapels, which contain with frescoes and sculptures that tell the story of the life of Christ (**Figure 16**).

The main problem of historical plasters' preservation is linked to the rain infiltrations and to the freezing-thawing cycles that compromise their adhesion to stone masonries. Through compression static tests on stone-mortar composite specimens, it was possible to prequalify the dehumidified mortar with greater durability guarantees. Sometimes the long-term detachment determined the failure of the restoration work. The test validates the mechanical

Figure 16. Decay of historical plasters because of the rain infiltrations (Sacro Monte of Varallo).

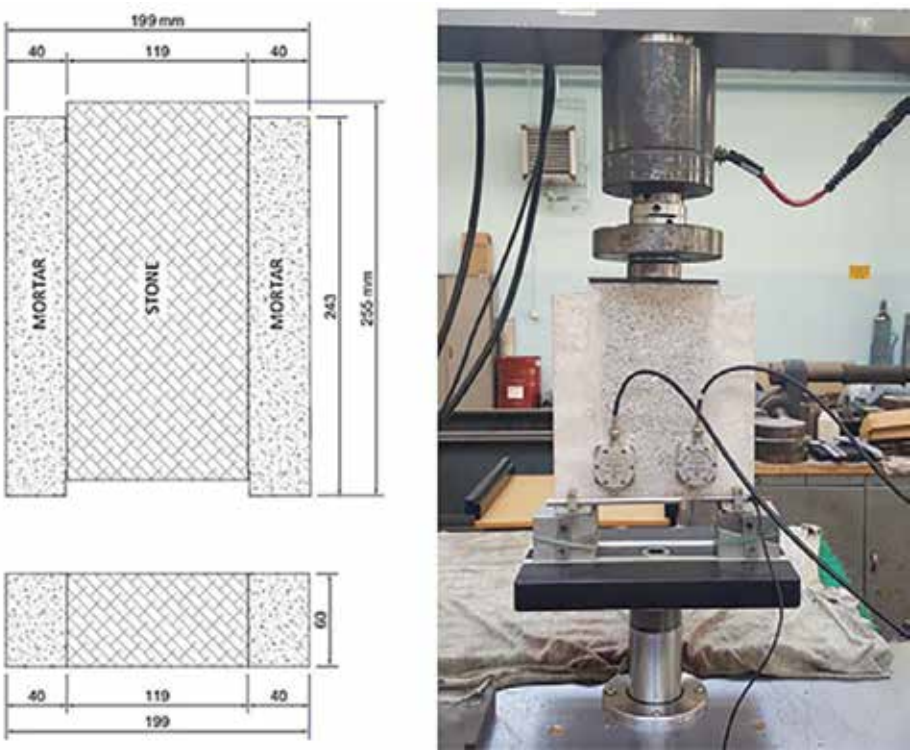

Figure 17. Geometry of composite specimen and test setup.

http://dx.doi.org/10.5772/intechopen.79543

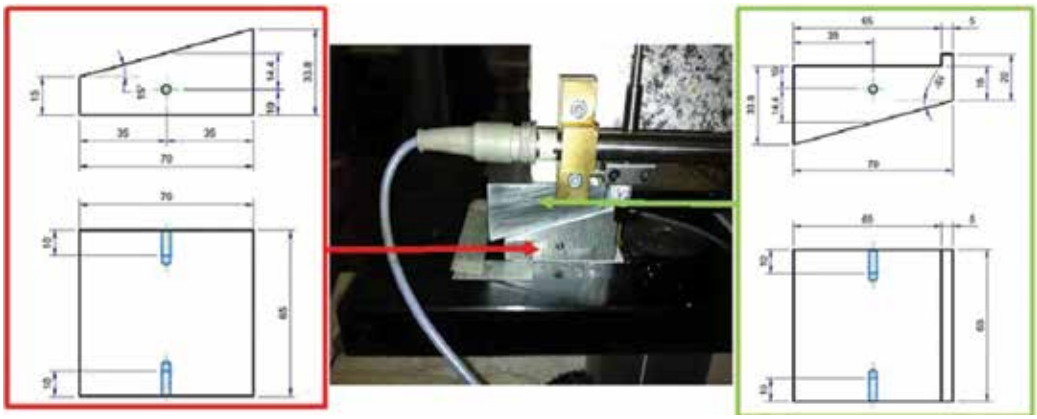

Figure 18. The wedges' geometry and test setup.

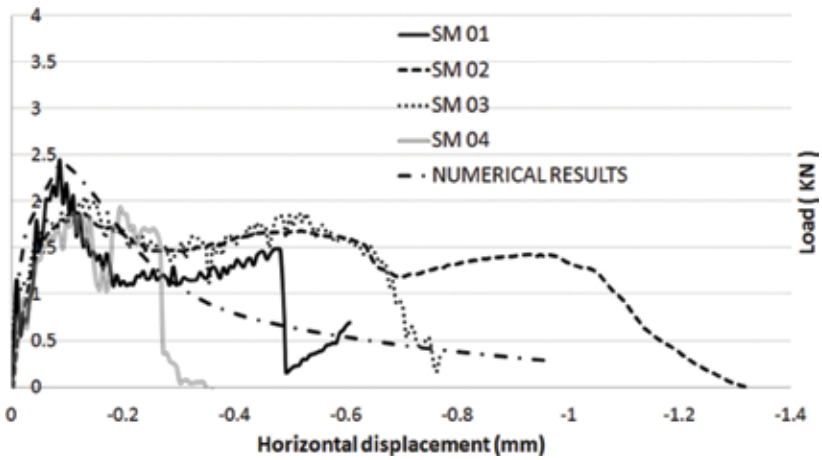

Figure 19. Load-horizontal displacement curves of static tests.

compatibility between the repair mortars and historical masonries stone, as a guarantee also for durability over time against atmospheric agents.

3.1. Preparation of the laboratory test

For carrying out tests, a particular geometry of the composite specimen has been proposed. Four mixed specimens were made, applying a 40 mm mortar layer to both shorter faces of the stone brick suitably cut with the dimensions shown in **Figure 17**. The mechanical characteristics of the repair mortar and the stone brick were chosen equivalent to those of the stone masonry at the Sacro Monte di Varallo. The experimental test can carry out also by masonry brick, if the historical walls were made by bricks. The hydraulic lime mortar was a pre-blended transpiring product, for dehumidifying repair work on historical masonry

damaged by dampness. For this mortar, the Young's modulus was 4379 MPa, and the compressive strength was 33.8 MPa.

The surface of the stone block has been treated specifically by means of a drill to facilitate the mortar's adhesion. This treatment aimed to simulate the real discontinuities on the wall surface that favor the adhesion of the plaster. The application of the dehumidified mortar took place leaving specific and surface symmetrical discontinuities at the top and bottom of the specimen, as shown in **Figure 17**. These notches favored the trigger and propagation of multiple cracks, in order to test the adhesion of two linked materials. An inductive horizontal displacement transducer was applied at the bottom of the specimen for the bulging displacements. The vertical displacements were recorded by the piston's translation of the 250 kN servo controlled test machine. The composite specimens were tested by monotonous compression load by horizontal controlled opening (0.0001 mm/s). Static tests have been performed after 28 days of maturation. The composite specimen rested, through the side layers mortar, on a double system of steel wedges (**Figure 18**). The wedges were coupled by a 1 mm thick Teflon layer for reducing the horizontal friction during the plaster's expansion. The "SM" (Stone brick-Mortar) label has been associated with each specimen with its sequence number.

3.2. Composite stone-repair mortar specimens

The results of compressive static tests are shown in **Figure 19**. A numerical simulation based on the cohesive crack model was us```ed to follow the experimental data, in order to describe the evolutionary phenomenon of de-bonding as a function of a small number of parameters [13–15]. The composite specimen stone-mortar displayed four stress singularity points: two notch tips at the specimen's top, and two at the specimen's bottom. These points were the weakest planes involved in the singular stress fields. Because of the wedges, the cracks that start from the bottom of the specimen showed greater velocity than the cracks that start from the top of the specimen. To exception of SM 04, the other composite specimens were displayed a ductile behavior keeping a residual load and displacement after the peak load. That is a fundamental requirement for a durable service life of repair plasters subjected to thermo-hygrometric cycles stress as rising damp effects. The specific geometry of the composite specimens has allowed to test the adherence between dehumidified repair plaster and masonry structures, in order to prequalify the durability of the repair product. The notch tips have put to the test the adherence of the repair plaster applied to the stone support, simulating the fatigue loads that can compromise the restoration work.

The Teflon sheet, inserted at the contact surface between the upper and lower wedge, was able to reduce the friction and to stabilize the load curves. The static compressive tests represent a rather fast laboratory procedure useful for analyze the delamination of the dehumidified repair plasters applied to the historical masonry of the Sacro Monti di Varallo. The next step of this experimental research, at the moment in progress, is to carry out the cyclic compressive tests in order to simulate the fatigue stress between the masonry stone and the repair mortar.

The experimental tests can be carried out by several and different dehumidified mortars in order to compare their mechanical behavior.

4. Conclusions

Experimental procedures have been described to validate the choice of a durable repair mortar against different stress stresses (including thermal stresses) and compatible with the mechanical characteristics of the historical masonry. The experimental methodology is useful to identify a number of key parameters for interpreting the long-term behavior of historic brick-strengthening mortar system. The results showed a considerable change of mechanical characteristics in strengthening materials due to maturation, thermo-hygrometric and various fatigue loading condition that can affect masonry structure after restoration process, according to the experimental results of previous researches [3, 5]. In this way it is possible avoid errors associated with materials that are not mechanically compatible. The experimental procedure described above studied in depth previous researches on the creep of single materials [6–8] and historical walls [4, 5, 9, 10], shifting the focus on the analysis of the long-term behavior of the new strengthening materials applied to historical masonry structures. The tests have allowed to select the most compatible and durable restoration product and technique for strengthening work in the Royal Palace of Venaria Reale.

In parallel an innovative laboratory procedure for pre-qualification of dehumidified repair mortars applied to historical masonry buildings has been described. The specific geometry of mixed stone-mortar specimens can test the de-bonding process of mortar in adherence with the historical masonry structures. This method supplies useful indication to select, from a range of alternatives, the repair product that is best in keeping with the mechanical characteristics of historical material. The experimental procedure is currently being used at Sacro Monte di Varallo Special Natural Reserve, where the historical stone masonry of the Chapels are subjected to rising damp effects due to capillary action or rain infiltrations. The study of the phenomena involved in the de-bonding process between the masonries stone and the dehumidified repair plasters is basic to plan a durable restoration work of the historical plasters of the Chapels.

Author details

Alessandro Grazzini

Address all correspondence to: alessandro.grazzini@polito.it

Politecnico di Torino, Turin, Italy

References

[1] Valluzzi MR, Binda L, Modena C. Experimental and analytical studies for the choice of repair techniques applied to historic buildings. Materials and Structures. 2002;**35**: 285-292. DOI: 10.1007/BF02482134

[2] Bocca P, Grazzini A. Mechanical properties and freeze-thaw durability of strengthening mortars. Journal of Materials in Civil Engineering. 2013;**25**:274-280. DOI: 10.1061/(ASCE)MT.1943-5533.0000597

[3] Mutluturk M, Altindag R, Turk G. A decay function model for the integrity loss of rock when subjected to recurrent cycles of freezing-thawing and heating-cooling. International Journal of Rock Mechanics and Mining Sciences. 2004;**41**:237-244. DOI: 10.1016/S1365-1609(03)00095-9

[4] Anzani A, Garavaglia E, Binda L. Time dependent behaviour of historic masonry: A probabilistic model. In: Proceedings of the 7th International Masonry Conference; October 30–November 1, 2006; London. British Masonry Society [CD-ROM]

[5] Anzani A, Binda L, Mirabella Roberti G. The effect of heavy persistent actions into the behaviour of ancient masonry. Materials and Structures. 2000;**33**:251-261

[6] Minh-Tan D, Chaallal O, Aitcin PC. Fatigue behaviour of high-performance concrete. Journal of Materials in Civil Engineering. 1993;**5**:96-111

[7] Mu B, Shah SP. Fatigue behavior of concrete subjected to biaxial loading in the compression region. Materials and Structures. 2005;**38**:289-298. DOI: 10.1617/14155

[8] Taliercio A, Gobbi E. Experimental investigation on the triaxial fatigue behaviour of plain concrete. Magazine of Concrete Research. 1996;**48**:157-172. DOI: 10.1680/macr.1996.48.176.157

[9] Carpinteri A, Grazzini A, Lacidogna G, Manuello Bertetto A. Durability evaluation of reinforced masonry by fatigue tests and acoustic emission technique. Structural Control and Health Monitoring. 2014;**21**:950-961. DOI: 10.1002/stc.1623

[10] Bocca P, Lacidogna G, Grazzini A, Manuello Bertetto A, Masera D, Carpinteri A. Creep behaviour in reinforced masonry walls interpreted by acoustic emission. Key Engineering Materials. 2010;**417-418**:237-240. DOI: 10.4028/www.scientific.net/KEM.417-418.237

[11] Brooks JJ, Abu Bakar BH. Shrinkage and creep of masonry mortar. Materials and Structures. 2004;**37**:177-183. DOI: 10.1007/BF02481617

[12] Fassina V, Favaro M, Naccari A, Pigo M. Evaluation of compatibility and durability of a hydraulic lime-based plaster applied on brick wall masonry of historical buildings affected by rising damp phenomena. Journal of Cultural Heritage. 2002;**3**:45-56. DOI: 10.1016/S1296-2074(02)01158-5

[13] Barpi F, Valente S. Lifetime evaluation of concrete structures under sustained post-peak loading. Engineering Fracture Mechanics. 2005;**72**:2427-2443. DOI: 10.1016/j.engfracmech.2005.03.010

[14] Barpi F, Valente S. The cohesive frictional crack model applied to the analysis of the dam-foundation joint. Engineering Fracture Mechanics. 2010;**77**:2182-2191. DOI: 10.1016/j.engfracmech.2010.02.030

[15] Bocca P, Grazzini A, Masera D, Alberto A, Valente S. Mechanical interaction between historical brick and repair mortar: Experimental and numerical tests. Journal of Physics: Conference Series. 2011;**305**:1-10. DOI: 10.1088/1742-6596/305/1/012126

Chapter 2

Acoustic Emission Monitoring of Fracture Tests

Turbadrakh Chuluunbat and Andrii Kostryzhev

Additional information is available at the end of the chapter

http://dx.doi.org/10.5772/intechopen.79325

Abstract

Identification of defect(s) where crack initiation is possible and prediction of crack propagation are of great importance in materials engineering. The current chapter analyzes the application of the acoustic emission (AE) technique for fracture monitoring in the line pipe steel during single-edge-notched tension (SENT) test and Charpy V-notch (CVN) impact test. It was found that the AE activity starts before the yield point, due to the stress concentration at the crack tip, and increases suddenly before the peak load is reached, due to the fracture initiation. Toward the end of the test, the AE hit density increases again, following intensive crack propagation. The AE analysis conducted in the present chapter showed a strong evidence of AE hit density increasing before the peak load is reached, the moment corresponding to fracture initiation.

Keywords: acoustic emission, fracture, signal analysis, tests

1. Introduction

1.1. Acoustic emission

Acoustic emission is a phenomenon whereby transient stress waves or displacement waves are generated following the rapid release of energy from localized sources such as crack initiation sites, fracture propagation, and dislocation motion in metals [1–3]. Elastic energy is transmitted through the material in the form of transient elastic waves and can be detected by sensors on the surface of a specimen (**Figure 1**).

The sensor used in AE measurements converts elastic waves into electrical signals which are then processed and analyzed by special hardware and software. Useful AE signals need to be distinguished from the background noise generated from the surroundings [4, 5]. **Figure 2** shows typical acoustic emission signal types. There are two main types of useful AE signal:

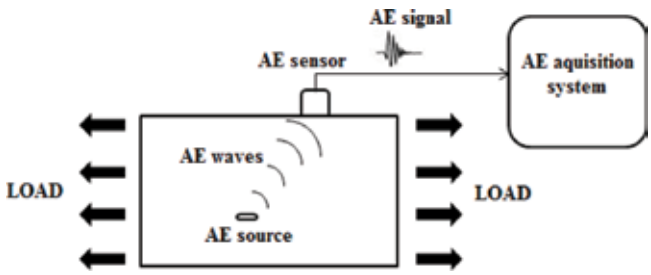

Figure 1. Schematic presentation of AE monitoring technique.

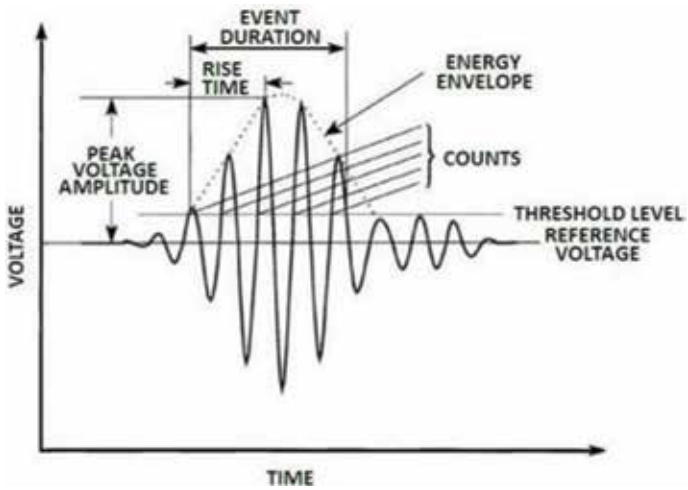

Figure 2. Parameters of an AE hit [6].

"burst" and "continuous" [7]. Burst AE signals correspond to individual events such as stages of crack growth, brittle fracture, and impact. Continuous AE signals correspond to sustained signals generated by time-overlapping events such as plastic deformation, friction, and liquid leaks [3, 8]. It has been demonstrated that continuous low-amplitude AE signals are generated from low-energy sources. Discrete high-amplitude AE signals are generated from high-energy sources [9].

Currently, the AE technique is used in many industries for nondestructive testing of various materials and structures. A major advantage of AE measurement is that it can monitor in real time the development of defects occurring inside a material without further damaging of the material [10, 11]. However, for some applications, the operating environments are often very noisy, while the AE signals are usually very weak. This makes the detection of AE signal a challenging task.

1.2. AE source and AE signal analysis

There are two approaches to analyze AE signals: "Parameter-based" and "Waveform-based" [2]. Several AE parameters, such as oscillation count, amplitude, energy, event duration, and

rise time, can be derived from the AE signal. The major parameters used in the parameter-based analysis of the AE signal are shown in **Figure 2**.

The AE waveform and frequency analysis are usually carried out using fast Fourier transform and wavelet transform [4, 12, 13]. Identification of the AE signal can be based on the type of AE waveform and its frequency range: burst-type signal for individual events and continuous signal for prolonged events [3]. For example, the AE analysis during the fatigue cracking [13] showed three types of waveforms (**Figure 3**): from fatigue cracking (a) and (b); fretting (c) and (d); and noise (e) and (f). The microcrack (a) and (b) had strong high-frequency components above 0.5 MHz in comparison with fretting and noise, although peak amplitude was generally low.

Generally, an AE signal in metals is generated upon the initiation and growth of cracks, due to slip and dislocation movements, twinning, or phase transformation. In these cases, stress plays an important role in giving rise to AE. Plastic deformation is induced by permanent changes in the positions of atoms. These changes are related to and based on the movement of the dislocations [14]. In addition, fracture occurs when the material breaks and new surfaces are produced.

Figure 4 presents the AE sources in steel. The major macroscopic AE sources in steel are crack jumps, development of plastic deformation, fracturing and debonding of hard inclusions. The main microscopic AE sources include dislocation movement, interaction, annihilation, slip

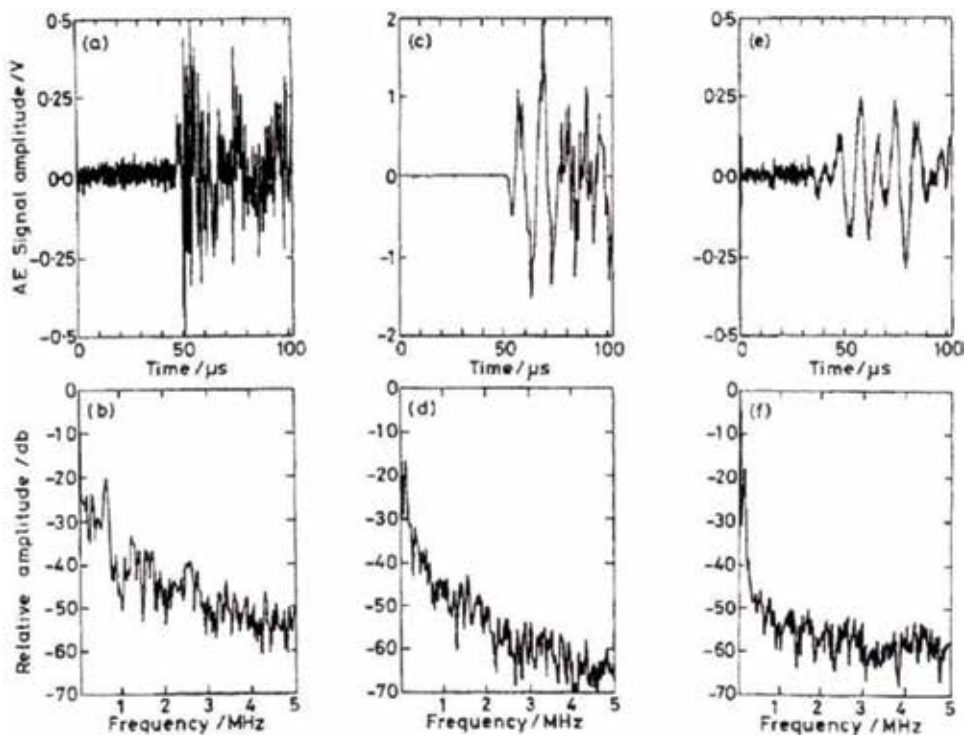

Figure 3. Waveforms and corresponding frequency spectra [13].

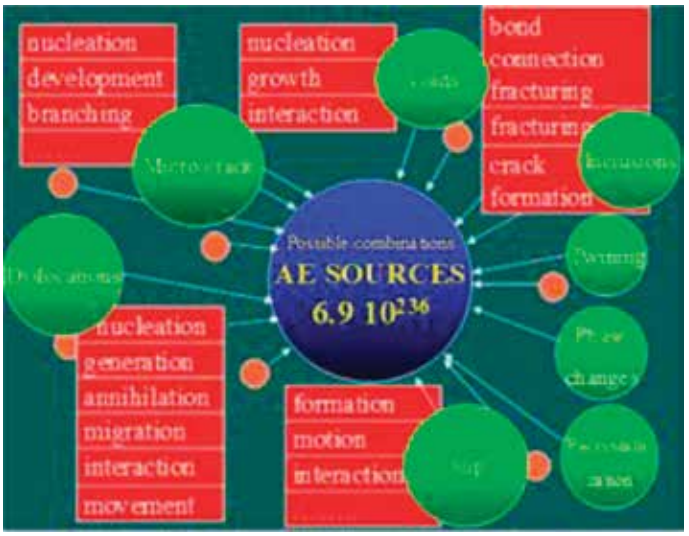

Figure 4. AE sources in steel micro and macrostructure [10].

formation, void nucleation, void growth, and void interaction [15–17]. The most detectable AE signals are generated when a loaded material undergoes plastic deformation or when a material is loaded at or near its yield stress [18]. AE activity can also be observed when the material ahead of the crack tip undergoes plastic deformation (microyielding). In primary emissions arising from crack growth, there are two sources of cracks that affect the AE [19]. In the first case, there may be emissive particles (e.g., nonmetallic inclusions) in the stress concentration region near the crack tip. Since these particles are less ductile than the surrounding material, they tend to break more easily when strained. The second AE source is the propagation of crack tip occurring as a result of dislocation motion and small-scale cleavage produced by tri-axial stresses.

1.3. AE monitoring of fracture

A number of AE studies performed during tensile testing detected a burst AE signal near yielding [13], AE activity originating from movement of dislocations [20], and AE wave parameters arising from macroyielding [21]. Researchers have also studied the relationship between AE features (signal amplitude, frequency, energy, duration, and count) and test parameters (load, stress, and crack growth) during tensile testing of notched and plain metal specimens [22–27].

As can be seen from **Figure 5**, the tensile process could be divided into four stages: (1) microplastic deformation, (2) yielding, (3) strain hardening, and (4) necking and fracture. Significant AE energy release is expended in the first and second stages. AE energy decreased in stage 3, and the density of AE hits increased at stage 4 due to the occurrence of specimen fracture [20, 29].

Fracture tests were carried out to detect AE signals associated with crack initiations [27, 28, 30] and crack growth in metals [29, 31–33].

http://dx.doi.org/10.5772/intechopen.79325

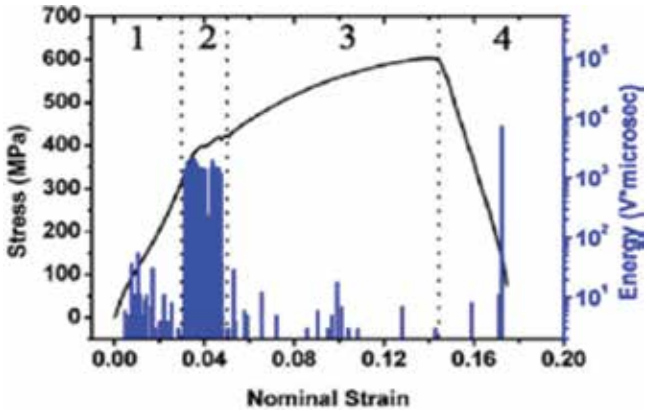

Figure 5. Stress-strain curve coupled with AE energy for tensile testing of Q345 steel [28].

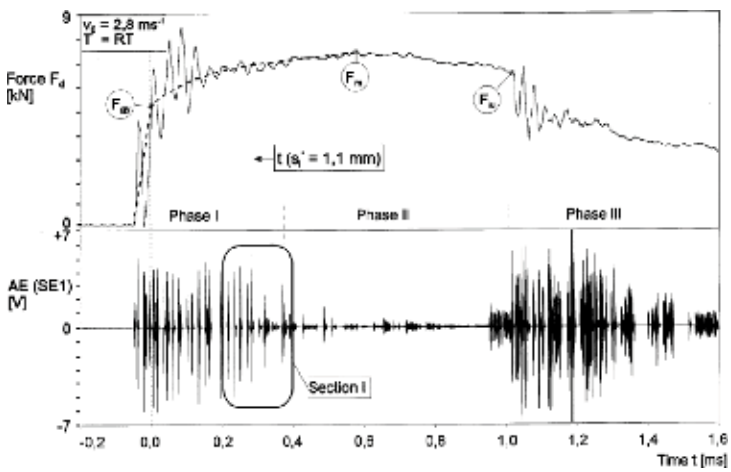

Figure 6. Load and AE signal from instrumented three point impact loading [34].

In other studies by Richter et al. [34] and [35], modified CVN specimens of 10CrMo9 steel with 20% side grooves were used to detect the onset of tearing. They did a dynamic three-point bending test using AE sensor located inside the hammer of tester (**Figure 6**).

This study investigated dynamic fracture behavior and determination of fracture initiation using the AE method. The main purpose of the investigation was to use the dynamic J integral (Jid) at crack initiation and dynamic yield stress (Gyd) for the characterization of elastic-plastic material behavior under rapid loading (impact).

Tronskar et al. [35] applied a different approach to determine the onset ductile tearing in instrumented Charpy testing of NVE 36 steel. A linear correlation was found between the time of ductile fracture initiation determined by the AE monitoring and direct displacement interferometric strip method.

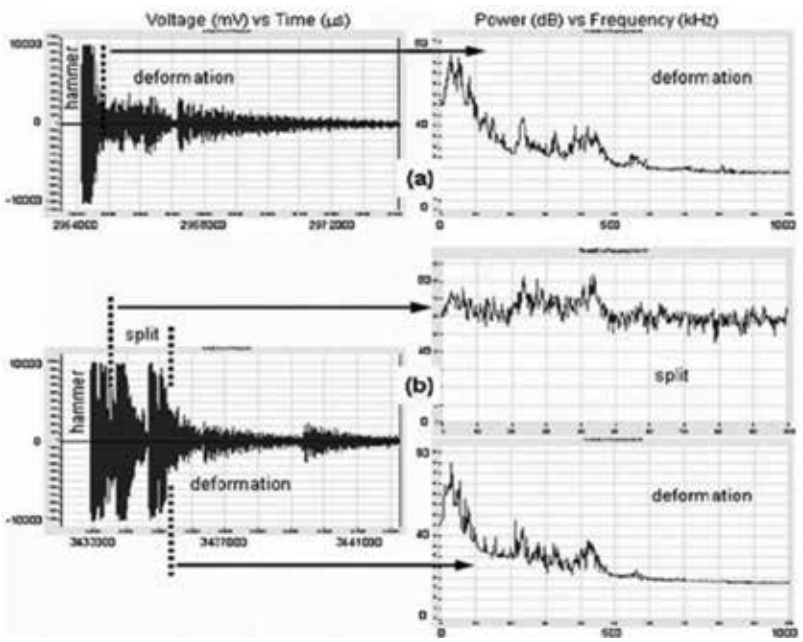

Figure 7. Acoustic emission during CVN at 60 and 80 J impact energies [12].

The possibility of detection of split formation during low-blow Charpy impact (40–100 J) testing was also shown for high-strength steel by Kostryzhev et al. [12]. AE waveform analysis was carried out to separate signals generated from the hammer, plastic deformation, and split initiation. **Figure 7** shows acoustic waves and power spectra for testing of strip steel at 60 and 80 J impact energies. The AE waves generated from crack initiation and growth were in two peak frequencies between 200 and 500 kHz and 500 and 1000 kHz. It is indicated by a shorter duration of the fracture process than that of deformation by dislocation slip.

2. Materials, equipment, and method

2.1. Materials and equipment

Two grades of pipeline steels, API-X70 and API-X80, were used in this study. Their chemical compositions are shown in **Tables 1** and **2**. All X70 specimens used in SENT and CVN tests were cut from a pipe with 14.1 mm wall thickness and 1067 mm diameter. All X80 specimens were prepared from a pipe with 25 mm wall thickness and 1067 mm diameter.

The SENT tests were carried out using an Instron 8801 servo hydraulic dynamic testing machine. The machine has console software which provides full system control from a computer including waveform generation, calibration, limit setup, and status monitoring. The testing system includes up to a 100 kN axial force capacity, a Dynacell load cell, standard height frame options, and a wide range of grips, fixtures, and accessories [36].

C	Mn	Si	Nb	Ti	V	Ni	Cr
0.0499	1.56	0.238	0.0576	0.0088	0.0256	0.214	0.028
Cu	Mo	Al	Ca	N	S	P	B
0.163	0.148	0.035	0.0015	0.0036	0.0014	0.0059	0.0001

Table 1. Composition of X70 pipeline steel (wt%).

C	Si	Mn	P	S	Cu	Alt	Nb	Ni	Cr	Ti	Ceq	Pcm
0.064	0.22	1.72	0.006	0.002	0.23	0.027	0.068	0.206	0.22	0.0158	0.42	0.18

Table 2. Composition of X80 pipeline steel (wt%).

The CVN impact tests were carried out using a 450MPX instrumented Instron Impact tester. The capacity of this machine is 750 J. The specimen temperature was controlled by a cooler containing methanol (for above −80°C) and a mixture of liquid nitrogen and methanol (for below −80°C). **Figure 8** shows the AE signal processor, manufactured by the Physical Acoustics Corporation (USA). The system consisted of a wideband sensor with an operating frequency range of 50–1000 kHz and temperature range of −65°C … + 175°C, a single-channel AE digital signal processor with an internal low noise preamplifier and a computer. The AE signal was recorded and analyzed using the AEwin software. This software has the ability to analyze waveforms and conduct fast Fourier transform (FFT). All data are saved in standard Physical Acoustics Corporation (PAC) defined DTA files.

2.2. SENT test

The geometry of a SENT specimen is conforming to DNV RP F108 specifications [37]: 12 mm in width, 6 mm in thickness, and 60 mm in gauge length. A notch representing an initial "crack" of 2 mm length and 0.3 mm width was cut using wire cutting. The crack (notch) depth

Figure 8. A single-channel AE digital signal processor.

was a third of the specimen thickness. The tests adopted a slower strain rate of 2.7×10^{-4} and a higher strain rate of 5.5×10^{-3}. **Table 3** shows testing conditions.

Additional test was conducted at a lower temperature of −20°C, while other tests were performed at room temperature (~20°C). The materials used in SENT tests were X70 and X80 line pipe steels. X70 specimens were cut using wire cutting from a 14 mm wall thickness and 1067 mm diameter pipe. X80 specimens were cut from a 25 mm wall thickness and 1067 mm diameter pipe.

A scheme of the SENT test setup is illustrated in **Figure 9**. During testing, the AE sensor was attached to the specimen using a sticky band with ultrasound treatment gel applied between the specimen and sensor surfaces as a coupling material to increase the signal quality. All the recorded waveforms were analyzed in time and frequency domain (frequency spectrum) using FFT. The crack propagation during SENT testing was observed using a MotionPro X3 high-speed camera with excellent resolution, up to 8500 μs exposure time and up to 300 of frame/sec recording rate. After testing, the fracture surface was observed by JEOL JSM-6490LA scanning electron microscope (SEM) operating at 20kV.

2.3. CVN test

The CVN test involves striking the specimen with a striker (hammer), mounted at the end of a pendulum. The CVN test procedures and specimen dimensions can be taken from the

Test number	Material grade	Temperature	Strain rate
1	X70	RT (20°C)	2.7×10^{-4}
2	X70	RT (20°C)	5.5×10^{-3}
3	X80	RT (20°C)	2.7×10^{-4}

Table 3. SENT test conditions.

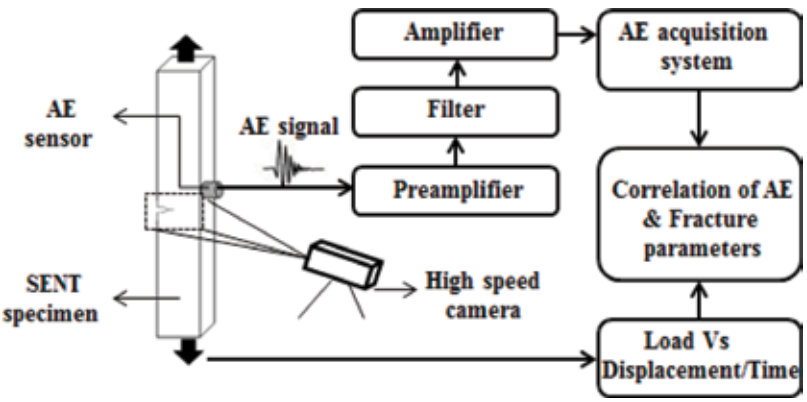

Figure 9. A schematic of AE measurement setup of SENT testing.

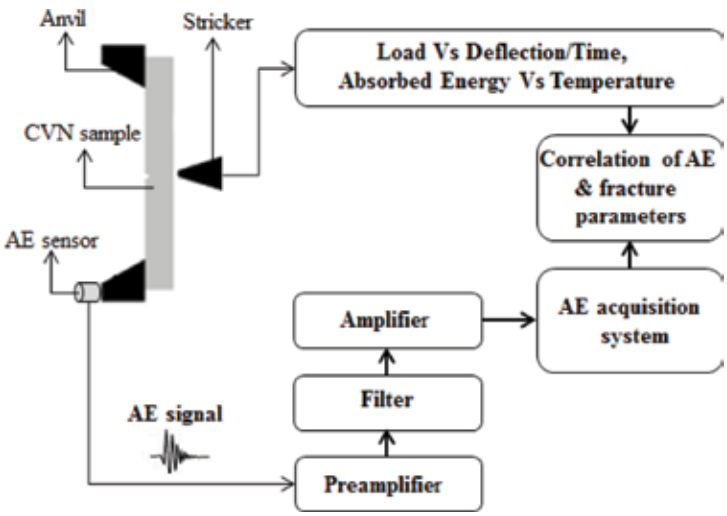

Figure 10. A scheme of experimental setup for AE monitoring of Charpy testing.

Australian standard-1544.2 [38]. A scheme of the CVN test setup is illustrated in **Figure 10**. The specimen that fits in the Charpy impact tester is rectangular with a notch cut on one side. The notch represents a predetermined crack initiation location. Charpy specimens, in particular the notches, are carefully designed and prepared, since variations in notch dimensions will seriously affect the results of the tests. In this work, CVN tests using full size specimens with 10 mm thickness were performed at various temperatures: RT (20°C), −20, −40, −60, −80, −100, and − 120°C, using an instrumented Charpy impact machine. In addition, sub-size specimens with B = 5 mm and 7.5 mm were used for testing at ambient temperature. Each test has been repeated three times. During the test, the absorbed impact energy and the load-deflection curve were recorded. Before testing, specimens were kept in the cooler for at least 40 minutes to achieve a uniform temperature. The AE sensor was nonpermanently attached to one of the anvils of Charpy machine with a sticky band, and ultrasound treatment gel was applied as a coupling material to increase the signal quality. The choice for the sensor location was determined by minimizing the saturation condition.

3. Results and discussion

3.1. AE monitoring of SENT

Pipelines can be subjected to severe deformations. Local defects may result from bending, generated by ground/soil movement or washout during installation and operation, and biaxial loading, originating from longitudinal straining and internal pressure [39, 40].

To fully explain pipeline failure, research is needed to develop a better understanding of the mechanical properties and fracture behavior (initiation and propagation) in both traditional

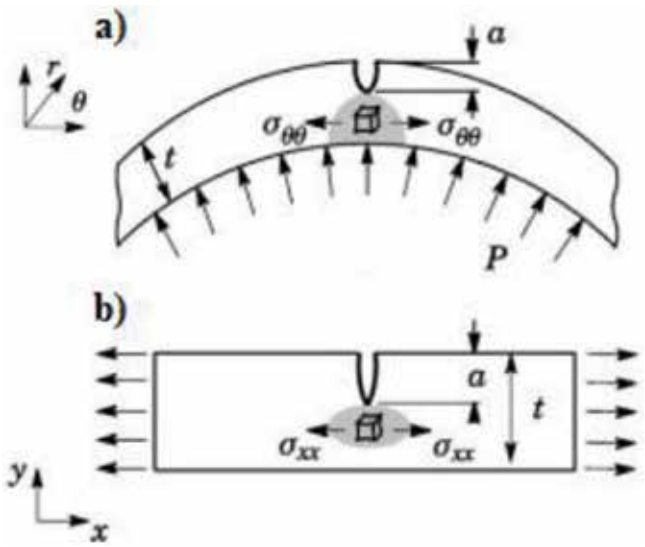

Figure 11. (a) Schematic loading condition for a pressured pipe; (b) SENT test specimen [38].

and newly developed pipeline steels. One of the representative specimens used to evaluate the fracture characteristics of the pipeline steel was designed to be compatible with a SENT test. The fracture toughness data obtained from a SENT test can be more suitable for fracture predictions of pressurized pipelines and cylindrical vessels than data obtained from notched fracture specimens under bending or impact loading [40] (**Figure 11**).

Based on the AE activity, the load-displacement curve for slow strain rate can be divided into three regions (**Figure 12**):

- Region I. There were few hits in this region with a maximum amplitude of 45 dB and average frequency varying from 80 to 100 kHz;
- Region II. The AE activity increased compared to Region I. There are seven hits in this region. The maximum amplitude is 70 dB and the average frequency ranges from 100 to 350 kHz;
- Region III. The AE activity is stable in accordance with the monotonous crack propagation. At the end of this region, the AE hit density increased significantly following the occurrence of multiple fracture events prior to separation of the specimen in two parts. The main AE signals observed in this region were of 75 dB amplitude and 200–400 kHz average frequency.

The load-displacement curve coupled with AE activity for SENT of X80 steel (**Figure 13**) has shown a higher hit density compared to X70 steel tested at the same conditions (**Figure 12**):

- Region I. There were six hits observed. The maximum amplitude was 60 dB and the average frequency varied from 50 to 150 kHz;

- Region II. The AE activity decreased compared to Region I. There were two hits in this region. The maximum amplitude was 65 dB, and the average frequency ranged from 100 to 300 kHz.
- Region III. The AE activity was relatively stable due to the monotonous crack propagation. The main AE signals observed in this region were of 80 dB amplitude and 100–300 kHz average frequency.

3.2. AE monitoring of CVN

3.2.1. Effect of specimen thickness

Figure 14 shows the load-deflection curves obtained during the CVN testing of three specimens with different thicknesses (B = 10, 7.5, and 5 mm) at ambient temperature. Three curves have similar shape, although the load increases with the specimen thickness.

All the specimens exhibited ductile fracture behavior. **Table 4** lists the CVN energy, the load at yield, and the maximum load for three specimens with different thicknesses. As the specimen thickness decreases from 10 to 5.0 mm, the CVN energy decreased from 303.3 to 108.0 J.

In this study, the AE monitoring technique was used to investigate the effect of Charpy specimen thicknesses for the first time. The AE waveforms for 5 mm specimen is shown in **Figure 15**, and the signal parameters for 5 and 7.5 mm thickness are listed in **Table 5**.

It can be found that as the specimen thickness decreases from 7.5 to 5 mm, in Region I, AE signal amplitude decreases from 10 to 8 V, and the average frequency is quite low in the range of 50–100 kHz due to the hammer impact and general yielding. In Region II, a burst AE signal is generated due to the ductile fracture initiation. Amplitude value is in the range of 4–6 V, and

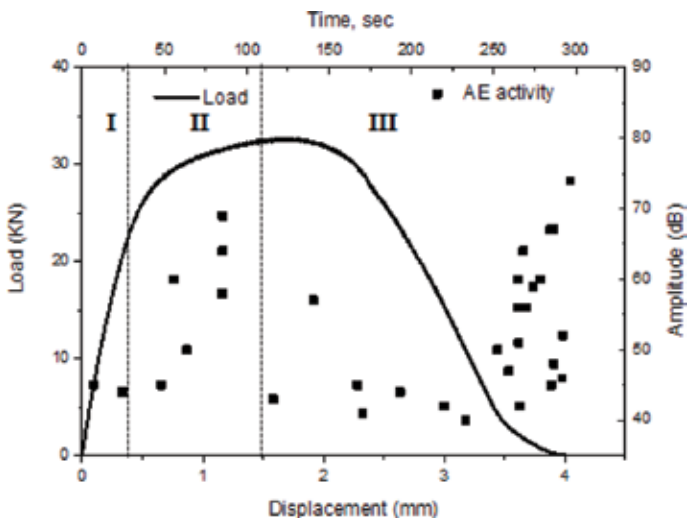

Figure 12. The load-displacement curve and AE activity for X70 steel tested at 2.7×10^{-4} s^{-1}.

the average frequency decreased from 200 to 100 kHz. In Region III, continuous AE signals were observed due to the slightly (slowly) dropped load. The AE amplitude decreased from 8 to 4 V, and the average frequency decreased from 150 to 50 kHz.

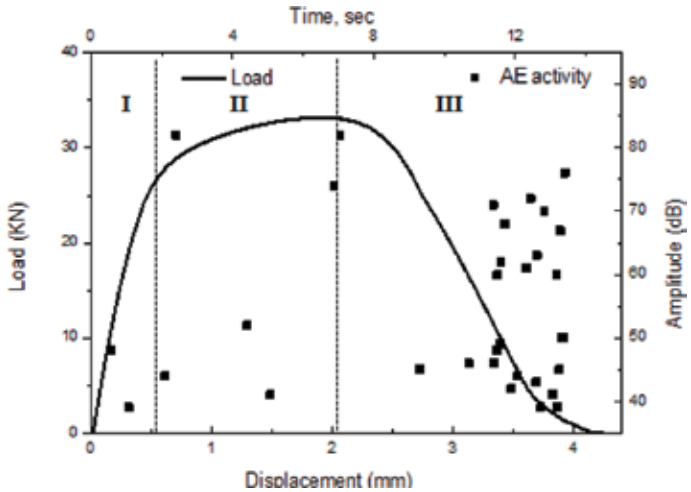

Figure 13. The load-displacement curve and AE activity for X80 steel tested at 2.7×10^{-4} s^{-1}.

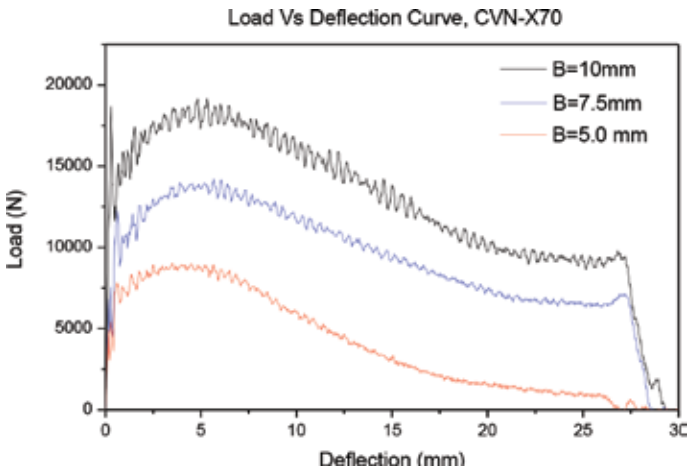

Figure 14. Load-deflection curves obtained during instrumented CVN impact testing at ambient temperature of specimens with various thicknesses.

Specimen thickness, mm	Average CVN energy, J	Load at yield, N	Maximum load, N
10	330.3	14,895	17,990
7.5	197.3	11,150	12,800
5.0	108.0	4810	6105

Table 4. Experimental results for testing at ambient temperature.

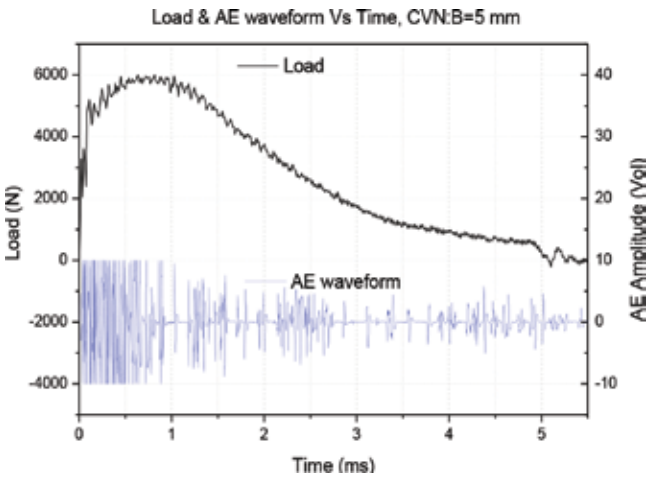

Figure 15. Load and acoustic emission waves versus time for CVN impact test at ambient temperature of 5-mm specimen.

Sample thickness	Region	Amplitude, V	FFT power spectrum frequency peak, kHz	Suggested cause of AE
5.0 mm	I	<6	50–80	The hammer impact and general yielding (A)
	II	4–6	~100	Plastic deformation and ductile fracture (A–B)
	III	2–4	80–100	Ductile fracture propagation (B–C)
7.5 mm	I	<6	75–100	The hammer impact and general yielding (A)
	II	4–6	~150	Plastic deformation and ductile fracture (A–B)
	III	2–4	100–150	Ductile fracture propagation (B–C)

Table 5. The AE waveform parameters during CVN impact test in the studied X70 steel at various thicknesses.

3.2.2. Effect of temperature

Full-size CVN tests have been conducted at seven temperatures. Three representative load-deflection curves are shown in **Figure 16**.

As can be seen in **Figure 16** for 20°C, at the beginning, the load increases with the deflection. At a deflection of 5 mm, the load reaches its maximum and then gradually decreases with deflection. At the final stage of test at a deflection of around 25 mm, the load still remains at quite high value, followed by a quick drop. This behavior is due to the fact that the material is too tough to be fully broken at this temperature.

For the test at −60°C, the maximum load is higher than for 20°C. However, beyond the peak point, the drop of the load at −60°C is much faster than that for 20°C. This indicates a more brittle fracture at −60°C than at 20°C. At the final stage of −60°C test, the load gradually

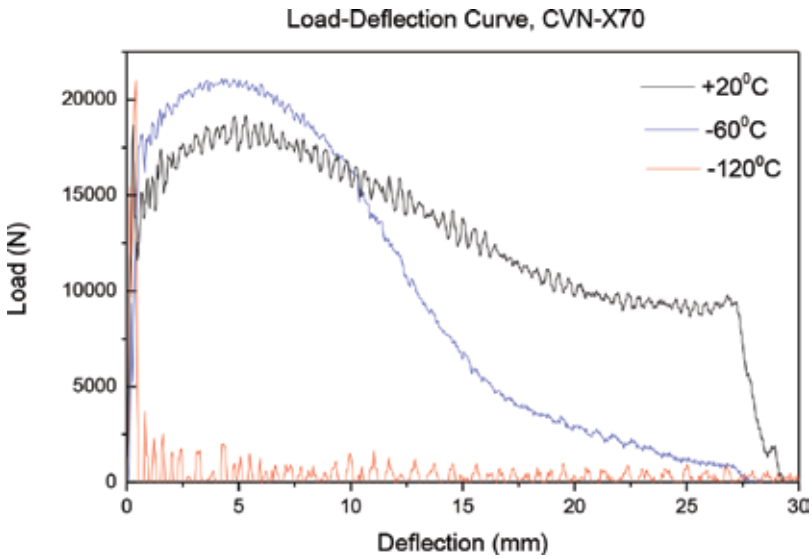

Figure 16. Load-deflection curves of instrumented Charpy impact tests at +20, −60, and − 120°C.

approaches zero. The load for −120°C test temperature reaches its maximum value at a very low defection (around 1 mm) and then rapidly drops to near zero. This clearly indicates brittle fracture mode at this temperature.

It can be seen in **Figure 17**, the fracture surface of the CVN specimen fractured at 20°C is fully ductile with 100% fibrosity. Apparent necking and shear lip areas can be seen. The region close to the notch shows a typical ductile fracture with elongated shearing dimples and micro-voids. The region far from notch also shows ductile fracture, but the dimples are much larger

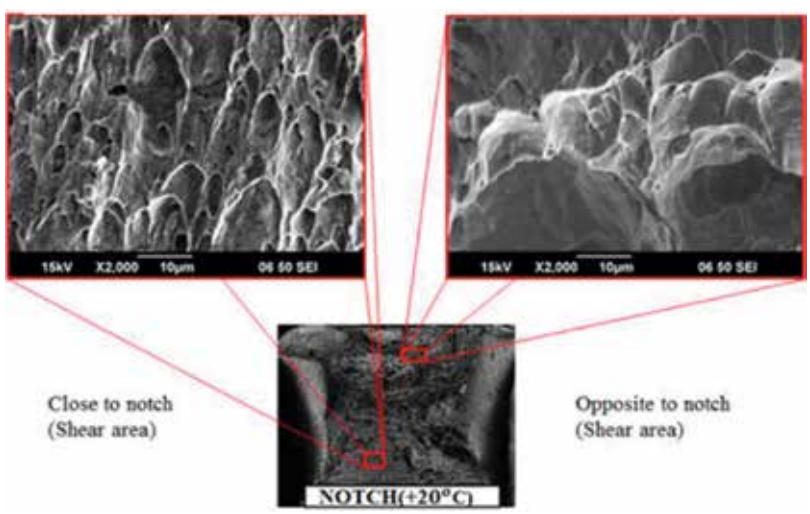

Figure 17. Fracture surface for 10-mm thick CVN specimen tested at +20°C.

in size and much shallower compared to the region close to the notch. The mechanism of ductile crack growth can be characterized by microvoid nucleation, growth, and coalescence. As a specimen is loaded, local strains and stresses at the crack tip support void nucleation. These voids grow as the crack tip blunts and link with the main crack.

The specimen fractured at −60°C shows a half ductile and half brittle type of fracture surface, as can be seen in **Figure 18**. The half close to the notch shows a similar appearance to that of **Figure 18**, with necking, shear lips, elongated dimples, and microvoids. The half close to the final fracture area shows a typical brittle fracture appearance without necking and cleavage facets are observed at high magnification.

AE waves along with the load-time curve for CVN test at −60°C are shown in **Figure 19**. For the AE signal analysis, the load-time curve was divided into three regions: I—before the yield point, II—between the yield point and the peak point, and III—after the peak point till the final fracture.

The general trends are as follows:

- Region I. A high amplitude AE signal is generated from the hammer impact and sample yielding due to a sudden increase in load under elastic condition;
- Region II. A characteristic high-frequency burst in the AE signal is observed. This corresponds to ductile fracture initiation. The phenomenon is observed for a short time between the yield point and the point of maximum load.
- Region III. AE signals generated from fracture propagation are observed. They are of a burst type at high frequency and a continuous type at frequency lower than in Region II; before the end of test, a distinct drop in load was observed that generated a high-frequency burst signal due to the occurrence of brittle fracture.

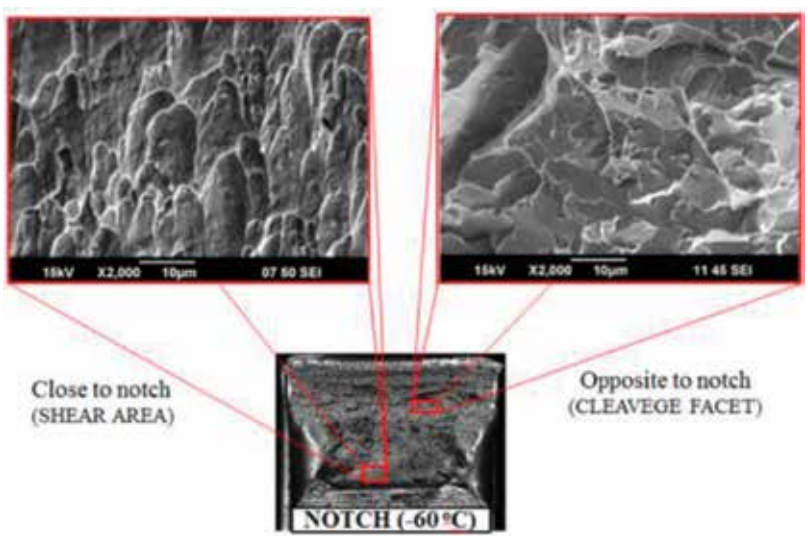

Figure 18. Fracture surface for 10-mm thick CVN specimen tested at −60°C.

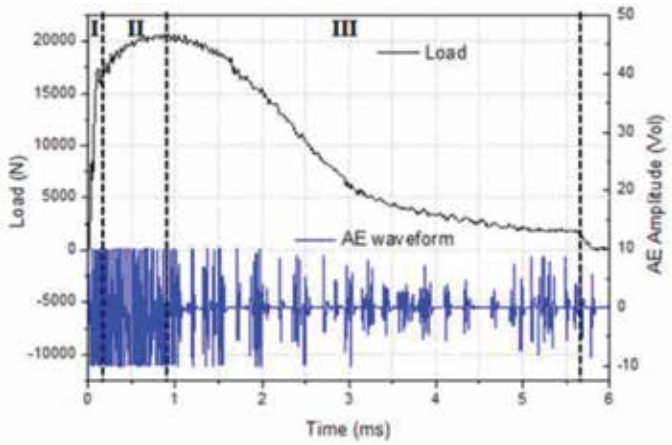

Figure 19. Load-time curve and acoustic emission wave for CVN test at −60°C temperature (B = 10 mm).

Table 6 lists the amplitude and average frequency ranges for each of three regions of the two tests conducted. With a decrease in temperature from ambient to −60°C, the AE average frequency in Region I increased from 50 to 100 kHz. In Region II, strong AE bursts were generated from crack initiation. The AE average frequency increased from 100–200 to 200–250 kHz with a decrease in test temperature. In Region III, the continuous AE signal was related to crack propagation. Although the burst signals dominated due to brittle fracture mode, amplitude increased from 4–6 to 6–8 V and the average frequency increased from 50–100 to 250–350 kHz with a decrease in temperature.

3.2.3. Investigation of fracture initiation

It has been observed by the high-speed camera and AE monitoring of the SENT tests that the fracture does not initiate at the peak load, and it always occurs between the yield point and the peak point, with higher AE amplitude and frequency associated with fracture initiation.

Testing temperature	Region	Amplitude, V	Frequency peak, kHz	Suggested cause of AE
+20°C	I	<8	50–75	The hammer impact and general yielding (A point)
	II	<4–6	100–200	Plastic deformation and ductile fracture (A–B point)
	III	>4	50–150	Ductile fracture propagation (B–C point)
−60°C	I	<8	100–150	The hammer impact and general yielding (A)
	II	4–6	200–250	Ductile fracture and crack propagation (A–B)
	III	6–8	250–350	Brittle fracture (B–C)

Table 6. AE waveform parameters during CVN testing.

http://dx.doi.org/10.5772/intechopen.79325

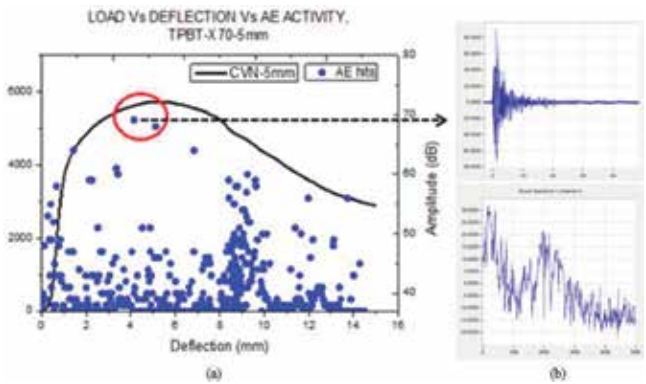

Figure 20. (a) AE activity corresponding to the load-deflection curve obtained during TPBT; (b) selected AE signal waveform and power spectrum corresponding to the fracture initiation for 5-mm thick CVN sample.

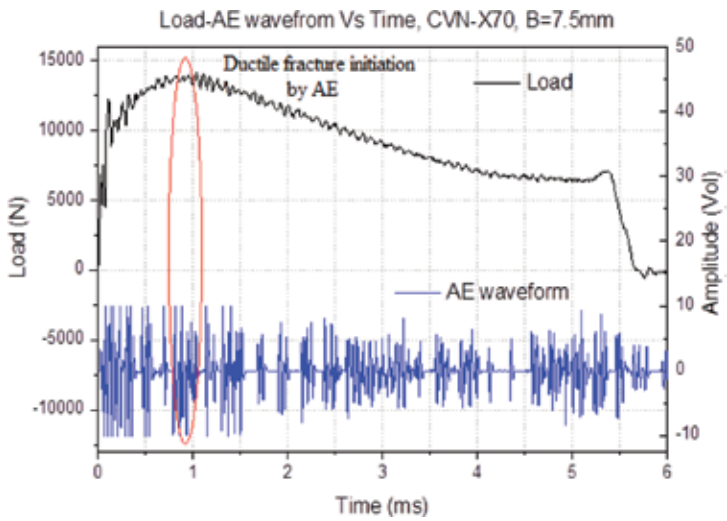

Figure 21. Load-time curve and AE wave for CVN specimen tested at RT, B = 7.5 mm.

In order to further validate the location of fracture initiation, quasi-static three point bending tests (TPBTs) were performed using a tensile test machine.

Figure 20(a) shows the load-deflection curve of the X70 line pipe steel obtained during the TPBT and corresponding AE hit amplitude distribution. It has been found that before the peak load was reached, a strong AE burst with larger amplitude, marked by a circle in the figure, was generated. High-speed video indicated that the fracture initiation was responsible for this AE burst event. **Figure 20(b)** shows this hit waveform and power spectrum. This strong AE signal corresponding to fracture initiation was of 70 dB amplitude and 350 kHz average frequency.

In the CVN test, fracture initiation occurred within a very short time period, and the high-speed camera cannot be installed to observe the fracture behavior of the specimen. Therefore, it is impossible to determine directly the location of fracture initiation in the CVN

load-displacement curve. **Figure 20** shows the results of the CVN tests at room temperature. It can be seen that there are some strong signals before the peak load, marked in red in **Figure 21**. It is evident that these signals related with crack initiation with approximately 10% error.

4. Conclusions

In this chapter, the acoustic emission (AE) monitoring has been shown to accurately reflect the start of plastic deformation, initiation of fracture, and fracture mode (ductile or brittle) during tensile, three-point bend impact, and testing of steels. The AE signal density, amplitude, and frequency could vary by 2–3 times with occurrence of those phenomena. The dependences of absolute values of AE signal parameters on test temperature, loading rate, sample geometry, and fracture mode have been obtained and analyzed. The effect of material chemistry and microstructure on AE activity during testing requires more detailed investigation.

For single edge-notched tension test:

- The AE monitoring technique was used for the first time during the SENT test of X70 and X80 line pipe steels. AE activity started before the yield point, due to the stress concentration at the crack tip and increased before the maximum load was reached, due to the fracture initiation. Toward the end of the test, the AE hit density increased, due to the multiple fracture;
- With an increase in strain rate, the AE activity increased.
- The fracture initiation point can be detected by a sudden change in the AE activity. The fracture initiation in the studied steel was marked by the AE signal with 65–75 dB amplitude and a 300–350 kHz average frequency prior to the maximum load point.

For Charpy V-notch test:

- With test temperature decreasing the average frequency of the burst-type AE signals increased. The ductile-to-brittle transition temperature (DBTT) was found to be in the range of −60 to −80°C for the tested steel. A sudden drop in the load observed at −60°C occurred due to the brittle fracture and generated a 350 kHz average frequency burst-type AE signal;
- Charpy specimens with various thicknesses were tested for the first time using the AE monitoring technique. With a decrease in specimen thickness from 10 to 5 mm, the AE average frequency decreased from 150 to 50 kHz;
- It was impossible to observe directly the fracture initiation in the CVN test. The quasi-static three-point bending tests using the same specimens were carried out. The fracture initiated before the peak load was reached. In the CVN tests, strong AE signals were observed before the peak load, and these are believed to correspond to fracture initiation;
- The fracture mode during impact testing can be predicted using AE waveform and power spectra methodologies. In this work, 50–200 kHz frequency signals corresponded to ductile fracture and 250–350 kHz frequency signals corresponded to brittle fracture.

Acknowledgements

This work was supported by the Energy Pipeline CRC, through the Australian Government's Cooperative Research Centre Program. The funding and in-kind support from the APGIA RSC is gratefully acknowledged. The authors are thankful to Electron Microscopy Centre at the University of Wollongong for providing access to the JEOL JSM-6490LA scanning electron microscope.

Author details

Turbadrakh Chuluunbat[1]* and Andrii Kostryzhev[2]

*Address all correspondence to: turbadrakh@mandakh.mn

1 Department of Science and Engineering, Mandakh University, Ulaanbaatar, Mongolia

2 School of Mechanical, Materials, Mechatronic and Biomedical Engineering, University of Wollongong, Australia

References

[1] Miller RK. Acoustic Emission Testing. The McGraw-Hill Companies; 2003

[2] Gross CU, Ohtsu M. Acoustic Emission Testing. Heidelberg, Berlin: Springer; 2008

[3] Muravin B, Carlos MF. Guide for development of acoustic emission application for examination of metal structure. Journal of Acoustic Emission. 2011;**29**:142-148

[4] Kostryzhev AG. Detection of crack growth in rail steel using acoustic emission. Ironmaking and Steelmaking. 2012;**2**:1-6

[5] Wevers M. Listening to the sound of materials: Acoustic emission for the analysis of material behavior. NDT and E International. 1997;**30**:99-106

[6] Hellier C. Handbook of Nondestructive Evaluation. New York, London: McGraw-Hill; 2001

[7] Ingham T. Acoustic emission characteristics of steels part 1: Acoustic measurements from tensile tests. International Journal of Pressure Vessels and Piping. 1974;**2**:31-50

[8] Vallen H. Acoustic Emission Testing Fundamentals, Equipment, Applications. The e-Journal of Nondestructive Testing. 2002;**7**:9-10

[9] Dunegan HL. Factors affecting acoustic emission response from materials. ASTM Acoustic Emission Standards. 1972;**2**:100-113

[10] Tonolini F. General review of developments in acoustic emission methods. International Journal of Pressure Vessels and Piping. 1987;**28**:179-201

[11] Crutzen S. Developments in fracture mechanics and non-destructive examination. Nuclear Engineering and Design. 1992;**134**:59-86

[12] Kostryzhev AG. Acoustic emission monitoring of split formation during Charpy impact testing of high strength steel. Materials Science and Technology. 2012;**28**:240-242

[13] Ono K. Current understanding of mechanisms of acoustic emission. Journal of Strain Analysis for Engineering Design. 2005;**40**:1-15

[14] Muravin B. Acoustic emission science and technology. Journal of Building and Infrastructure Engineering of the Israeli Association of Engineers and Architects. 2009;**1**:4-5

[15] Eitzen DG, Wadley HNG. Acoustic emission: Establishing the fundamentals. Journal of Research of the National Bureau of Standards. 1984;**89**:75-100

[16] Frederick JR, Felbeck DK. Dislocation motion as a source of acoustic emission. ASTM Acoustic Emission Standards. 1972;**78**:129-139

[17] Carpenter SH, Higgins FP. Sources of acoustic emission generated during the plastic deformation of 7075 aluminum alloy. Metallurgical Transactions A. 1977;**8**:1629-1632

[18] Barat K. Low temperature tensile deformation and acoustic emission signal characteristics of AISI 304LN stainless steel. Materials Science and Engineering A. 2013;**597**:37-45

[19] Roberts TM. Acoustic emission monitoring of fatigue crack propagation. Journal of Constructional Steel Research. 2003;**59**:695-712

[20] Mukhopadhyay CK. Study of tensile deformation behaviour of M250 grade maraging steel using acoustic emission. Journal of Materials Science. 2010;**45**:1371-1384

[21] Mukhopadhyay CK. The influence of notch on the acoustic emission generated during tensile testing of nuclear grade AISI type 304 stainless steel. Materials Science and Engineering A. 2000;**276**:83-90

[22] Kral Z. Crack propagation analysis using acoustic emission sensors for structural health monitoring systems. Scientific World Journal. 2013;**2013**:1-4

[23] Han Z. Effects of strain rate and notch on acoustic emission during the tensile deformation of a discontinuous yielding material. Materials Science and Engineering A. 2011; **528**:4372-4380

[24] Blanchette Y, Dickson JI. Acoustic emission behaviour during crack growth of 7075-T651 AI alloy. Engineering Fracture Mechanics. 1986;**24**:647-656

[25] Fallahi A. Monitoring of the deformation and fracture process of dual phase steels employing acoustic emission techniques. Materials Science and Engineering A. 2012; **548**:183-188

[26] Ohtsu M, Ono K. AE source location and orientation determination of tensile cracks from surface observation. International Nondestructive Testing. 1988;**21**:143-150

[27] Roy H. Acoustic emissions during fracture toughness tests of steels exhibiting varying ductility. Materials Science and Engineering A. 2008;**486**:562-571

[28] Clark G, Knott JF. Acoustic emission and ductile crack growth in pressure-vessel steels. Metal Science. 1977;**6**:531-536

[29] Wadley HNG. Acoustic emission for physical examination of metals. International Metals Reviews. 1980;**2**:41-64

[30] Mostafavi S. Acoustic emission methodology to evaluate the fracture toughness in heat treated AISI D2 tool steel. Journal of Materials Engineering and Performance. 2011; **21**:2103-2116

[31] Chuluunbat T, Koztryzhev AG. Influence of loading conditions during tensile testing on acoustic emission. Key Engineering Materials. 2014;**626**:121-126

[32] Mukhopadhyay CK. Acoustic emission during fracture toughness tests of SA333 Gr.6 steel. Engineering Fracture Mechanics. 2012;**96**:294-306

[33] Yusof MFM. Acoustic emission behavior during fatigue crack of API5LX70 gas pipeline steel. Applied Mechanics and Materials. 2011;**80**:148-152

[34] Richter H. The use of acoustic emission to determine characteristic dynamic strength and toughness properties of steel. Nuclear Engineering and Design. 1999;**188**:241-254

[35] Tronskar JP. Application of acoustic emission for measuring crack initiation toughness in instrumented Charpy impact testing. Journal of Testing and Evaluation. 2003;**31**:222-233

[36] Fearnehough GD. Fracture propagation control in gas pipelines: A survey of relevant studies. International Journal of Pressure Vessels and Piping. 1974;**2**:257-282. DOI: 10.1016/0308-0161(74)90007-6

[37] Rivalin F. Ductile tearing of pipeline steel wide plates I. Dynamic and quasi-static experiments. Engineering Fracture Mechanics. 2001;**68**

[38] Cravero S, Ruggieri C. Correlation of fracture behavior in high pressure pipeline with axial flaws using constraint designed test specimens-Part 1: Plane-strain analysis. Engineering Fracture Mechanics. 2005;**72**:1344-1360

[39] DNV-P-F108. Fracture Control for Pipeline Installation Methods: Introducing Cyclic Plastic Strain. Norway: Det Norske Veritas; 2006

[40] Australian-Standard-1544.2. Method for Impact Tests on Metals. Part 2: Charpy V-Notch. Sydney: Standards Australia International Ltd.; 2003

Section 2

Vibrations Advanced Testing

Chapter 3

Effect of Various Edge Conditions on Free-Vibration Characteristics of Isotropic Square and Rectangular Plates

Muzamal Hussain and Muhammad Nawaz Naeem

Additional information is available at the end of the chapter

http://dx.doi.org/10.5772/intechopen.80672

Abstract

In this chapter, vibrations of isotropic rectangular plates have been analyzed by applying the wave propagation approach. The plate problem has been expressed in integral form by considering the strain and kinetic energies. The Hamilton's principle has been applied to transform the integral form into the partial differential equation of second order. The classical method namely product method has been used to separate independent variables. The partial differential equation has converted into the ordinary differential equations. The axial wave numbers are associated with particular boundary conditions. This is an approximate technique, which is based on eigenvalues of characteristic beam functions. The natural frequencies of plates are investigated versus modal numbers by varying the length and width of the plates with simply supported-simply supported (SS-SS), clamped-clamped (CC-CC), and simply supported-clamped (SS-CC) boundary conditions. The frequencies of the plates increase by increasing the modal number, and CC-CC frequencies are greater than the frequencies of other boundary conditions. Computational computer software MATLAB is engaged to characterize the frequencies. The results are compared with the earlier simulation work in order to test the accuracy and efficiency of the present method.

Keywords: rectangular plates, wave propagation approach, edge conditions, vibration

1. Introduction

Beams, plates, and shells are three main structural elements. Plates are widely used in various areas of engineering science like aerodynamics, civil and hydraulic instruments, vessels, mechanical structures, etc. Dynamical loading is applied on plates when they are involved in

a physical system. Their dynamical behavior is studied theoretically. Vibration is an important feature of plates, having a critical role in applied field of engineering, which is investigated by researchers. A classical study of flexural vibrations of rectangular plates was performed by Mindlin et al. [1]. Leissa [2] compiled a book on vibration and buckling problems of the rectangular plates. He derived their natural frequencies. In the present study, vibrations of rectangular plates are analyzed by applying the wave propagation approach. This is an approximate technique which is based on eigenvalues of characteristic beam functions. Plates are structural elements that are frequently subjected to vibration, and controlling the frequency at which a plate vibrates is very important to structural designers. Free-vibration analyses of thin rectangular plates that are clamped on all edges have been studied by many researchers in the past with the aim of calculating its natural frequencies, and they have done using numerical approaches. Plates are important elements in various fields of engineering science and technology. Their extensive uses are found in aerodynamics, civil structures, hydraulic structures, containers, ships, instruments, and machine parts. Dynamical loadings are exerted on plates when they are involved in a physical system.

The theoretical vibration analysis is performed to approximate experimental values to evade any future complications. Many researchers [3–10] have worked on vibration characteristics of plates. For several decades, numerous measurements of vibrational properties and the vibrational behavior issues of plates have been studied in addition to different theories [10–12].

Natural frequencies for vibrating rectangular plates are obtained for various boundary conditions. Sakiyama and Huang [13] presented the vibration study of rectangular plates. The thickness of plates was variable. They based their analysis on the Green function method and obtained frequency spectra. They obtained some preliminary results for vibrations of plates. A best theoretical review on plates and shells has been presented by Ventsel and Krauthammer [14] using Galerkin method to carry out free-vibration analysis of SS-SS plate. Zhang et al. [15] presented a coupled structural-acoustic analysis for cylindrical shells having fluid inside them. They applied the wave propagation method for solving shell motion equations.

Werfalli and Karoud [16] conducted a vibration analysis of thin isotropic rectangular plates for number of end conditions. This study involved determination of their natural frequencies by applying the Galerkin method. Frequencies were obtained for a number of aspect ratios. They have discussed the formation of differential equations for plates and their analytical solutions. Hsu [17] applied a new version of differential quadrature technique to analyze vibrations of rectangular plates which rested on material foundations of elastic nature and carried any number of sprung masses. It was inferred that vibration characteristics of these types of plates can be studied for carrying any number of sprung masses and resting on the elastic foundations. Zhou and Ji [12] studied vibrations of rectangular plates associated with distributions of springs in uniform and continuous manner in a domain of rectangular nature. The Chebyshev polynomials in a series were taken to represent trial functions. Comparisons of natural frequencies verified accuracy and extensive applicability of the applied approach. From the results, it was noted that the natural frequencies and modes were exited in couples.

Mansour et al. [18] gave a theoretical wave propagation method to study vibrations of rectangular Kirchhoff plates. The direct exact solutions were obtained by Xing and Liu [11]. They

applied method of separation of variables to solutions of the plate eigenvalue equation in exact shape. This solution procedure met the motion equation in the eigenvalues form and could be used for any kind of end conditions. Lal et al. [19] presented an analysis and numerical results for vibration characteristics of hetero-homogeneous rectangular plates with uniform thickness. The Rayleigh-Ritz technique method was used to solve the plate equation. Characteristic orthogonal polynomials were used for four conditions of clamped, simply supported, and free ends with mixed forms. The Gram-Schmidt procedure was used to produce orthogonal polynomials meeting end conditions. Sun et al. [20] used wave propagation approach to analyze vibrations of thin rotating circular cylinders. Njoku et al. [21] used Taylor series peculiar shape functions for clamped-clamped isotropic thin rectangular plates and applied Galerkin functional to determine the fundamental frequencies of the vibrating plate.

Recently, the vibrational behaviors of plates have been reported in Refs. [22–26]. However, up to now, little is known about the vibrational properties of plates and moreover the effects of the geometrical/material parameters by using extensive wave propagation approach (WPA).

In this chapter, the WPA proposed by Zhang et al. [15] for computing the vibrations is extended to plates, which is our particular motivation. Increasingly, numerical calculations have been used to investigate vibrational properties of plates through different models [5, 9, 12, 13, 21]. The method of choice is based on WPA that allows for the study of fundamental frequencies of plates over various combinations of geometric parameters, and this approach has become increasingly popular in the numerical solution of engineering applications. There are many theoretical and numerical techniques that have been used for vibration problems of plates such as Rayleigh-Ritz [19], differential quadrature method [17], Galerkin's technique [16, 21, 27], WPA [15, 28], finite element method [23], and structural element method (SEM) [29]. Despite of its conceptual simplicity, the continuum models and Galerkin's technique are subject to several computational problems which have to be addressed. The WPA was found to be a very popular tool to compute the vibrational properties of plates. Recently, the strong formulation of WPA has been applied for investigations fundamental frequencies of single-walled carbon nanotubes and detailed discussion is given in our earlier published work [30–32]. The present model based on WPA is, therefore, another choice of powerful numerical technique, whose results are appropriate in the limit of acceptable statistical errors than the earlier used Raleigh-Ritz [19] and Galerkin's techniques [16, 21].

The main objective of the present work is to generalize a modified model based on WPA first time and is determine how to calculate the frequencies of plates under various boundary conditions. In our case, the WPA is applied to solve the presented dynamical equations. The natural frequencies of plates are investigated versus modal numbers by varying the length and width of the plates with simply supported-simply supported (SS-SS), clamped-clamped (CC-CC), and simply supported-clamped (SS-CC) boundary conditions. The frequencies of the plates increase by increasing the modal number and CC-CC frequencies are greater than the frequencies of other boundary conditions. Computational computer software MATLAB is engaged to characterize the frequencies. The results are compared with the earlier simulation/method in order to test the accuracy and efficiency of the present method.

2. Formulation

Consider **Figures 1** and **2** representing a rectangular plate made with length '*a*,' width '*b*' and thickness '*h*' as geometrical parameters and Young's modulus *E*, Poisson's ratio υ and mass density ρ as material parameters. A coordinate system has set at middle reference of the rectangular plate with '*x*' and '*y*' as coordinates along *x*- and *y*-axis, respectively, in *xy*-plane for the cases of simply supported-simply supported (SS-SS), clamped-clamped: clamped-clamped boundary conditions as shown in **Figures 1** and **2**.

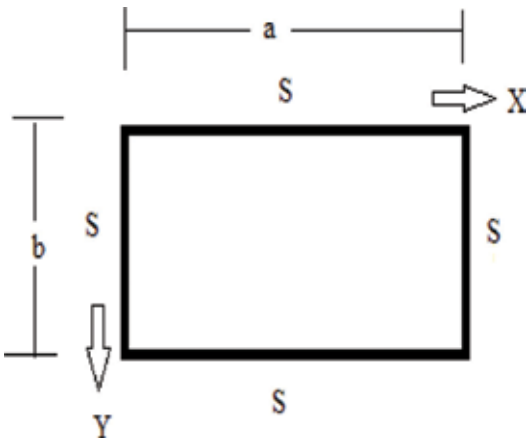

Figure 1. SS-SS plate.

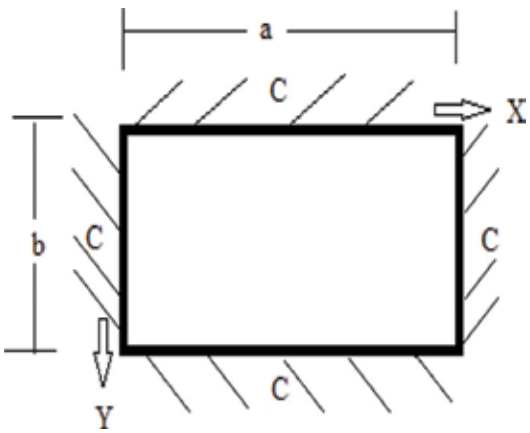

Figure 2. CC-CC plate.

http://dx.doi.org/10.5772/intechopen.80672

2.1. Governing equation of thin plate model

Consider a rectangular plate whose geometrical dimensions are '*a*' and '*b*.' Its thickness is denoted by *h*. Then, *a*, *b*, and *h* are called its geometrical parameters. Its material parameters are *E*, modulus of elasticity; *h*, plate thickness; *v*, Poisson's ratio; *ρ*, density; Young's modulus, *E*; *v*, Poisson's ratio; and *ρ*, mass density. Suppose that *w (x,y,t)* designates the deformation displacement out of the plane of motion in the transverse direction. The strain energy, *U*, of this rectangular plate when it is vibrating, is expressed as:

$$U = \frac{1}{2}\int_0^b \int_o^a D\left(\frac{\partial^2 w(x,y,t)}{\partial x^2} + \frac{\partial^2 w(x,y,t)}{\partial y^2}\right)^2 dxdy \tag{1}$$

The expression for kinetic energy, *T* for the rectangular plate is written as:

$$T = \frac{1}{2}\rho h \int_0^b \int_0^a \left(\frac{\partial^2 w(x,y,t)}{\partial t}\right)^2 dxdy \tag{2}$$

Here *t* denotes the time variable, $D = \frac{Eh^3}{12(1-v^2)}$ designates the flexural rigidity, *E* is Young's modulus, *ρ* is the density of the plate material, and *h* is the rectangular plate thickness. The Lagrangian energy variational functional is formulated by considering the expressions for the strain and kinetic energies of the vibrating rectangular pate and is written as:

$$\prod = T - U \tag{3}$$

For deriving, pate governing equation is obtained by applying the Hamiltonian variational principle [33]. This principle states that during very short interval of time, the change in the Lagrange functional is minimized. So using this principle to the expression (3), we get the following:

$$\int_{t_1}^{t_2} \delta\left(\prod\right) dt = 0 \tag{4}$$

Further, it can be written as:

$$\int_{t_1}^{t_2} \delta(T - U) dt = 0 \tag{5}$$

This process furnishes the governing equation that states the flexural vibration for the rectangular plates as:

$$\frac{\partial^4 w(x,y,t)}{\partial x^4} + 2\frac{\partial^4 w(x,y,t)}{\partial x^2 \partial y^2} + \frac{\partial^4 w(x,y,t)}{\partial y^4} + \frac{\rho h}{D}\frac{\partial^2 w(x,y,t)}{\partial t^2} = 0 \tag{6}$$

Usually, energy variational methods are applied to investigate the vibration characteristics of structural elements namely: beams, plates, and shells. These methods consist of the Rayleigh-Ritz method [19] and the Galerkin method [16, 21]. When a vibrating problem is written in the integral form, the Rayleigh-Ritz technique is applied. When this problem is in the form of differential equations, the Galerkin procedure is applied. In both these techniques, axial modal dependence is assumed by different of mathematical functions which meet the boundary conditions described on the ends of structural elements. Frequently, beam functions are exploited for this purpose. These functions are obtained from the solutions of the beam differential equation for various end conditions.

The differential equation for a vibrating beam is written as:

$$\frac{\partial^4 w}{\partial x^4} + \alpha^4 \frac{\partial^2 w}{\partial t^2} = 0 \tag{7}$$

The general solution of the equation for the wave deformation displacement ω of the beam vibration can be written as:

$$w = \left\{A_1 e^{k_m x} + A_2 e^{-k_m x} + A_3 e^{ik_m x} + A_4 e^{-ik_m x}\right\} e^{i\omega t} \tag{8}$$

where k_m is the axial wave number whose value depends upon boundary conditions applied at the beam ends. ω is the natural angular frequency of the beam. In the solution (8), there are four terms which are functions of the axial variable, x. They represent the negatively decaying evanescent wave, the positively wave, the negatively propagating wave, and the positively propagating wave. Determination of values of $A_i^{'}s$ and the axial wave mode k_m are associated with edge conditions. Moreover, they are related to the eigenvalues of characteristic beam functions.

Expression (8) may further be written in the following:

$$w = \{B_1 \cos(k_m x) + B_2 \sin(k_m x) + B_3 coh(k_m x) + B_4 \sinh(k_m x)\} e^{i\omega t} \tag{9}$$

For wave propagation approach, this expression is truncated and is taken as:

$$w = e^{-ik_m x} e^{i\omega t} \tag{10}$$

This is illustrated by the example of boundary conditions viz., simple supported—simply supported. Application of these boundary conditions generates the trigonometric equation: $\sin(k_m d) = 0$. Infinite solution of this equation gives $k_m d = m\pi$, where m is the number of the axial standing waves and d is the dimension of the rectangular plate. Hence for a complete simply supported rectangular plate on four ends, $k_m = \frac{m\pi}{a}$ and $k_n = \frac{n\pi}{b}$ are used to evaluate natural frequency of the plate for the vibration parameters, m and n. Here, a and b are the dimensions, that is, length and width of the rectangular plate.

http://dx.doi.org/10.5772/intechopen.80672

2.2. Application of wave propagation approach

Area of determination of solutions of plate equation describing vibration phenomenon has been remained an attractive interests of mathematicians and engineers for their applied aspects. A comprehensive material on plate solutions has been compiled by Leissa [2]. The present era has been said to be the era of computer and its applications. The invention of computer has made the mathematical computational process very simple, and complicated expressions are simplified by applying computer software packages like Mathematica, Matlab, Maple, etc. Various numerical techniques are available to solve the differential equations found in engineering fields. With new developments in the world of computer science, complicated problems encountered in the areas of engineering and technology have been solved very easily and in efficient way. Linear and nonlinear differential equations have solved by the finite difference method, Rayleigh-Ritz method, the Galerkin method, finite element method, Fourier series method, and boundary element method. Ultimately, there are numerous commercially developed software packages. It is the basic interest of a researcher to apply a method which implicate less time and labor. This concept leads to develop a new technique which is more efficient and simple and provides accurate results. It has been seen that in the recent years, the wave propagation approach has been employed successfully to solve a number of shell and tube problems [28, 30–32]. Application of this approach reduces the differential equations in simple algebraic equations. For the present plate problem, this procedure is used to get the plate eigenvalue equation.

Modal displacement functions. For classical solutions of partial differential equations, method of separation of variables is employed to split the independent variables. In the governing differential equation of motion for rectangular plates, three independent variables are involved viz., two space variables x, y and one time variable, t. For splitting variables, the following modal displacement function forms are adopted:

$$w(x,y,t) = X(x)Y(y)\sin\omega t \tag{11}$$

or

$$w(x,y,t) = X(x)Y(y)\cos\omega t \tag{12}$$

or

$$w(x,y,t) = X(x)Y(y)e^{-i\omega t} \tag{13}$$

where $X(x)$ and $Y(y)$ are unknown functions. They are taken from algebraic functions and assumed to meet boundary conditions. A trigonometric function or an exponential complex function represents harmonic response. When modal form (7) or (8) or (9) is substituted in the equation of motion of plates,

$$\frac{\partial^4 X}{\partial x^4} + 2\frac{\partial^2 X}{\partial x^2}\frac{\partial^2 Y}{\partial y^2} + \frac{\partial^4 Y}{\partial y^4} = \frac{\rho h\omega^2}{D} \tag{14}$$

For wave propagation approach, the space modal functions $X(x)$ and $Y(y)$ are supposed to be the following forms:

$$X(x) = e^{-ik_m x} \tag{15}$$

and

$$Y(y) = e^{-ik_n y} \tag{16}$$

where k_m and k_n are axial mode wave numbers, and their values depend on the nature of boundary conditions specified at the plate four ends.

Making substitutions of expressions (14) and (15) in Eq. (13), we get

$$\frac{\partial^4\left(e^{-ikmx}\right)}{\partial x^4} + 2\frac{\partial^2\left(e^{-ikmx}\right)}{\partial x^2}\frac{\partial^2\left(e^{-ikny}\right)}{\partial y^2} + \frac{\partial 4\left(e^{-ikn}\right)}{\partial y^4} = \frac{\rho h\omega^2}{D} \tag{17}$$

or

$$k_m^4 + 2k_m^2 k_n^2 + k_n^4 = \frac{\rho h\omega^2}{D} \tag{18}$$

or

$$\frac{\rho h\omega^2}{D} = \left[k_m^4 + 2k_m^2 k_n^2 + k_n^4\right] \tag{19}$$

or

$$\frac{\rho h\omega^2}{D} = \left[k_m^2 + k_n^2\right]^2 \tag{20}$$

So the frequency equation for rectangular plates is obtained as:

$$\omega = \sqrt{\frac{D}{\rho h}}\left[k_m^2 + k_n^2\right] \tag{21}$$

2.3. Boundary conditions

By applying the Hamilton's principle [33] to the Lagrangian energy variational functional, the simply supported conditions are described as:

$$\Phi_m(x) = \frac{d^2\Phi_m(x)}{dx^2} = 0$$

at $x = 0$, *or* $x = L$

http://dx.doi.org/10.5772/intechopen.80672

and clamped condition is defined as:

$$\Phi_m(x) = \frac{d\Phi_m(x)}{dx} = 0$$

at $x = 0$ or $x = L$

and free condition is stated as:

$$\frac{\Phi^2{}_m(x)}{dx^2} = \frac{d^3\Phi_m(x)}{dx^3} = 0$$

at $x = 0$ or $x = L$.

Most of the vibration analysis of rotating functionally graded cylindrical shell with ring supports has been performed using the simply supported boundary conditions. In this case, the axial deformation displacement is estimated by the trigonometric functions, that is:

$$U(x) = \frac{d\Phi_m(x)}{dx} = \cos(m\pi x/L)$$

$$V(x) = W(x) = \Phi_m(x) = \sin(m\pi x/L)$$

Differential equations represent a physical problem and involve unknown functions. These functions are determined by applying some constraints on the boundary of solutions. These conditions are called boundary conditions. Plate vibration is an initial-boundary value problem and is transformed into the boundary value problem and four boundary conditions are described at four ends of a rectangular plate. For a rectangular plate with edges a and b, there are eight physical boundary conditions:

i. Fully simply supported end conditions

$$w(0,y,t) = 0, \frac{\partial^2 w(0,y,t)}{\partial x^2} = 0, w(a,y,t) = 0, \frac{\partial^2 w(a,y,t)}{\partial x^2} = 0 \tag{22}$$

$$w(x,0,t) = 0, \frac{\partial^2 w(x,0,t)}{\partial y^2} = 0, w(x,b,t) = 0, \frac{\partial^2 w(x,b,t)}{\partial y^2} = 0 \tag{23}$$

ii. Clamped-clamped end condition

$$w(0,y,t) = 0, \frac{\partial w(0,y,t)}{\partial x} = 0, w(a,y,t) = 0, \frac{\partial w(a,y,t)}{\partial x} = 0 \tag{24}$$

$$w(x,0,t) = 0, \frac{\partial w(x,0,t)}{\partial y} = 0, w(x,b,t) = 0, \frac{\partial w(x,b,t)}{\partial y} = 0 \tag{25}$$

iii. Two opposite ends simply supported and other two ends clamped

$$w(0,y,t)=0,\ \frac{\partial^2 w(0,y,t)}{\partial x^2}=0,\ w(a,y,t)=0,\ \frac{\partial^2 w(a,y,t)}{\partial x^2}=0 \tag{26}$$

$$w(x,0,t)=0,\ \frac{\partial w(x,0,t)}{\partial y}=0,\ w(x,b,t)=0,\ \frac{\partial w(x,b,t)}{\partial y}=0 \tag{27}$$

iv. Fully free end conditions

$$\frac{\partial^2 w(0,y,t)}{\partial x^2}=0,\ \frac{\partial^3 w(0,y,t)}{\partial x^3}=0,\ \frac{\partial^2 w(a,y,t)}{\partial x^2}=0,\ \frac{\partial^3 w(a,y,t)}{\partial x^3}=0 \tag{28}$$

$$\frac{\partial^2 w(x,0,t)}{\partial y^2}=0,\ \frac{\partial^3 w(x,0,t)}{\partial y^3}=0,\ \frac{\partial^2 w(x,b,t)}{\partial y^2}=0,\ \frac{\partial^3 w(x,b,t)}{\partial x^3}=0 \tag{29}$$

v. Clamped at two ends and free other two ends

$$w(0,y,t)=0,\ \frac{\partial w(0,y,t)}{\partial x}=0,\ w(a,y,t)=0,\ \frac{\partial w(a,y,t)}{\partial x}=0 \tag{30}$$

$$\frac{\partial^2 w(x,0,t)}{\partial y^2}=0,\ \frac{\partial^3 w(x,0,t)}{\partial y^3}=0,\ \frac{\partial^2 w(x,b,t)}{\partial y^2}=0,\ \frac{\partial^3 w(x,b,t)}{\partial y^3}=0 \tag{31}$$

2.4. Frequency equation for various boundary conditions

Using axial wave numbers, various frequency formulas can be formed for a number of boundary conditions.

1. SS-SS

$$\omega=\frac{\pi^2}{a^2}\sqrt{\frac{D}{\rho h}}\left[m^2+\frac{n^2a^2}{b^2}\right] \tag{32}$$

2. SS-SS and CC-CC

$$\omega=\frac{\pi^2}{a^2}\sqrt{\frac{D}{\rho h}}\left[m^2+\left(\frac{2n+1}{2}\right)^2\frac{a^2}{b^2}\right] \tag{33}$$

3. CC-CC and CC-CC

$$\omega=\frac{\pi^2}{4a^2}\sqrt{\frac{D}{\rho h}}\left[(2m+1)^2+(2n+1)^2\frac{a^2}{b^2}\right] \tag{34}$$

4. SS-C and SS-C

$$\omega = \frac{\pi^2}{16a^2}\sqrt{\frac{D}{\rho h}}\left[(4m+1)^2 + (4n+1)^2\frac{a^2}{b^2}\right] \tag{35}$$

3. Results and discussion

According to various support conditions (CC-CC, SS-CC, and SS-SS), the fundamental frequencies (Hz) of the plate have been studied using wave propagation approach. The obtained results are discussed and compared with earlier theoretical results and simulation methods using same sets of material and geometrical parameters. In addition to these, as a final case study, the effect of CC-CC, SS-CC, and SS-SS for two sorts of plates (square and rectangular) is calculated and investigated. Their material properties, E, ν, and ρ, for isotropic plate are $2.07788 \times 10^{11} N/m^2$, 0.317756, and $8166 Kg/m^3$ [23], and boundary condition is specified in Ref. [31]. Here, a number of results are presented for vibrating rectangular isotropic plates. The vibration frequency equation for the plate has been obtained in terms of vibration, geometrical, and material parameters. The wave propagation approach has been applied for various boundary conditions. For the accuracy and stability of the present method, the findings are in good agreement with the existing results.

Tables 1 and **2** show the comparison of natural frequencies of simply supported square plate with FEM [23] and SEM [29]. As the number of modes increases, the frequencies also increase. This comparison shows that present approach is efficient to find the vibration of plates.

In **Tables 3–5**, the frequencies for a vibrating rectangular plate have been evaluated for modal parameters (m, n). It is observed that as m is kept fixed, n is allowed to vary, the frequency for the square plate is increased. Here, behavior of natural frequencies has been shown for a SS-SS,

	Frequencies (THz)		
Modes	**Present**	**FEM [23]**	**SEM [30]**
(1, 1)	4.845	4.857	4.866
(1, 2)	12.11	12.14	12.16
(2, 2)	19.28	19.43	19.46
(1, 3)	24.19	24.28	24.28
(2, 3)	31.41	31.57	31.6
(4, 1)	41.10	41.26	41.3
(3, 3)	43.61	43.71	43.75

Table 1. Convergence of natural frequencies (Hz) with FEM and SEM of simply supported square plate.

	Frequencies (THz)		
Modes	**Present**	**FEM [31]**	**SEM [32]**
(1, 1)	55.10	55.13	55.15
(1, 2)	55.52	55.73	55.75
(2, 2)	56.42	56.62	56.67
(1, 3)	65.50	65.52	65.59
(2, 3)	69.68	69.60	69.68
(4, 1)	77.12	77.19	77.30
(3, 3)	83.04	83.18	83.33

Table 2. Convergence of natural frequencies (Hz) with FEM and SEM of clamped square plate.

CC-CC, and SS-CC rectangular plate with regard to geometrical and material parameters. The frequencies of CC-CC plate are greater than that of SS-CC and SS-SS.

Figures 3 and **4** show the variation of frequencies versus modal wave number. **Figure 3** is drawn for the square plate when we take $a = b = 3$ m and $m = 1, 2$, $n = 1 \sim 5$ with various boundary conditions and show the influence of these conditions. As the constraints in the end conditions are applied more, the frequencies increase. It has been seen that the frequency is

Modal parameter (*m*, *n*)	ω	***f*(Hz)**	**Modal parameter (*m*, *n*)**	ω	***f*(Hz)**	**Modal parameter (*m*, *n*)**	ω	***f*(Hz)**
(1, 1)	152.66	24.2972	(2, 1)	381.66	60.743	(3, 1)	763.32	121.486
(1, 2)	381.65	60.743	(2, 2)	610.656	97.1889	(3, 2)	992.316	157.932
(1, 3)	763.31	121.486	(2, 3)	992.316	157.932	(3, 3)	1374	218.675
(1, 4)	1297.6	206.526	(2, 4)	1526.6	242.972	(3, 4)	1908.3	303.715
(1, 5)	1984.6	315.864	(2, 5)	2213.6	352.31	(3, 5)	2595.3	413.053

Table 3. Variations of natural frequencies (Hz) of simply supported plate with modal parameter *(m, n)* ($a = 1$ m, $b = 1$ m, $E = 2.052 \times 10^{11}$ N/m^2; $\upsilon = 0.3$, $\rho = 7850$ kg/m^3).

Modal parameter (*m*, *n*)	ω	***f*(Hz)**	**Modal parameter (*m*, *n*)**	ω	***f*(Hz)**	**Modal parameter (*m*, *n*)**	ω	***f*(Hz)**
(1, 1)	248.079	39.483	(2, 1)	477.075	75.9288	(3, 1)	858.735	136.672
(1, 2)	553.407	88.0774	(2, 2)	782.403	124.523	(3, 2)	1164.1	185.266
(1, 3)	1011.4	160.969	(2, 3)	1240.4	197.415	(3, 3)	1622.1	258.158
(1, 4)	1622.1	258.158	(2, 4)	1851.1	294.604	(3, 4)	2232.7	355.347
(1, 5)	2385.4	379.644	(2, 5)	2614.4	416.089	(3, 5)	2996	476.833

Table 4. Variations of natural frequencies (Hz) of simply supported-clamped plate with modal parameter *(m, n)* ($a = 1$ m, $b = 1$ m, $E = 2.052 \times 10^{11}$ N/m^2; $\upsilon = 0.3$, $\rho = 7850$ kg/m^3).

Modal parameter (m, n)	ω	f(Hz)	Modal parameter (m, n)	ω	f(Hz)	Modal parameter (m, n)	ω	f(Hz)
(1, 1)	343.494	54.6687	(2, 1)	648.822	103.263	(3, 1)	1106.8	176.155
(1, 2)	648.822	103.263	(2, 2)	954.15	151.858	(3, 2)	1412.1	224.749
(1, 3)	1106.8	176.155	(2, 3)	1412.1	224.749	(3, 3)	1870.1	297.641
(1, 4)	1717.5	273.344	(2, 4)	2022.8	321.938	(3, 4)	2480.8	394.83
(1, 5)	2480.8	394.83	(2, 5)	2786.1	443.424	(3, 5)	3244.1	516.316

Table 5. Variations of natural frequencies (Hz) of clamped-clamped plate with modal parameter *(m, n)* (a = 1 m, b = 1 m, $E = 2.052 \times 10^{11}$ N/m^2; υ = 0.3, ρ = 7850 kg/m^3).

almost two times for m = 1 and m = 2 for CC-CC, SS-CC, and SS-SS boundary condition. **Figure 4** is drawn for the square plate when we take $a = b$ = 4 m and m = 3, 4, $n = 1 \sim 5$ with various boundary conditions and show the influence of these conditions. As the constraints in the end conditions are applied more, the frequencies increase. The frequency gapes for these boundary conditions at m, n = (1, 2), (2, 1) at $a = b$ = 3, 4 are very close to each other, and as we proceed the modal number, then the frequency gape is higher.

Figures 5 and **6** show the variation of natural frequencies (Hz) of rectangular plates versus the vibration modal wave number (m, n) for the boundary conditions on four edges viz., SS-SS, CC-CC, and SS-CC square plate. **Figure 5** is drawn for the rectangular plate when we take a = 3, b = 2 m. As the constraints in the end conditions are applied more, the frequencies increase. Here, we fix the value of m = 1 but vary the value of n from $1 \sim 5$. It is observed that frequency increases by increasing the value of n. It has been seen that the frequency is almost two times for m = 1 and m = 2 for SS-SS, SS-CC, and CC-CC boundary condition. The frequency curves are observed closed to each other for modal wave number, (m, n) = (1, 1), (1, 2), (2, 1), (2, 2).

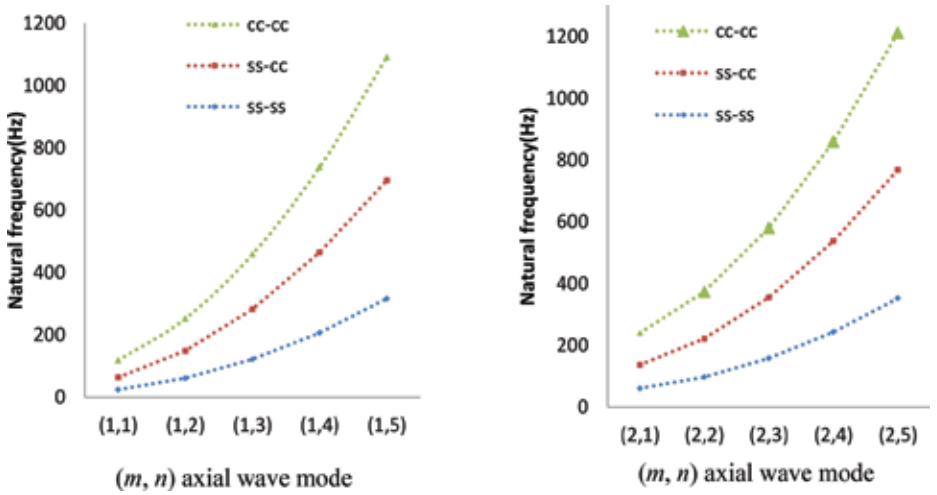

Figure 3. The influence of natural frequencies of a square plate for SS-SS, SS-CC, and CC-CC boundary conditions (a = 3 m, b = 3 m, $E = 2.052 \times 10^{11}$ N/m^2; υ = 0.3, ρ = 7850 kg/m^3).

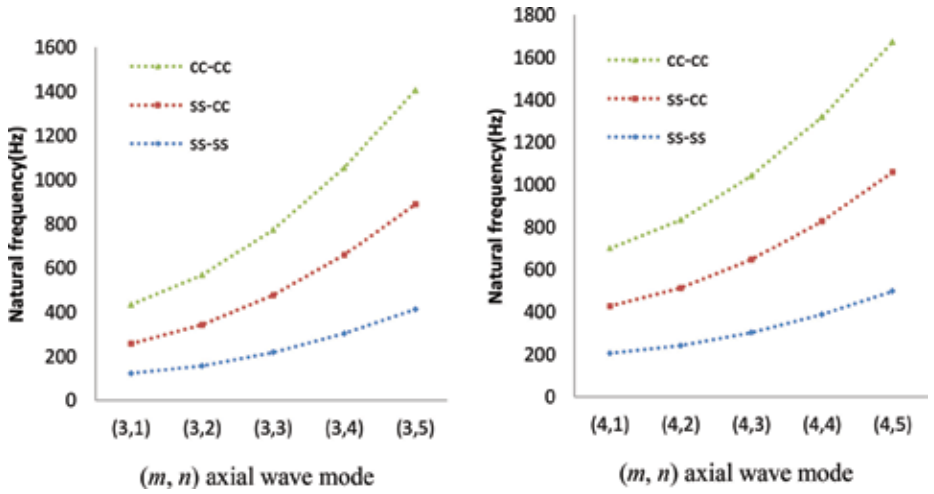

Figure 4. The influence of natural frequencies of a square plate for SS-SS, SS-CC, and CC-CC boundary conditions ($a = 4$ m, $b = 4$ m, $E = 2.052 \times 10^{11}$ N/m^2; $\upsilon = 0.3$, $\rho = 7850$ kg/m^3).

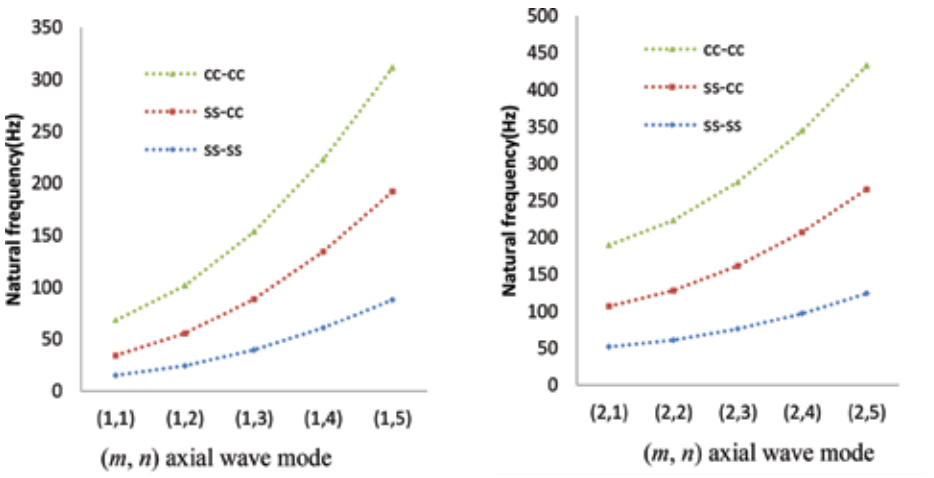

Figure 5. The influence of natural frequencies of a rectangular plate for SS-SS, SS-CC, and CC-CC boundary conditions ($a = 3$ m, $b = 2$ m, $E = 2.052 \times 10^{11}$ N/m^2; $\upsilon = 0.3$, $\rho = 7850$ kg/m^3).

Figure 6 is drawn for the rectangular plate when we take $a = 4$, $b = 3$ m. It can be perceived from above discussion that the CC-CC boundary conditions have the height frequency curves of rectangular plates and other boundary condition followed as SS-CC and SS-SS. It is also concluded that the frequency curves with SS-SS boundary condition are the lowest for varying the modal wave number. For these boundary conditions, on increasing the length a and width b, the frequencies also increase (m, n). In these figures, it can be seen that the gap between the CC-CC and SS-CC is greater than that of SS-SS boundary condition. **Figures 5** and **6** also show that the trend of frequency is same for the symmetry of (m, n).

http://dx.doi.org/10.5772/intechopen.80672

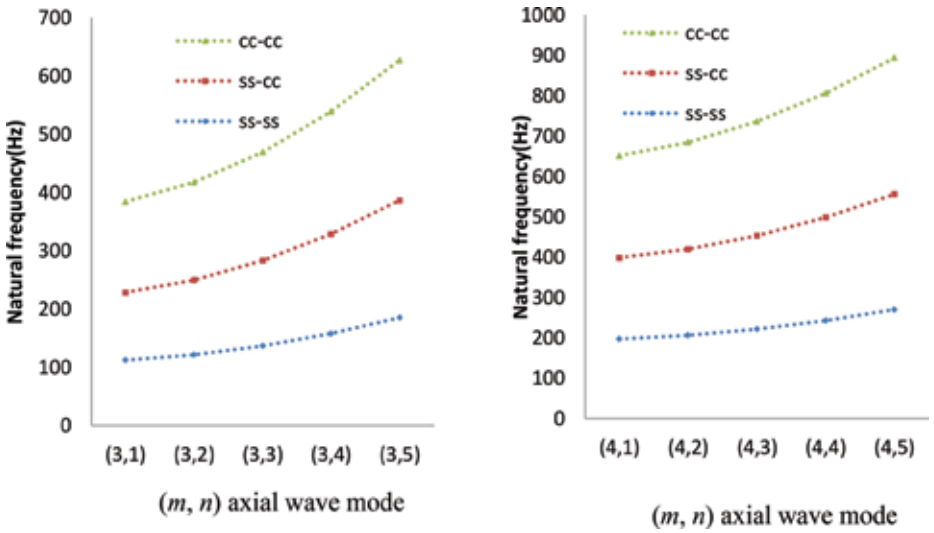

Figure 6. The influence of natural frequencies of a rectangular plate for SS-SS, SS-CC, and CC-CC boundary conditions ($a = 4$ m, $b = 3$ m, $E = 2.052 \times 10^{11}$ N/m^2; $\upsilon = 0.3$, $\rho = 7850$ kg/m^3).

4. Concluding remarks

In this study, vibrations of isotropic square and rectangular plates have been investigated for modal parameters. Wave propagation approach has been engaged to solve this problem. The axial deformations along axial variables are approximated by the complex exponential functions. The axial wave numbers are associated with particular boundary conditions. As the modal wave numbers are enhanced, the frequencies for the plates indefinitely. Moreover, the influence of the boundary conditions has been studied for by changing the axial wave modes. Dynamical loadings are exerted on plates when they are involved in a physical system. Their dynamical behavior is studied theoretically. In the present study, vibrations of square and rectangular plates are analyzed by applying the wave propagation approach. This is an approximate technique related to the axial wave modes obtained characteristic beam functions. These axial wave modes represent boundary conditions specified at four ends of a rectangular plate. Natural frequencies for vibrating square and rectangular plates are obtained for various boundary conditions. The natural frequencies of plates are investigated versus modal numbers by varying the length and width of the plates with simply supported- simply supported (SS-SS), clamped-clamped (CC-CC), and simply supported-clamped (SS-CC) boundary conditions. The frequencies of the plates increase by increasing the modal number, and CC-CC frequencies are greater than the frequencies of other boundary conditions. If we change the nature of material of plate or other physical parameters applied to maintain motion in radial direction, then a new problem can be formed. These problems can be solved for different set of boundary conditions. This analysis can be applied to examine the vibrations of functionally graded material plates.

Author details

Muzamal Hussain* and Muhammad Nawaz Naeem

*Address all correspondence to: muzamal45@gmail.com

Department of Mathematics, Govt. College University Faisalabad, Faisalabad, Pakistan

References

[1] Mindlin RD, Schecknow A, Dereshiewicz H. Flexural vibrations of rectangular plates. Journal of Applied Mechanics. 1956;**23**:430-436

[2] Leissa AW. Vibration of plates. NASASP. 1969;**160**:53

[3] Are EB, Idowu AS, Gbadeyan JA. Vibration of damped simply supported orthotropic rectangular plate s resting on elastic Winkler foundation, subjected to moving loads. Advances in Applied Science Research. 2013;**4**(5):387-393

[4] Ding Z, Tianjian J. Free vibration of rectangular plates with continuously distributed spring-mass. International Journal of Solids and Structures. 2006;**5**(1):455-460

[5] Ezeh JC, Njoku KO, Ibearugbulem OM, Ettu LO, Anyaogu L. Free vibration analysis of thin rectangular isotropic cc-cc plate using Taylor series formulated shape function in Galerkin's method. Academic Research International. 2006;**4**(4):126-132

[6] Ibearugbulem OM, Ezeh JC, Onyechere CI. Free vibration analysis of thin rectangular plates using ordinary finite difference method. Journal of Applied Mechanics. 2013;**4**(2): 1551-1557

[7] Jiu HW, Liu AQ, Chen HL. Exact solution for free vibration analysis of rectangular plates using Bessel functions. Journal of Applied Mechanics. 2007;**74**:1247-1251

[8] Onyechere CI, Ibearugbulem OM, Ezeh JC. Free vibration analysis of thin rectangular flat plates using ordinary finite difference method. Part-I: Natural and Applied Sciences. 2013; **4**(2):187-192

[9] Ramezani S, Ahmadian MT. Free vibration analysis of rotating laminated cylindrical shells under different boundary conditions using a combination of the layer-wise theory and wave propagation approach. Archive of Applied Mechanics. 2013;**83**:521-531

[10] Kerboua Y, Lakis AA, Marcouiller TL. Vibration analysis of rectangular plates coupled with fluid. Applied Mathematical Modelling. 2008;**32**(12):2570-2586

[11] Xing Y, Liu B. New exact solutions for free vibrations of rectangular thin plates by symplectic dual method. Acta Mechanica Sinica. 2009;**25**:265-270

[12] Zhou D, Ji T. Free vibration of rectangular plates with continuously distributed spring-mass. International Journal of Solids and Structures. 2006;**43**(21):6502-6520

[13] Sakiyama T, Huang M. Free vibration analysis of rectangular plates with variable thickness. Reports of the Faculty of Engineering, Nagasaki University Japan; 1998

[14] Ventsel E, Krauthammer T. Thin plates and shells: theory, analysis and applications. New York, USA: Marcel Dekker, Inc; 2001

[15] Zhang XM, Liu GR, Lam KY. Coupled vibration analysis of fluid-filled cylindrical shells using the wave propagation approach. Applied Acoustics. 2001;**62**:229-243

[16] Werfalli NM, Karoud AA. Free vibration analysis of rectangular plates using Galerkin-based finite element method. International Journal of Mechanical Engineering. 2005;**2**(2):59-67

[17] Hsu M. Vibration characteristics of rectangular plates resting on elastic foundations and carrying any number of sprung masses. International Journal of Applied Sciences and Engineering. 2006;**4**(1):83-89

[18] Mansour NB, Masih L, Pooyanfar M. Analytical solution for free vibration of rectangular Kirchhoff plate from wave approach. World Academy of Science. Engineering and Technology. 2008;**39**:221-223

[19] Lal R, Kumar Y, Gupta US. Transverse vibrations of nonhomogeneous rectangular plates of uniform thickness using boundary characteristic orthogonal polynomials. International Journal of Applied Mathematics and Mechanics. 2010;**6**(14):93-109

[20] Sun S, Cao D, Chu S. Free vibration analysis of thin rotating cylindrical shells using wave propagation approach. Archive of Applied Mechanics. 2012;**83**:521-531

[21] Njoku K, O Ezeh JC, Ibearugbulem OM, Ettu LO, Anyaogu L. Free vibration analysis of thin rectangular isotropic CC-CC plate using Taylor series formulated shape function in Galerkin's method. Part I: Natural and Applied Sciences. 2013;**4**(4):126-132

[22] Ducceschi M. Nonlinear vibrations of thin rectangular plates: A numerical investigation with application to wave turbulence and sound synthesis [Doctoral dissertation]. ENSTA Paris Tech; 2014

[23] Park I, Lee U, Park D. Transverse vibration of the thin plates: frequency-domain spectral element modeling and analysis. Mathematical Problems in Engineering. 2015

[24] Kalita K, Haldar S. Free vibration analysis of rectangular plates with central cutout. Cogent Engineering. 2016;**3**(1):1163781

[25] Korabathina R, Koppanati MS. 19. Linear free vibration analysis of rectangular Mindlin plates using coupled displacement field method. Journal of Mathematical Models in Engineering (MME). 2016;**2**(1):41-48

[26] Merneedi A, Nalluri M, Rao VS. Free vibration analysis of a thin rectangular plate with multiple circular and rectangular cut-outs. Journal of Mechanical Science and Technology. 2017;**31**(11):5185-5202

[27] Hussain M, Naeem MN, Shahzad A, He M. Vibration characteristics of fluid-filled functionally graded cylindrical material with ring supports. In: Computational Fluid Dynamics. Intechopen; 2018, ISBN 978-953-51-5706-9. DOI: 10.5772/intechopen.72172

[28] Hussain M, Naeem MN, Isvandzibaei MR. Effect of Winkler and Pasternak elastic foundation on the vibration of rotating functionally graded material cylindrical shell. Proceedings of the Institution of Mechanical Engineers, Part C: Journal of Mechanical Engineering Science. 2018. DOI: 10.1177/0954406217753459

[29] Yang TY. Finite Element Structural Analysis. Upper Saddle River, NJ, USA: Prentice Hall; 1986

[30] Hussain M, Naeem MN, Shahzad A, He M. Vibrational behavior of single-walled carbon nanotubes based on cylindrical shell model using wave propagation approach. AIP Advances. 2017;**7**(4):045114

[31] Hussain M, Naeem MN. Vibration analysis of single-walled carbon nanotubes using wave propagation approach. Mechanical Sciences. 2017;**8**(1):155-164

[32] Hussain M, Naeem MN. Vibration of single-walled carbon nanotubes based on Donnell shell theory using wave propagation approach. In: Novel Nanomaterials: Synthesis and Applications. Rijeka, Croatia: IntechOpen; 2018, ISBN 978-953-51-5896-7. DOI: 10.5772/intechopen.73503

[33] Sodel W. Vibration of shell and plates. Mechanical Engineering series. New York: Marcel Dekker; 1981

Chapter 4

Advanced Space Flight Mechanical Qualification Test of a 3D-Printed Satellite Structure Produced in Polyetherimide ULTEM™

Jonathan Becedas, Andrés Caparrós,
Antonio Ramírez, Pablo Morillo,
Esther Sarachaga and Almudena Martín-Moreno

Additional information is available at the end of the chapter

http://dx.doi.org/10.5772/intechopen.79852

Abstract

The aim of this work is to demonstrate the use of additive manufacturing with thermoplastic material in the whole functional structure of spacecraft and to mechanically qualify it for space flight. For such purpose, an 8 U CubeSat structure was manufactured in polyetherimide (PEI) ULTEM™ through 3D printing and passed several vibration tests. The results are compared with those obtained in the qualification of the same structure manufactured in aluminum alloy AA-6082 T651 through a conventional CNC method. The qualification consisted of passing the vibration requirements in quasi-static, sine, and random tests to fly in PSLV launcher. Finally, a robustness test for the 3D-printed structure is included, and all the results are analyzed. This study is being part of the H2020 European Project ReDSHIFT (Project ID 687500).

Keywords: polyetherimide, ULTEM™, vibration, space qualification, additive manufacturing, 3D printing, fused deposition modeling, satellite structure

1. Introduction

The cost of putting a satellite into orbit is directly related to its mass. Putting 1 kg into a low Earth orbit can be between $10.000 and $20.000 for medium- to large-sized satellites [1, 2] and between $40.000 and $50.000 for small satellites (under 100 kg) [3]. In small satellites one of the subsystems that most contribute to the total mass of the system is the structural subsystem. Normally, the structure of the satellite contributes between 30 and 40% to the total mass of the

spacecraft. However, this is normal because these structures are commonly made of metallic materials such as aluminum alloys [4], because they need to resist very demanding environmental conditions in space and very demanding mechanical conditions during the launch, and because they have to guarantee the integrity of the satellite itself and of the other satellites placed in the launcher.

However, additive manufacturing is enabling the use of new materials for space such as polyetherimide (PEI) [5]. Polyetherimide (PEI) is an amorphous thermoplastic very resistant to high and low temperatures, with a high glass transition temperature, and very resistant to mechanical loads [6] and has half the density of the aluminum. The incorporation of this type of materials in the structure of satellites can highly reduce the mass of the overall system and the cost of putting it into space.

Nevertheless, the incorporation of new materials and methods in a spacecraft requires a profound analysis and passing of very demanding tests to prove that it is qualified to be launched and to be performed with enough margin in the space environment [7]. During the launch, the structure will suffer extreme mechanical stress. The conditions are a combination of static and dynamic loads or mechanical aggressions [8] constituted by the static loads and acceleration, the pressure produced by the mechanical waves generated by the noise inside the launcher, and the vibrations produced by its motor and its structure, by all the other satellites onboard, and by the shocks when every stage of the launcher is separated or when the satellite is separated from the launcher. These effects are combined as a random vibration in which shocks can be superimposed.

In order to verify that a satellite can resist the launch, the launcher authorities provide a set of requirements that have to be fulfilled and verified through mechanical testing. These are modal survey vibration tests to identify the modes of vibration of the satellite to demonstrate that the main modes have higher frequencies than the launcher and that it will not enter in resonance, quasi-static vibration tests to demonstrate that the satellite resists the accelerations of the launcher, sine vibration tests to demonstrate that the satellite resists all the vibrations induced by the launcher, random vibration test to demonstrate that the satellite resists an emulated launch in which all the loads are combined, and shock vibration test to demonstrate that the satellite resists the shocks during the launch.

In this work, a small satellite structure 8 U CubeSat type 3D-printed in PEI ULTEM™ 9085 is presented. The structure was mechanically tested at qualification levels to fly in the Polar Satellite Launch Vehicle (PSLV) [9], and the results are presented compared with the results of the same structure manufactured in aluminum alloy AA-6082 T651 through a conventional CNC method. Once the structure in ULTEM™ was qualified, a robustness test was done to identify its mechanical limits. All the results are included in Section 3 and discussed in Section 4.

2. Materials and methods

The qualification of a new structural design for a spacecraft requires a very methodic procedure in which all the boundary conditions shall be considered and controlled with care:

http://dx.doi.org/10.5772/intechopen.79852

manufacturing environment and methodology, transport of the parts and their inspection, assembly, testing, and analysis. The whole process shall be completely controlled and monitored. In this section, the experiment is described, the methodology applied in the whole process is introduced, the test specimens are detailed, and the instrumentation and equipment used during the testing are specified.

2.1. Experiment description

The objective of this experiment is to validate the use of additive manufacturing technology with PEI to be implemented in functional structures of satellites. For this purpose, a novel structure with 3D-printed PEI ULTEM™ 9085 was manufactured and tested, and it was compared with the same structure manufactured in aluminum alloy AA-6082 T651 with classical CNC milling methodology. The two test specimens are described in Section 2.1.1.

To qualify the structure of the spacecraft, a structural model was assembled as part of the model philosophy established [10]. The structural model was constituted by the structural subsystem of the satellite (functional structure) and by mass dummies, which were mechanically equivalent to the real components of the satellite.

2.1.1. Test specimen description

The test specimens used in the test campaign were two CubeSat structures manufactured by using different materials and technologies:

- Aluminum alloy AA-6082 T651, density 2.70 g/cm^3, manufactured by CNC milling
- PEI ULTEM™ 9085, density 1.34 g/cm^3, manufactured by fused deposition modeling (FDM)

The structural subsystem of the 8 U CubeSat consisted of six panels (cube faces), a T bracket, and a central avionics tray providing mechanical interface for all the equipment onboard the satellite. To validate the 3D-printed structure in ULTEM™, no particular design optimization was performed with regard to the structure in aluminum; in other words, the same set of manufacturing drawings and CAD models was used to manufacture the model in the machining workshop and in the additive manufacturing facility.

The design baseline was a medium-resolution Earth observation (EO) mission with the following commercial components constituting the satellite: an Astro Digital Data and Power Module (DPM), three Sinclair reaction wheels (RWs), a Sensonor gyrometer (GYR), two BST Star Trackers (STs), a Syrlinks X-Band Transmitter Unit (XTU), a VACCO Propulsion System (PS), an ANTCOM GPS antenna (GPS), an SCS Space Gecko imager payload (IMG), an EnduroSat X-Band antenna, and an Astro Digital UHF antenna.

The internal distribution of the components in the internal volume of the 8 U structure was done by considering the center of gravity (CoG) requirements imposed by the launcher [11].

For the design of the structural models, the complete avionics suite was substituted by mass dummies or mock-up representative of their functional counterparts not only in terms of envelope and mounting interfaces (bolts) but also in mass and center of gravity (CoG). All replicas

were manufactured in aluminum and anodized to be preserved from corrosion. The total mass of mock-ups was 5.2 kg, considering a realistic configuration for an 8 U CubeSat. The structure in aluminum had a mass of 3.1 kg (37.35% of the total mass, which was 8.3 kg), and the structure in ULTEM™ had a mass of 1.45 kg (46.77% less mass than the aluminum structure and 21.80% of the total mass of the structural model, which was 6.65 kg). **Table 1** shows the list of mock-ups with the most relevant mechanical properties: dimensions, mass, and coordinates of the center of gravity with respect to the geometric center of the satellite structure.

The overall structure design adheres to the CubeSat standard [12], and it could be fitted in any commercial P-POD designed to host an 8 U satellite. **Figure 1** shows the parts of the structure made with additive manufacturing in PEI ULTEM™. **Figure 2** depicts the mock-ups assembled in the structure.

Figure 3 shows the two test specimens populated with the mock-up avionics. The single circular window (front pictures) provided field of view for the payload camera. The two orthogonal circular windows (back pictures) provided fields of view for the star trackers. The purpose of the overtures in the structure was to reduce the mass of the structure while providing access to manipulate inside the spacecraft during assembly activities.

2.1.2. Testing platform description

The testing platform was represented by an electrodynamic shaker model LDS B&K V850–440 with an LDS B&K LPT 600 slip table with a mechanical interface adapter mounted on it (see **Figure 4**). The electrodynamic shaker stood over a concrete block by means of four silent blocks. The shaker was controlled by an LDS-Dactron control system, and the signal was amplified with an LDS B&K SPA 32Kv3 Kk4a-CE amplifier of 22 kN. Three accelerometers

Tag	Equipment name	Mock-up dimensions (mm)	Mock-up mass (gr)	X CoG (mm)	Y CoG (mm)	Z CoG (mm)
DPM	Data and Power Module	100(W) × 199(L) × 87(H)	1796	64.9	−3.6	−55.0
IMG	Imager payload	97(W) × 96(W) × 60(H)	473	2.1	58.5	−53.9
GPS	GPS antenna	40(W) × 40(L) × 26(H)	41	−64.1	−7.3	−23.8
ST1	Star tracker No. 1	30(W) × 30(L) × 38(H)	233	0.9	−74.5	−23.8
ST2	Star tracker No. 2	30(W) × 30(L) × 38(H)	233	−57.0	−71.0	−17.6
RW1	Reaction wheel No. 1	50(W) × 50(L) × 40(H)	171	108.5	105.5	−113.1
RW2	Reaction wheel No. 2	50(W) × 50(L) × 40(H)	171	84.7	35.2	41.7
RW3	Reaction wheel No. 3	50(W) × 50(L) × 40(H)	171	−64.5	61.1	−43.6
GYR	Gyroscope	39(W) × 45(L) × 22(H)	51	40.9	41.6	−53.9
PRO	Propulsion	39(W) × 45(L) × 80(H)	1181	0.0	0.0	101.7
XTU	X-Band transmitter	90 (W) × 96(L) × 24 (H)	433	0.0	0.0	−101.7

Table 1. List of mock-ups with mechanical properties.

http://dx.doi.org/10.5772/intechopen.79852

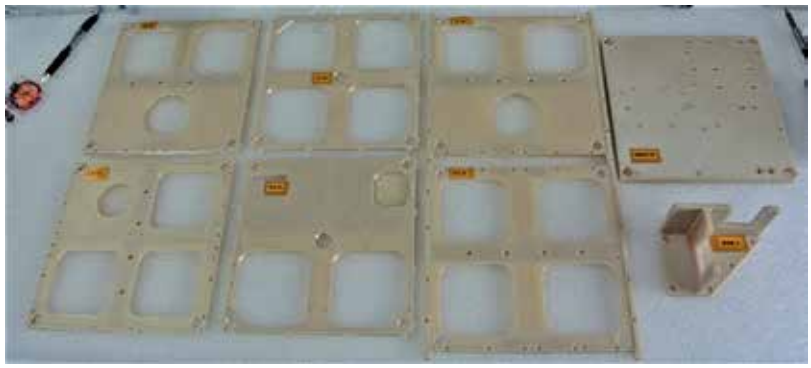

Figure 1. Structure of the 3D-printed satellite in PEI.

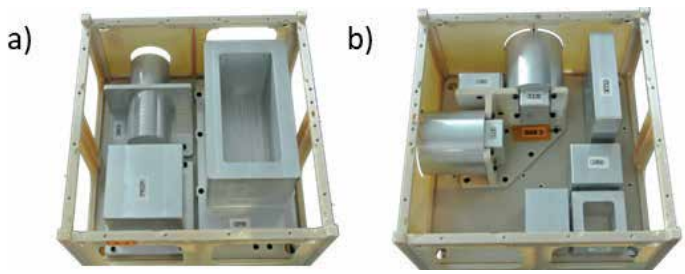

Figure 2. Mock-ups assembled in the 3D-printed structure. (a) Top view and (b) bottom view.

were used to record the measurements, one monoaxial 4513-B type used as control and two triaxial 4520-001 type for recording the response of the structural models.

2.1.3. Test specifications

The structural model was tested at qualification levels established by PSLV [11]. The applied loads to qualify the structure were the following:

- Modal survey: to identify the modes of the structural model, a modal survey was done. The parameters were the following: maximum test frequency (2 kHz) and sweep-type logarithmic and sweep rate (2.0 oct/min). This was done in every axis: X, Y, and Z.
- Quasi-static load (QSL): it was characterized by a ramp up which increases amplitude levels from 0.1 to 8.75 g of acceleration between 5 and 20 Hz, acceleration amplitude of 8.75 g at 20 Hz, and a ramp down from the maximum amplitude of 8.75 to 0.1 g at frequencies from 20 to 5 Hz. The load profile is shown in **Figure 5**. This test was done in every axis: X, Y, and Z.
- Sine load: with maximum acceleration amplitude of 2.5 g at frequencies from 10 to 100 Hz. The load profile is shown in **Figure 6**. This test was done in every axis: X, Y, and Z.

- Random load: it was defined by a specific power spectral density (PSD) profile in function of the frequency. The profile is defined in **Figure 7**. This test was done in every axis: X, Y, and Z.
- Shock load: it was modeled as a variable acceleration profile with levels between 8 and 220 g for frequencies between 20 and 2000 Hz, as shown in **Figure 8**. This test was done in axis Z. The profile from 30 to 300 Hz was representative of the qualification level; for higher frequencies, the test could not be done for limitations of the testing platform used. However, this test specification was representative enough.

The tests were done by following the standards [7, 10].

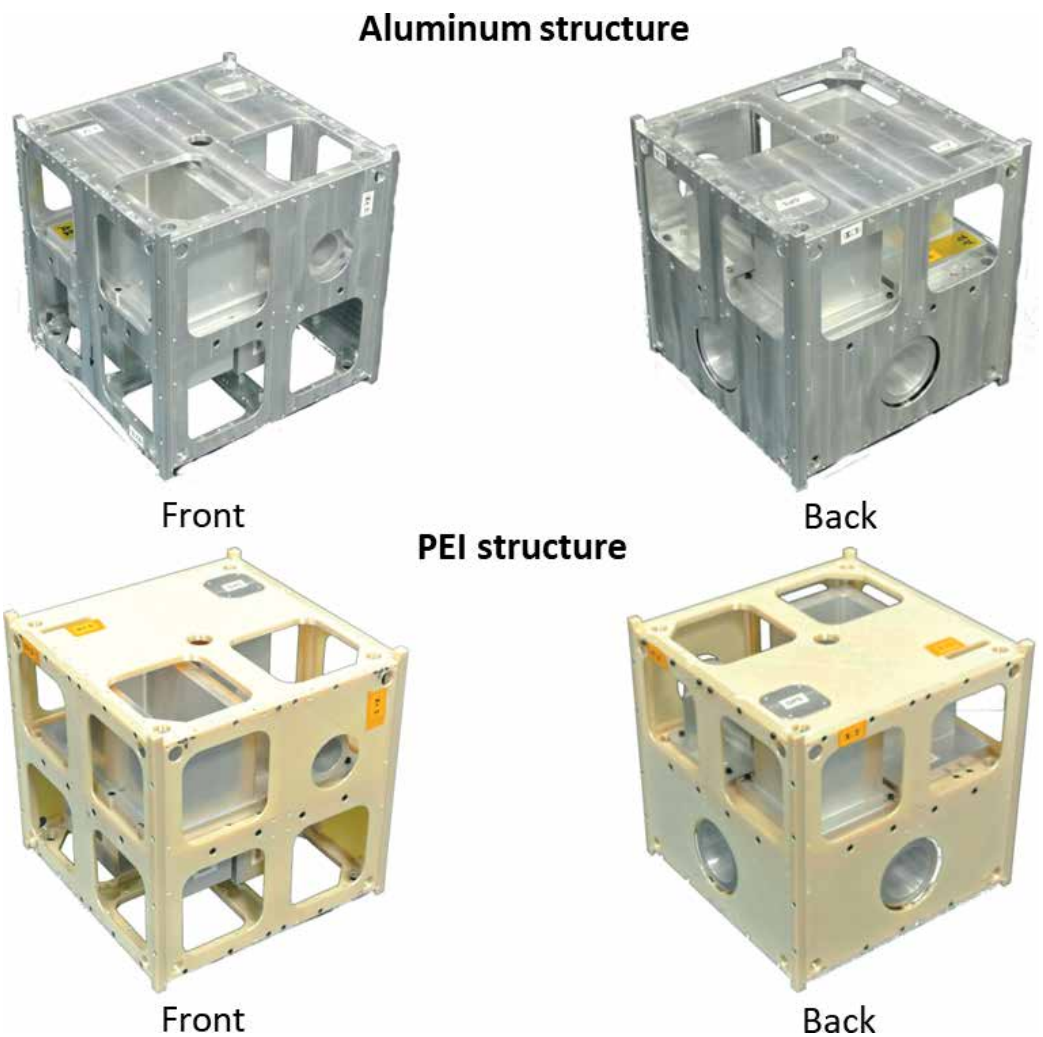

Figure 3. ReDSHIFT structural models.

http://dx.doi.org/10.5772/intechopen.79852

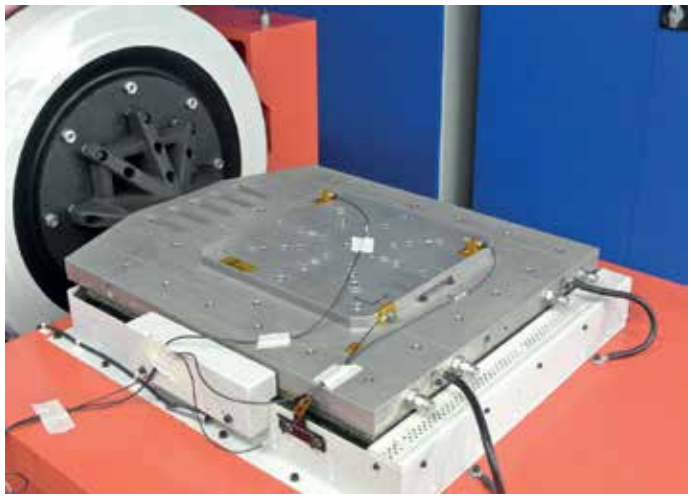

Figure 4. Interface adapter mounted on the shaker slip table.

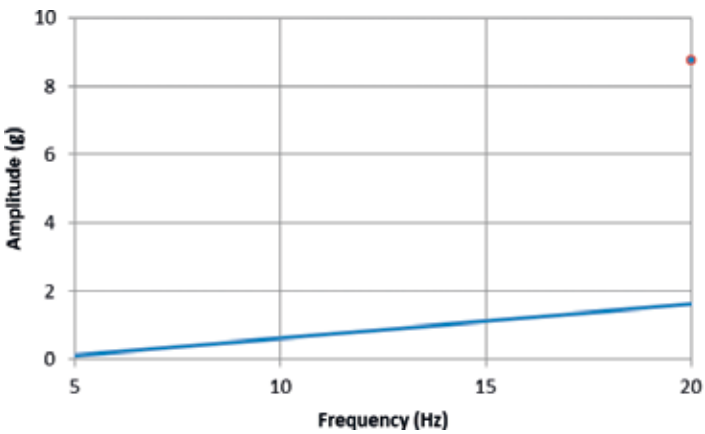

QSL (Qualification)	
Frequency	Amplitude
5	0.1
20	1.61
20	8.75

Figure 5. QSL profile.

As the purpose of the test was to qualify the 3D-printed structure and to analyze the differences between the 3D-printed ULTEM™ structure and the CNC-milled aluminum structure, the tests were performed on the bare structural models, i.e., not preserving the models inside a P-POD. For such a purpose, the bottom panels of the structures incorporated, near the corners, four M12 holes that were used to secure the test specimen on top of the mechanical interface with the slip table. In a real launch scenario, this would imply the adoption of pyro-bolts to assemble the spacecraft to the launcher interface. This was the worst case scenario for qualification purposes of the structure.

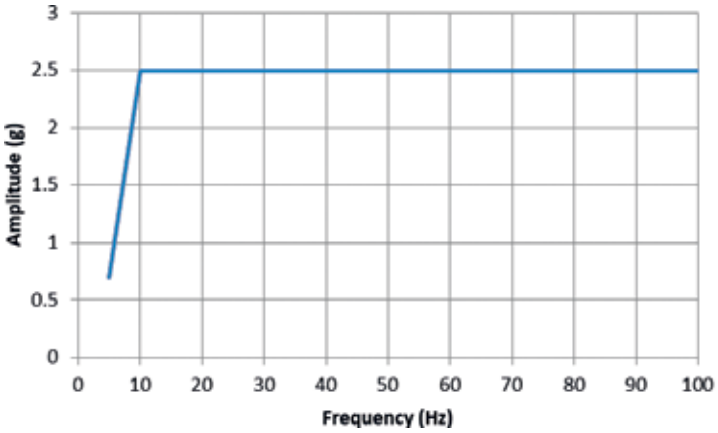

Sine Load (Qualification)	
Frecuency	Amplitude
5	0.7
10	2.5
100	2.5

Figure 6. Sine load profile.

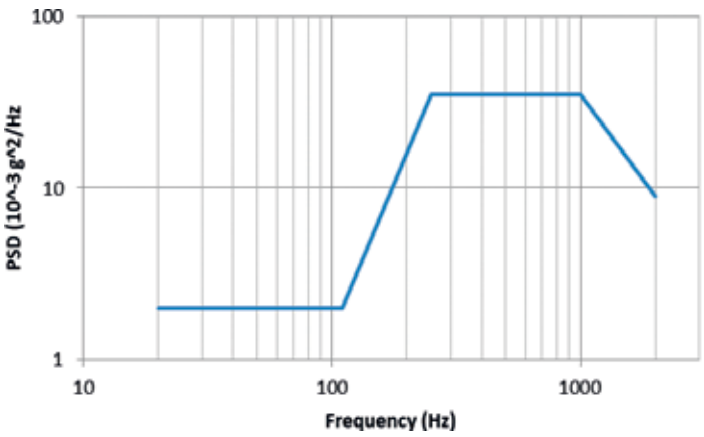

Random Load (Qualification)	
Frequency	PSD
20	2
110	2
250	35
1000	35
2000	9

Figure 7. Random load profile.

2.1.4. Experimentation methodology

To guarantee a representative experimentation for the qualification of the structural model in ULTEM™, a specific and very controlled process was carried out. It started with the selection of competitive providers to manufacture the parts. Once they were received, a careful incoming goods reception was done in order to validate that all the parts fulfilled the specifications defined. This process consisted of inspecting from the parcel to its content, taking into account physical status and functionality. A report (incoming inspection report) was done in order to register every detail related to packaging, labeling, wrapping, isolation, external damages, and internal damages. Serial and part numbers were checked. Photos were also taken so that every aspect could be graphically supported. After the approval of the incoming inspection, the structural model was assembled to validate the design and manufacturing processes. Once the assembly was successful, the structures were dismounted and protected, side panel by side

http://dx.doi.org/10.5772/intechopen.79852

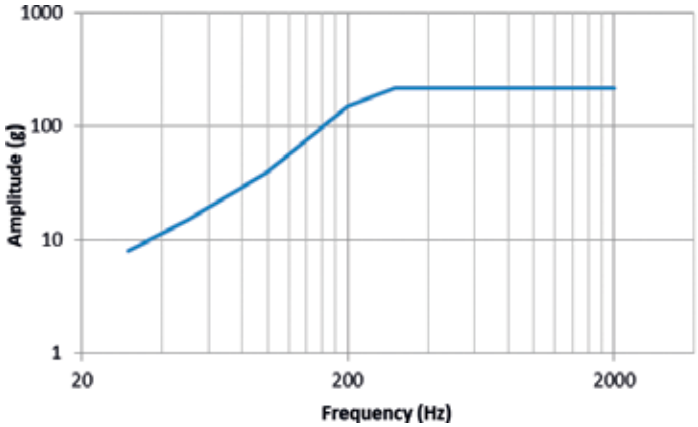

Shock Load (Qualification)	
Frequency	Amplitude
30	8
50	15
100	40
200	150
300	220
370	220
2000	220

Figure 8. Shock load profile.

panel, with bubble wrap, and they were packaged using shock-absorbing material. The same process was carried out to package the mock-ups.

Then, the packaged parts and required tools were prepared to be sent to the test facilities. Transport documents (packing list and annexes) were prepared. These documents contained information such as shipper, addressee, item description, references, gross weight, net weight, dimensions, and Incoterms. Incoterm is reflected the International Commercial Terms, i.e., it specified who took what risk and where.

When the goods arrived at the test facilities, the incoming goods reception process started again, and a new incoming inspection report was carried out. Transport documents were also checked.

Once the incoming inspection report was favorable, the structural model was assembled and mounted on the interface adapter with the slip table of the shaker.

To carry the experiment out, the Z panel of the specimen was fixed on the interface adapter by means of four M12 screws; subsequently, the rest of the assembled structure was fit on the Z panel and fixed by means of 24 M2.5 screws. For X and Y axes, the test was performed on the slip table (horizontal configuration) just rotating the test specimen 90°. For the Z-axis experimentation, the electrodynamic shaker was rotated 90° to the vertical configuration (**Figure 9**).

The following testing procedures were followed:

1. Survey vibration test in the direction of the selected axis of the test specimen to detect the vibration modes
2. Sine vibration test in the selected axis of the test specimen at qualification level
3. Survey vibration test in the selected axis of the test specimen to detect if there were significant changes in the modes

4. QSL vibration test in the selected axis of the test specimen at qualification level
5. Survey vibration test in the selected axis of the test specimen to detect if there were significant changes in the modes
6. Random vibration test in the selected axis of the test specimen at qualification level
7. Survey vibration test in the selected axis of the test specimen to detect if there were significant changes in the modes
8. Shock vibration test only in the selected axis of the test specimen
9. Survey vibration test after the shock vibration test in the Z-axis of the test specimen to detect if there were significant changes in the modes

A significant change was defined as a change in frequency of the modes of at least 10%. Firstly, the CNC aluminum model was tested on the X-axis and then on the Y-axis. Secondly, the 3D-printed ULTEM™ model was tested on the X-axis and then on the Y-axis. Thirdly, the electro-dynamic shaker was turned 90° to test on the Z-axis of the CNC aluminum model first, and then on the ULTEM™ model.

When the experiment was finished, the structures were dismounted and protected, side panel by side panel, with bubble wrap, and they were packaged using shock-absorbing material. The same process was carried out to package the mock-ups. The same logistics and inspection processes explained before were followed to transport the parts back.

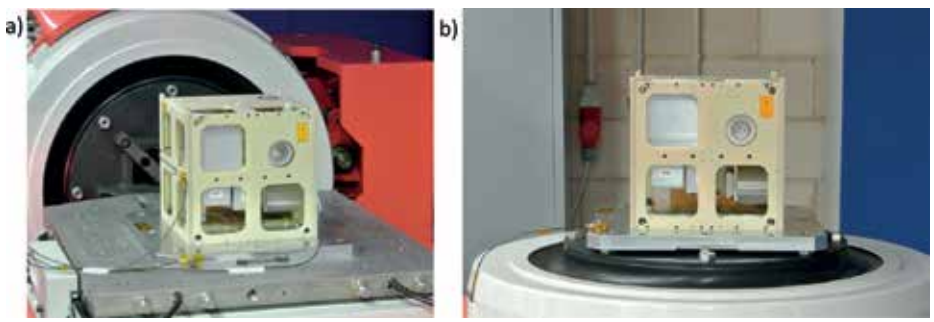

Figure 9. 3D-printed structural model mounted in the testing platform. (a) X-axis test and (b) Z-axis test.

3. Results

3.1. X-axis test results of the 3D-printed ULTEM™ structure

Figure 10 shows the results for the test carried out in the X-axis of the 3D-printed ULTEM™ structural model: modal survey (**Figure 10(a)**), QSL (**Figure 10(b)**), sine (**Figure 10(c)**), and random vibration (**Figure 10(d)**) tests. All the unities were expressed in g (9.81 m/s^2) except in the random test, which was expressed in PSD (power spectral density (g^2/Hz)). The red color

http://dx.doi.org/10.5772/intechopen.79852

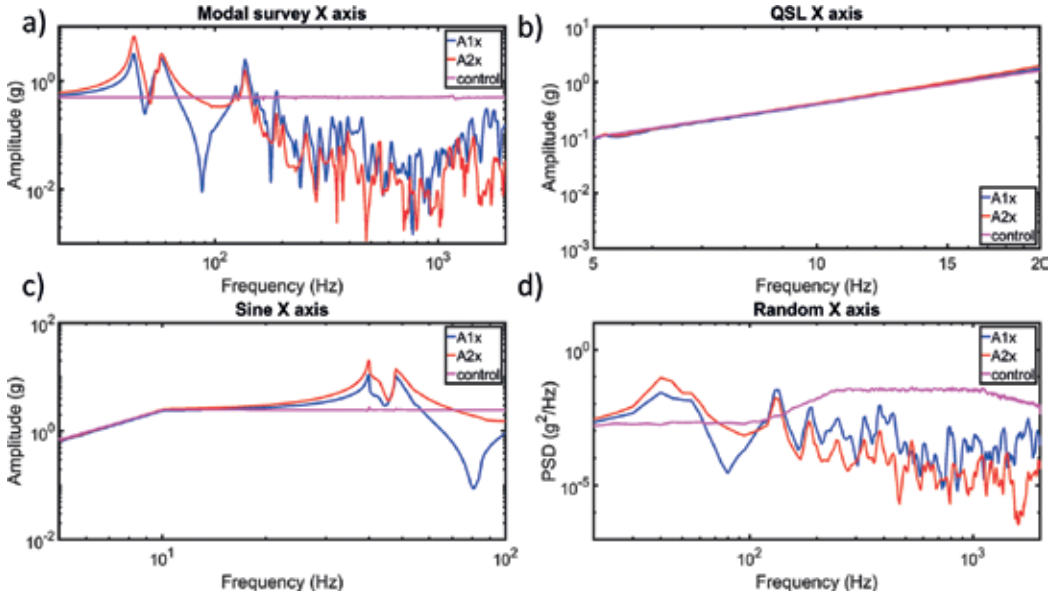

Figure 10. Results of the tests in the X-axis. (a) Modal survey, (b) QSL, (c) sine vibration, and (d) random vibration.

line represents the signal of the accelerometer 1 in the longitudinal axis, the blue color line represents the accelerometer 2 in the longitudinal axis, and the magenta line represents the control signal. **Table 2** summarizes the results obtained with the modal survey tests before and after the QSL, sine, and random tests were done. All the values are provided with the measurements of accelerometer 1 since the values provided by accelerometer 2 did not differ significantly.

With the modal survey, all the modes were characterized. The first mode was the most representative. This was located at 43.19 Hz. The amplitude of the first mode was 3.22 g. For comparison, the main mode of the structure manufactured by CNC in aluminum had a frequency of 190.77 Hz and had an amplitude of 8.2 g. This shows that the 3D-printed structure has less rigidity, but it still fulfills the requirement provided by the PSLV launcher authority, which established that the first mode of the spacecraft shall be higher than 20 Hz.

3D-printed ULTEM™ structural model—modal survey results before and after the quasi-static load, sine, and random vibration tests in the X-axis

	Pre-QSL	Post-QSL	Pre-sine	Post-sine	Pre-random	Post-random
First modal freq. [Hz]	43.19	43.19	43.19	40.55	40.55	40.55
Observed deviation	<0.1%		−6.10%		<0.1%	
Accel. peak [g]	3.22	3.33	3.33	2.74	2.74	2.71
Observed deviation	3.40%		−6.10%		−1.8%	

Table 2. Results of the modal survey tests before and after the QSL, sine, and random vibration tests in the X-axis.

The QSL test indicated that the structure behaved perfectly. There was neither representative excitation nor attenuation in the structure. It perfectly followed the control signal without passing the limit values established by the control. After this test was finished, the modal survey showed that there was no significant deviation of the modes. The amplitude of the first mode was increased to 3.33 g (3.40% more).

The sine vibration test showed that the structural model entered in resonance at the frequencies of the first and the second modes. After this test, the first mode slightly changed the frequency to 40.55 Hz and reduced the amplitude to 2.74 g (6.10% less). This represented no major changes in the structure.

In the random vibration test, all the modes were excited. After the test, the frequency of the first mode did not change (40.55 Hz). Its amplitude was slightly reduced to 2.71 g (1.8% less).

There were no shifts over 10% in the frequency of the first mode before and after all the specific tests. In addition, after all the tests, the structure was analyzed, and no visible changes were identified (plastic deformation, broken screws, lost screws, and unassembled parts, among others), which means that all the tests were successfully passed.

3.2. Y-axis test results of the 3D-printed ULTEM™ structure

Figure 11 shows the results for the test carried out in the Y-axis of the 3D-printed ULTEM™ structural model: modal survey (**Figure 11(a)**), QSL (**Figure 11(b)**), sine (**Figure 11(c)**), and random vibration (**Figure 11(d)**) tests. The red color line represents the signal of the accelerometer 1 in the longitudinal axis, the blue color line represents the accelerometer 2 in the longitudinal axis, and the magenta line represents the control signal. **Table 3** summarizes the

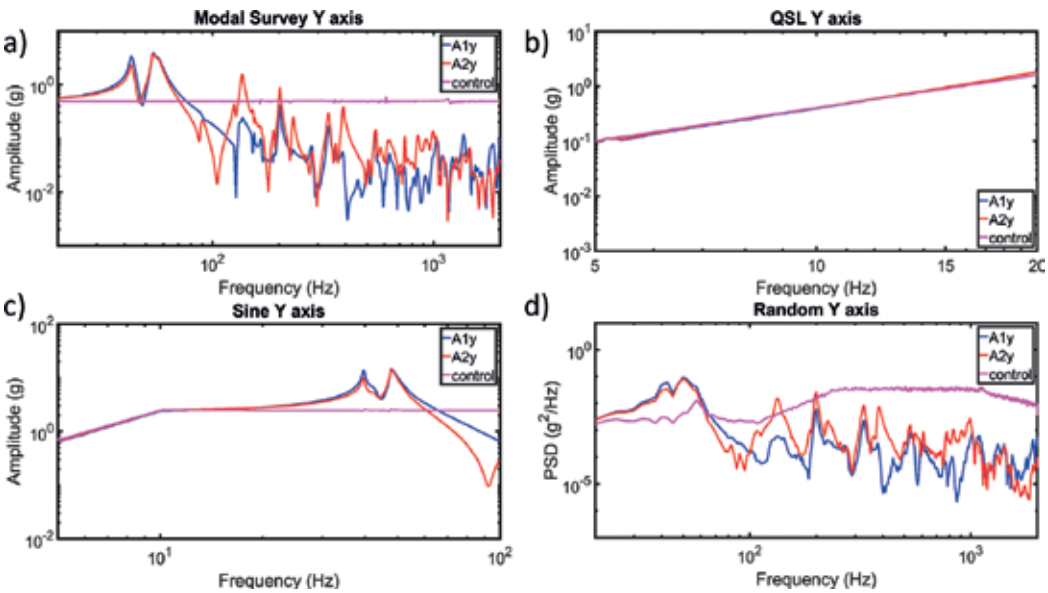

Figure 11. Results of the tests in the Y-axis. (a) Modal survey, (b) QSL, (c) sine vibration, and (d) random vibration.

3D-printed ULTEM™ structural model—modal survey results before and after the quasi-static load, sine, and random vibration tests in the Y-axis

	Pre-QSL	Post-QSL	Pre-sine	Post-sine	Pre-random	Post-random
First modal freq. [Hz]	43.19	43.19	43.19	41.66	41.66	41.66
Observed deviation	<0.1%		−3.70%		<0.1%	
Accel. peak [g]	3.44	3.54	3.54	3.18	3.18	3.08
Observed deviation	2.90%		−10.20%		−3.10%	

Table 3. Results of the modal surveys tests before and after the QSL, sine, and random vibration tests in the Y-axis.

results obtained with the modal survey tests before and after the QSL, sine, and random tests were done. As in the tests done in the X-axis, all the values are provided with the measurements of accelerometer 1 since the values provided by accelerometer 2 did not differ significantly.

With the modal survey, all the modes were characterized. The first mode was located at 43.19 Hz. The amplitude of the first mode was 3.44 g. For comparison, the main mode of the structure manufactured by CNC in aluminum had a frequency of 190.63 Hz and had an amplitude of 5.88 g.

Again, in the QSL test, the structure behaved perfectly between the margins defined by the control. The modal survey after this test showed that there was no significant deviation of the modes. The amplitude of the first mode was slightly increased to 3.54 g.

The sine vibration test showed that the structural model entered in resonance at the frequencies of the first and the second modes. After this test, the first mode slightly changed the frequency to 41.66 Hz and reduced the amplitude to 3.18 g (at 10.20% less, which indicates that the components of the structure would be less accelerated because the structure gained damping). This represented no major changes in the structure but an increase in the damping.

In the random vibration test, all the modes were excited. However, the first mode did not change in frequency, and the amplitude was reduced at 3.10% to 3.08 g.

There were no shifts over 10% in the frequency of the first mode before and after all the specific tests. In addition, after all the tests in the Y-axis, the structure was analyzed, and no visible changes were identified, which means that all the tests were successfully passed.

3.3. Z-axis test results of the 3D-printed ULTEM™ structure

Figure 12 shows the results for the test carried out in the Z-axis of the 3D-printed ULTEM™ structural model: modal survey (**Figure 12(a)**), QSL (**Figure 12(b)**), sine (**Figure 12(c)**), random vibration (**Figure 12(d)**), and shock (**Figure 12(e)**) tests. The red color line represents the signal of the accelerometer 1 in the longitudinal axis, the blue color line represents the accelerometer 2 in the longitudinal axis, and the magenta line represents the control signal. **Table 4** summarizes the results obtained with the modal survey tests before and after the QSL, sine, random,

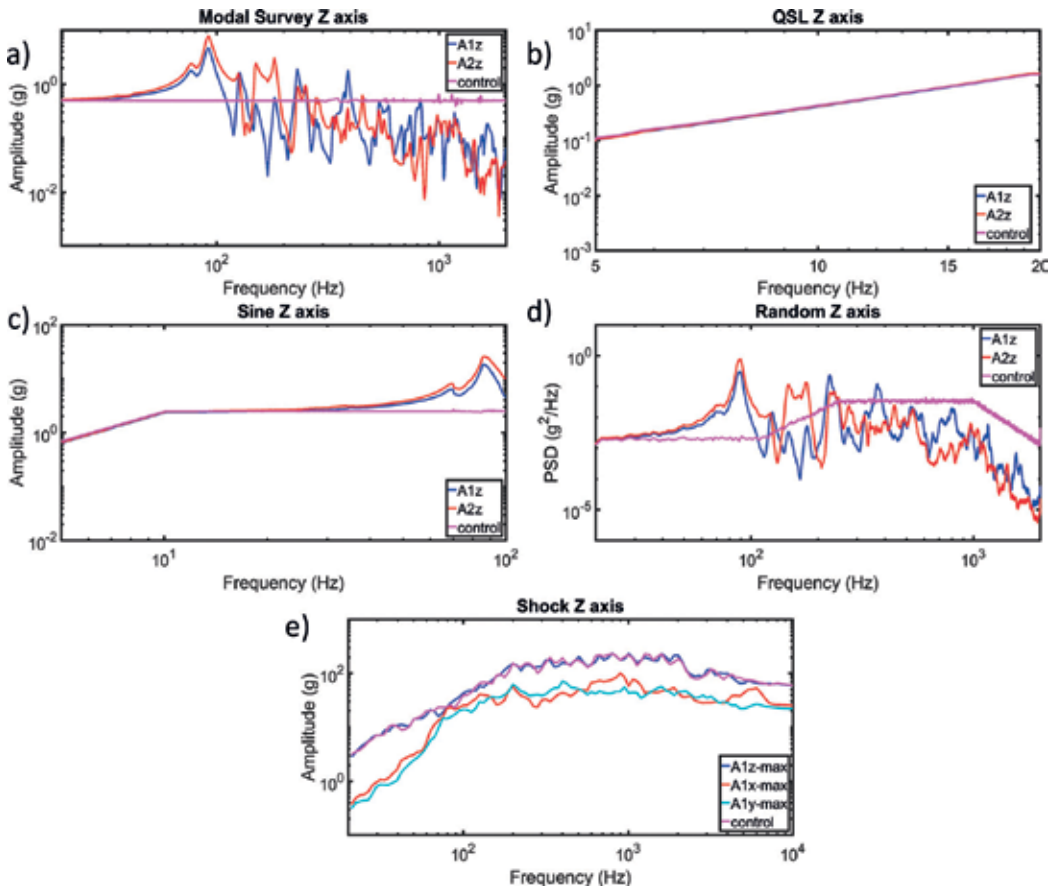

Figure 12. Results of the tests in the Y-axis. (a) Modal survey, (b) QSL, (c) sine vibration, (d) random vibration, and (e) shock.

3D-printed ULTEM™ structural model—modal survey results before and after the quasi-static load, sine, and random vibration tests in the Y-axis

	Pre-QSL	Post-QSL	Pre-sine	Post-sine	Pre-random	Post-random	Pre-shock	Post-shock
First modal freq. [Hz]	77.19	77.3	77.3	74.46	74.46	74.46	74.46	73.79
Observed deviation	0.14%		−3.70%		<0.1%		−0.90%	
Accel. peak [g]	1.79	2.12	2.12	1.7	1.7	1.67	1.67	1.64
Observed deviation	18.40%		−19.80%		−1.80%		−1.80%	

Table 4. Results of the modal survey tests before and after the QSL, sine, random vibration, and shock tests in the Z-axis.

and shock tests were done. As in the tests done in the X and Y axes, all the values are provided with the measurements of accelerometer 1 since the values provided by accelerometer 2 did not differ significantly.

http://dx.doi.org/10.5772/intechopen.79852

With the modal survey, all the modes were characterized. The first mode was located at 77.19 Hz. The amplitude of the first mode was 1.79 g. For comparison, the main mode of the structure manufactured by CNC in aluminum had a frequency of 354.45 Hz and had an amplitude of 4.00 g.

In the QSL test, the structure behaved perfectly between the margins defined by the control. The modal survey after this test showed that the first mode changed the frequency to 77.3 Hz (0.14%). The amplitude was increased to 2.12 g (18.40%). This represented no major changes in the structure but an increase in the stiffness.

The sine vibration test showed that the structural model entered in resonance at the frequency of the first mode. After this test, the first mode slightly changed the frequency to 74.46 Hz (3.70% lower) and reduced the amplitude to 1.70 g (at −19.80% less). This represented no major changes in the structure but an increase in the damping.

In the random vibration test, all the modes were excited. After the test, the first mode did not change (74.46 Hz). Its amplitude was reduced to 1.67 g (1.80% less).

In the shock vibration test, the structure behaved well. After the test, the first mode had a frequency of 73.79 Hz (0.90% less), and its amplitude was reduced to 1.64 g (1.80% less).

There were no significant changes in the structure, defined by shifts over 10% in the frequency of the first mode, before and after the tests. The visual analysis of the structure did not provide any change, which means that all the tests in this axis were successfully passed. Since the structure passed all the tests in all three axes, the structure was considered to be qualified to fly in the PSLV launcher.

3.3.1. Robustness test results

The robustness test was done with the random vibration test as the baseline due to its wider frequency range. First of all, the test level was raised up to the test specification provided by the GSFC General Environmental Verification Standard (GEVS) [13]. Following the same philosophy as for the regular test, a modal survey was carried out before and after the random test. An interactive process was started by increasing the load up step-by-step, with their corresponding modal surveys until a failure occurred. The levels of the robustness test can be seen in **Figure 13(a)**. The original profile of the PSLV random vibration test is represented in blue, the GEVS profile is represented in red, the extended profile of the second iteration is represented in magenta, and the profile at which the structure fails is represented in cyan.

Contrary to the expected failure by breaking a bolt by excessive shear stress, the failure was a combination of HeliCoil extractions by excessive traction stress and two cracks in one of the corners near the fixing point in contact with the shaker. Obviously, some bolts were bended after the failure as a side effect of the part cracks, but any of them was broken.

Figure 13(b) shows a comparison of the modal survey done before executing the test which modified the 3D-printed ULTEM™ structural model (blue signal) and after the execution of that random vibration test (red signal). The control signal is represented in magenta.

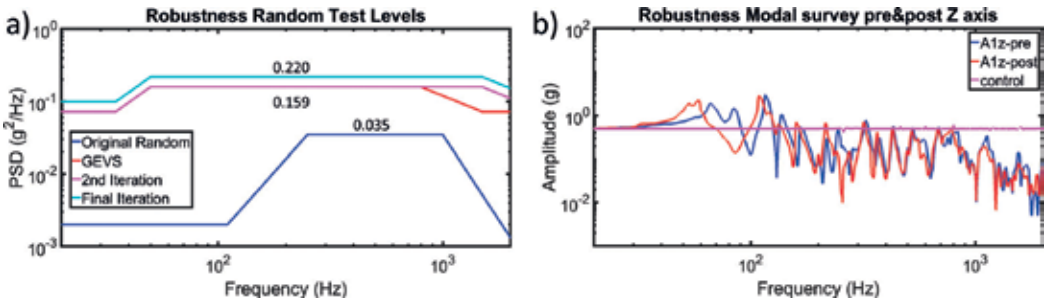

Figure 13. Robustness test levels and results. (a) Test level of the robustness test and (b) modal survey before and after the last random vibration test.

After the test the modes of the structural model are substantially shifted to the left, i.e., to lower frequencies: the first mode shifted from 53.10 to 66.19 Hz, which represented a change of 19.78% (clearly over 10%). The amplitude of the signal slightly changed from 1.95 g before the test to 1.91 after the test (2.05%). Besides, the shape of the signal also changed. After the test, the first and the second modes are nearer. This represents a significant change in the structure at the level of the test, and as conclusion, it is not passed. However, the structure was taken to the limit, which was much higher than the qualification levels.

4. Discussion

The 3D-printed ULTEM™ structural model widely fulfilled the requirements imposed by the PSLV launcher authority, which enables the technology tested to be used in space and more specifically in the functional structure of satellites.

By comparing the characteristics of the validated technology with respect to the classical CNC milling in aluminum alloy, the 3D-printed model presented a clearly different behavior. In **Figure 14**, the modal survey obtained in the two structural models was represented to facilitate comparison. There was a clear difference in the rigidity of the two materials with the same geometry. The 3D-printed model had natural modes with lower frequencies than the CNC structure in aluminum. This implies more flexibility and, as a result, larger displacements. Damages could be found if the structure is displaced, which would cause damages in the satellite components. Damages could also be found if the structure is impacted by an external item in the launcher. This result was expected as previous studies in the mechanical properties suggest a tensile modulus of 2 GPa for ULTEM™ parts made by FDM [14]. When this value is compared with aluminum typical value for tensile modulus (70 GPa), a simplified mass-spring model foresees a reduction in the first mode frequency of 80% which is coherent with the test results. In consequence the manufacturing flaws described in [14] do not have a remarkable impact in functional parts as the stiffness does not seem to be affected and the catastrophic fail was due to a stress concentration near the structure corners not to a manufacturing defect. In conclusion both the material and the manufacturing method have been proven to be valid for their use in primary structural application despite the local manufacturing flaws.

http://dx.doi.org/10.5772/intechopen.79852

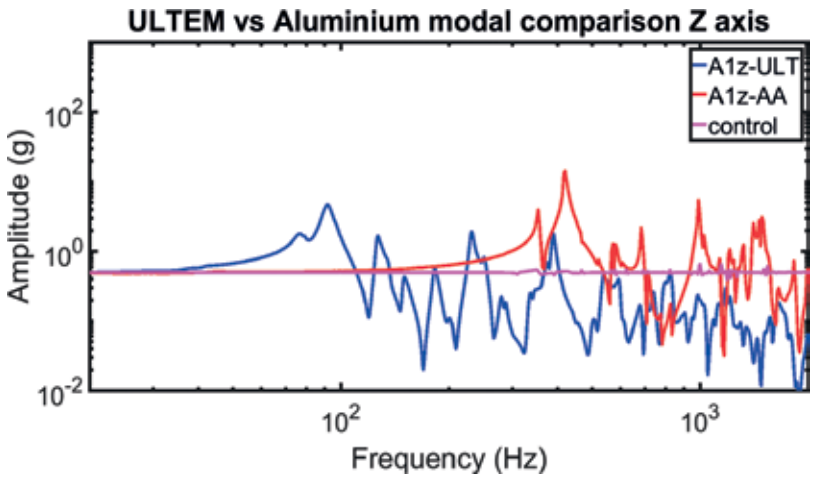

Figure 14. 3D-printed ULTEM™ structural model vs. CNC-milled aluminum structural model comparison.

In terms of damping, as can also be seen in **Figure 14**, the ULTEM™ model had a significant higher damping leading to a less sharp modal survey profile. This effect could be especially beneficial for all the electronic components inside the satellite as most of the vibration energy was dissipated by the structure, thus reducing the effective acceleration that those components could suffer. Primarily in the response to high frequency, associated with a higher energy, which can cause a higher damage in the electronic components such as relays or oscillators, this attenuation is desirable, and it can be considered as a thermoplastic structure advantage [15].

5. Conclusions

In this work, the structure of a satellite which was made in 3D-printed ULTEM™ was validated. A structural model with realistic mass dummies was tested under qualification levels established by the PSLV launcher authority. The tests were successfully passed, which indicate that the proposed structure was apt to be put in orbit.

Besides, the structure was compared with that manufactured with a classical CNC approach in aluminum alloy. The results indicate that the 3D-printed structure has less rigidity and more damping than the CNC aluminum structure. This can be beneficial for electromechanical components of the satellites since the ULTEM™ structure acts as a low-pass filter. However, it has larger displacements, which has to be considered in order to avoid impacts between components and external surfaces of the satellite.

In addition, during the experimentation of both the 3D-printed and the CNC-milled models, some ULTEM™ and aluminum powder were generated because of the stress caused by the trials. This powder generation and the effect that it could have over optical components in the satellite are still to be analyzed in depth. In addition, the thermal-vacuum cycling and atomic oxygen effects have to be studied before flying this structure in the space environment.

Acknowledgements

The research leading to these results has received funding from the Horizon 2020 Program of the European Union's Framework Programmes for Research and Innovation (H2020-PROTEC-2015) under REA grant agreement number 687500-ReDSHIFT (http://redshift-h2020.eu/).

Conflict of interest

This publication reflects only the author's views, and the European Commission is not liable for any use that may be made of the information contained therein.

Author details

Jonathan Becedas*, Andrés Caparrós, Antonio Ramírez, Pablo Morillo, Esther Sarachaga and Almudena Martín-Moreno

*Address all correspondence to: jonathan.becedas@elecnor-deimos.com

Elecnor Deimos Satellite Systems, Puertollano, Spain

References

[1] Messier D. What a ride to space costs these days. Parabolic Arc. 2017. Available from: http://www.parabolicarc.com/2017/08/18/ride-space-costs-days/ [Accessed: Jun 6, 2018]

[2] Gstattenbauer GJ. Cost comparison of expendable, hybrid, and reusable launch vehicles [thesis]. Ohio: Department of the Air Force, Air University, Air Force Institute of Technology, Wright-Patterson Air Force Base; 2004

[3] Spaceflight, Pricing information. 2018. Available from: http://spaceflight.com/schedule-pricing/#pricing [Accessed: Jun 6, 2018]

[4] Wassmer W. The materials used in artificial satellites and space structures. Azo Materials. 2015. Available from: https://www.azom.com/article.aspx?ArticleID=12034 [Accessed: Jun 6, 2018]

[5] Molitch-Hou M. Made In Space Begins 3D Printing PEI/PC on the ISS. Engineering.com. 2017. Available from: https://www.engineering.com/3DPrinting/3DPrintingArticles/ArticleID/15254/Made-In-Space-Begins-3D-Printing-PEIPC-on-the-ISS.aspx [Accessed: Jun 6, 2018]

[6] Mudarra M, Sellarès J, Cañadas JC, Diego JA. Sublinear dispersive conductivity in polyetherimides by the electric modulus formalism. IEEE Transactions on Dielectrics and Electrical Insulation. 2015;**22**(6):3327-3333

[7] ECSS Secretariat, ESA-ESTEC, Requirements & Standards Division. ECSS-E-ST-10-03C, Space Engineering-Testing, ESA Publications Division, Noordwijk, The Netherlands. Issue 2. Jun 1, 2012

[8] Yilmaz F, Haktanir OO, Uygur AB. Quasi-static structural test of satellites. In: 7th International Conference on Recent Advances in Space Technologies (RAST), Istanbul, Turkey: IEEE; 16–19 June, 2015

[9] Department of Space Indian Research Organisation. Polar Satellite Lauch Vehicle. Government of India. n.d. Available from: https://www.isro.gov.in/launchers/pslv [Accessed: Jul 6, 2018]

[10] ECSS Secretariat, ESA-ESTEC, Requirements & Standards Division. ECSS-E-ST-10-02C, Space Engineering-Verification, ESA Publications Division, Noordwijk, The Netherlands. Mar 6, 2009

[11] Roethlisberger G. Phase C Launch Environment, Ref.: S3-C-STRU-1-6-Launch Environment.doc. EPFL Lausanne Switzerland. 2008. Available from: http://www.goldstem.org/Swiss%20Cube/09%20-%20Structures%20and%20configuration/S3-C-STRU-1-6-Launch%20Environment.pdf [Accessed: Jul 6, 2018]

[12] 6U CubeSat Design Specification, The CubeSat Program, Cal Poly SLO, California, USA. 2016. Available from: https://static1.squarespace.com/static/5418c831e4b0fa4ecac1bacd/t/573fa2fee321400346075f01/1463 788288448/6U_CDS_2016-05-19_Provisional.pdf [Accessed: Jul 6, 2018]

[13] NASA Goddard Space Flight Center. General Environmental Verification Standard (GEVS) for GSFC Flight Programs and Projects. NASA Goddard Space Flight Center, Greenbelt, Maryland. 2013. Available from: https://standards.nasa.gov/standard/gsfc/gsfc-std-7000 [Accessed: Jul 11, 2018]

[14] Bagsik A, Schöppner V, Klemp E. FDM part quality manufactured with Ultem* 9085. In: 14th International Scientific Conference on Polymeric Materials. Martin-Luther-Universität Halle-Wittenberg, 15–17 September, Halle (Saale), Germany, Vol. 15. 2010. pp. 307-315

[15] Veprik AM, Babitsky VI. Vibration protection of sensitive electronic equipment from harsh harmonic vibration. Journal of Sound and Vibration. 2000;**238**(1):19-30

Section 3

Surface and Printing Advanced Testing

Chapter 5

Density Functional Theory (DFT) as a Powerful Tool for Designing Corrosion Inhibitors in Aqueous Phase

Dakeshwar Kumar Verma

Additional information is available at the end of the chapter

http://dx.doi.org/10.5772/intechopen.78333

Abstract

In the current chapter, recent progress has been described in the field of computational quantum chemistry for the development of corrosion inhibitors. The current chapter is divided into several sections and subdivisions. Recently, the development of green and sustainable technologies for corrosion prevention is highly desirable an increase in ecological awareness and strict environmental regulations. In the last decade, the use of quantum calculation based corrosion inhibitors study has attracted considerable attention. Quantum calculation based density function theory (DFT) has been widely accepted as "green corrosion inhibition technique" because of its theoretical based work. DFT can be used to design corrosion inhibitors to prevent corrosion on mild steel, aluminum, copper, zinc, and magnesium in aqueous media. DFT is the simplest way to study the molecular structure and behavior of corrosion inhibitors. Various quantum chemical parameters such as dipole moment (μ), energy difference (ΔE), softness (σ) and global hardness (η), highest occupied molecular orbital (E_{HOMO}) and lowest occupied molecular orbital (E_{LUMO}), etc., of corrosion inhibitors has been calculated using software in order to elucidate the adsorption and corrosion inhibition behavior of inhibitor molecules.

Keywords: adsorption, corrosion inhibition, aqueous solution, metals, DFT

1. Introduction

The damage on the material by corrosion produces not only for the high cost inspection, repair, and replacement, but in addition to these formation of a public risk, thus the need for the development of the novel Substances that treat acid in particular, like corrosion inhibitors Media [1]. The use of corrosion inhibitor molecules is one of the most practical ways to protect the materials against corrosion, and it is becoming increasingly popular in industrial applications.

The atmosphere is affected by various metals and their alloys strikes due to the use of acid like H_2SO_4 and HCl for various industrial processes (acid pickling, oil well-acidification, chemical clean-up, etc.) [2, 3], for these reasons the inhibitors is employed as one of the most practical ways to conserve corrosion. Traditionally, corrosion inhibition performance is evaluated experimentally, such as gravimetric analysis, potentiodynamic polarization, and electrochemical impedance spectroscopy (EIS). However, these experimental methods are expensive and laborious, and often decrease in the illuminating corrosion mechanism. With the improvements in software and hardware, computer simulation has become a powerful tool to investigate the complex system of corrosion resistance [4]. By checking the structure, electron distribution, and adsorption of molecules on the metal and oxide surfaces, the corrosion mechanism is now deeply detected. In 1971, Vosta and Eliasek [5] introduced quantum chemical methods to investigate the prohibition of corrosion and established the field of quantum corrosion electrochemistry. After this, the main objective of quantum chemistry methods was primarily on the discovery and establishment of relations between molecular structure and prohibition, and many valuable results have now been reported. Quantum chemical study has proven itself very long ago useful in determining the structure of the molecules, the reaction as well as the obvious electronic structures [6]. Thus, it has become a common practice to calculate quantum chemical corrosion study concept of assessment of efficiency a corrosion inhibitors with the help of computational chemistry using chemicals to find compounds with desired properties intuition and experience in a mathematical quantitative and a relation between the structure once computerized and activity or property are found, any number of compounds. Those who have not been synthesized so far can be easily tested planning of computational method [7] and a set of mathematical equations that are capable of displaying correctly chemical incident under study [8, 9].

2. Principles of corrosion

Thermodynamic and electrochemical are two basic principles of corrosion mechanism which describe the transformation of metals and alloys into their stable states like hydroxides, sulfates, oxides and chlorides, etc.

2.1. Thermodynamic principles

Thermodynamics directs the spontaneous direction of a chemical reaction and it is used to determine whether the corrosion on metal surface is theoretically possible or not [10].

2.2. Electrochemical principles

Basically corrosion is the coupled of two half-cell electrochemical reaction, cathodic and anodic reaction. Anodic reaction involves the leaving of free electron by metal ionization however cathodic reaction involves the up taking of free electrons by dissolved oxygen and/or water molecules in the solution. Previous is oxidation type reaction where free electrons are produced while later is reduction reaction in which electrons can be accepted [11]. Corrosion behavior of metals and alloys can be easily determine using electrochemical principles.

http://dx.doi.org/10.5772/intechopen.78333

Two half-cell reaction can be divided in to following type as given:

2.2.1. Anodic reaction

Anodic reaction is the loss of metal cations as given in examples:

$$\mathrm{Fe(s)} \rightarrow \mathrm{Fe^{2+}(aq)} + 2\mathrm{e}- \tag{1}$$

$$\mathrm{Zn(s)} \rightarrow \mathrm{Zn^{2+}(aq)} + 2\mathrm{e}- \tag{2}$$

$$\mathrm{Cu(s)} \rightarrow \mathrm{Cu^{2+}} + 2\mathrm{e}- \tag{3}$$

Each of the above reactions in Eqs. (1)–(3) is an anodic reaction because there is increase in oxidation number and loss of electrons from metals at the anodic site.

2.2.2. Cathodic reaction

Reduction of cation(s) from free electrons of oxidation reaction is a cathodic reaction. Formation of hydrogen gas (H_2) from the reduction of two hydrogen ions at metal surface is an example of cathodic reaction (Eq. (4)):

$$2\mathrm{H^{+}(aq)} + 2\mathrm{e}- \rightarrow \mathrm{H_2(g)} \tag{4}$$

Above reactions are shown schematically in **Figure 1**.

2.2.3. Coupled electrochemical reactions

Figure 2 represents coupled electrochemical reactions in which anodic and cathodic reactions exist on the metal surface at different places. There are four different types of conditions causes to corrosion are: (i) an anodic reaction, (ii) a cathodic reaction, (iii) a metallic path between these two reactions, and (iv) electrolyte. Electrolyte is an ionic aqueous solution in which

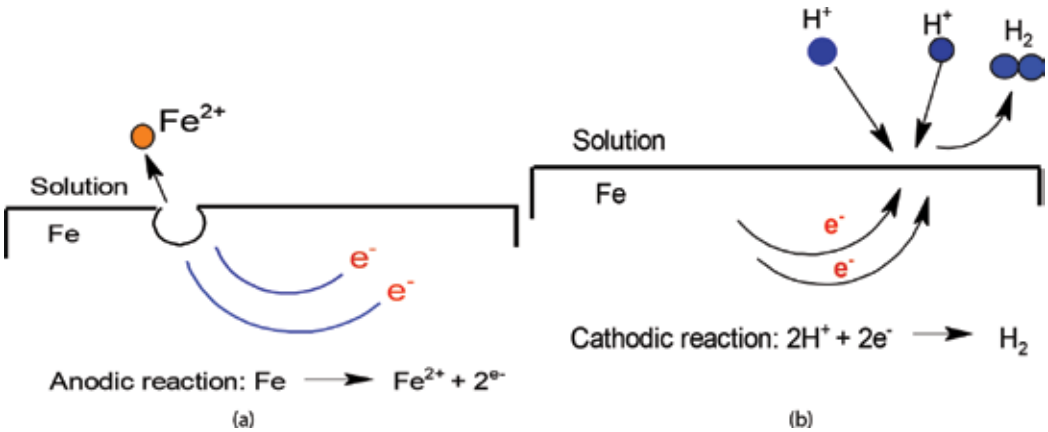

Figure 1. (a) Anodic reaction and (b) cathodic reaction in metal/solution interface.

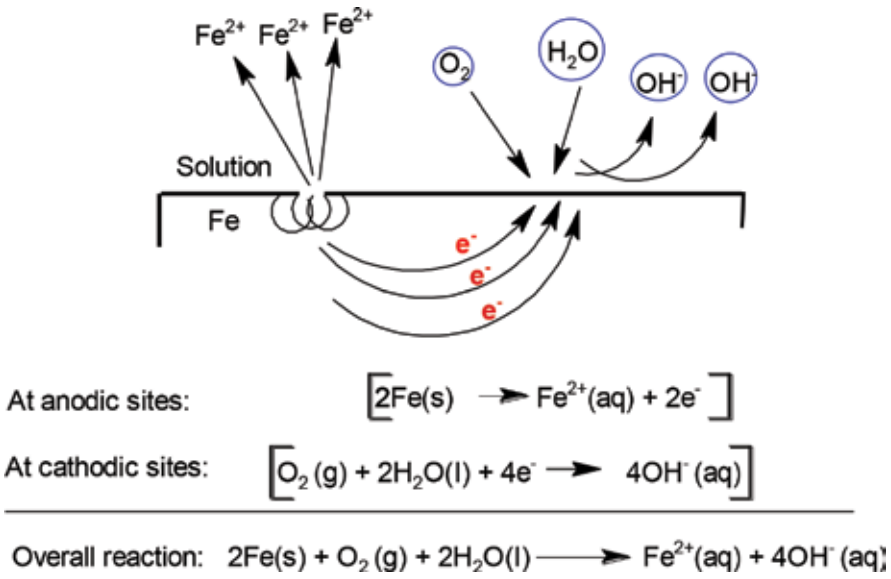

Figure 2. Coupled reactions occurring on the metal surface at different sites for iron in a neutral or basic medium.

current can be flow. The coupled reaction for an iron metal dipped in neutral, acidic or basic medium is illustrated in **Figure 2**.

Heterogeneous nature of a metal surface is reason for the orientation of coupled reaction on the same metal surface. Heterogeneity on metal surface can be arise due to defects like screw, steps, dislocation, point defects and kink sites, etc.

3. Adsorption mechanism of corrosion

Corrosion inhibition properties of metals and alloys can significantly change due to adsorption of inhibitor molecules at metal/solution interface. Inhibition of metal corrosion is a surface phenomenon which involves the adsorption of corrosion inhibitors over the metal surface in electrolytic solution. In corrosive solution inhibitor molecules adsorbed on the metal surface by replacing the H_2O molecules at the metal/solution interface according to the given process Eq. (5) [12]:

$$\mathrm{Inh}_{(\mathrm{sol})} + n\mathrm{H_2O}_{(\mathrm{ads})} \rightarrow \mathrm{Inh}_{(\mathrm{ads})} + n\mathrm{H_2O}_{(\mathrm{sol})} \tag{5}$$

where Inh $_{(ad)}$ and Inh $_{(sol)}$ are inhibitor molecules in the corrosive medium and adsorbed on the metal surface, respectively, whereas n is the number of H_2O molecules replaced by the molecules of inhibitor. The values of surface coverage (θ) have been used to elucidate the different isotherm to determine the adsorption process at metal/solution interface. The different adsorption isotherms can be characterized by the mathematical models as given in Eqs. (6)–(8) [13]:

$$\left(\frac{C}{\theta}\right) = \log K_{ads} - g\theta \tag{6}$$

$$\frac{C}{\theta} = \frac{1}{K_{ads}} + C \tag{7}$$

$$log\left(\frac{\theta}{(1-\theta)C}\right) = \log K_{ads} - g\theta \tag{8}$$

where θ is the surface coverage, K_{ads} is adsorption constant and C is the equilibrium concentration.

4. Consequences and economics of corrosion

Corrosion is a global problem, which adversely affects the development of both developed and developed countries. According to a highly cited study conducted by the National Association of Corrosion Engineers (NACE) in 1998, the total annual cost of corrosion in the U.S. is estimated at US $ 276 billion, which is approximately 3.1% GDP (GDP; NACE 2002) [14]. In 2011, the total cost of corrosion in the US increased to $ 2.2 trillion. Since the cost of corrosion in India is a matter of concern, it is about two lakh crores (US $ 45 billion) proposed by the 1st Global Corrosion Summit held in New Delhi in 2011 [15]. However, these estimates are outdated and recently the NACE is being closely examined at the cost of the corrosion, according to which the annual global cost of the corrosion is approximately $ 2.5 trillion, which is equivalent to 3.4% of the global GDP. In India, the cost of annual corrosion is more than 100 billion US dollars, whereas in South Africa, direct corrosion costs are estimated to be around 130 billion (i.e., 9.6 billion US dollars) [16, 17]. By applying the existing methods of prevention of corrosion, this cost of the war can be reduced by 35% (US $ 875 billion) to 15% (US $ 375 billion).

Corrosion is a global problem, which adversely affects the development of both developed and developed countries. According to a highly cited study conducted by the National Association of Corrosion Engineers (NACE) in 1998, the total annual cost of corrosion in the U.S. is estimated at US $ 276 billion, which is approximately 3.1% GDP (GDP; NACE 2002) [5]. In 2011, the total cost of corrosion in the US increased to $ 2.2 trillion. Since the cost of corrosion in India is a matter of concern, it is about two lakh crores (US $ 45 billion) proposed by the 1st Global Corrosion Summit held in New Delhi in 2011 [6]. However, these estimates are outdated and recently the NACE is being closely examined at the cost of the corrosion, according to which the annual global cost of the corrosion is approximately $ 2.5 trillion, which is equivalent to 3.4% of the global GDP [7, 8].

In India, the cost of annual corrosion is more than 100 billion US dollars, whereas in South Africa, direct corrosion costs are estimated to be around 130 billion (i.e., 9.6 billion US dollars) [7, 8]. By applying the existing methods of prevention of corrosion, this cost of the war can be reduced by 35% (US $ 875 billion) to 15% (US $ 375 billion).

5. Basics and computational aspects of density function theory (DFT)

5.1. The basics of DFT: Hohenberg-Kohn theorem

In Moscow, at the Frumkin Institute of Electrochemistry of the Russian Academy of Sciences, the scientific school of Quantum Electrochemistry was to be started in Revaz Dogonadze in the 1960s. Generally, the ideas that are generated in the field include quantum mechanics, electrodymamics, and electrochemistry; and likewise a very large group of different professional academics is studied. The fields of expertise include chemicals, physics, mechanical and electrical engineering. More specifically, quantum electrochemical electrode surfaces [18] for the study of electrochemical processes, quantum mechanical devices such as DFT are used, including the transfer of electrons from the molecules to the metal electrode surface.

In some previous studies, the basis and importance of DFT [19, 20] has been described. The recent impact of DFT in the development of quantum electrochemistry is significant, and can be linked to achievements in the late 1980s when hybrid functional and gradient-corrected methods were introduced [21]. Based on the famous Hohenberg-Kohn theorem awarded the Nobel Prize in physics for his work on DFT in 1964. DFT concentrates on electron density ρ(r), itself as the carrier of all information in form and/or molecule ground state, rather than an electron wave function, one per electron occurs. In summary, the Hohenberg-Kohn theorem establishes that the base of an electronic system only electronic density is functional. In principle, only need to calculate the electron density in all the properties of the system. In DFT, the ground state total energy for an N-electron system is expressed in terms of the external potential v(r) and the three-dimensional ground-state electronic density ρ(r) in the form (Eq. (9)) [22]:

$$E[\rho] = F[\rho] + \int dr\rho(r)v(r), \tag{9}$$

where $F[\rho]$ is the generalized functional of Hohenberg-Kohn given by the sum of the electronic kinetic energy functional as given in Eq. (10):

$$N = \int dr\rho(r), \tag{10}$$

Eq. (10) pledges the proper normalization of the electron density.

A general DFT formula is given as Eq. (11) [23]:

$$E_{DFT}[\rho] = T_s[\rho] + E_{ne}[\rho]\, J[\rho]\ E_{xc}[\rho], \tag{11}$$

where E_{ne} is the electron-nuclear attraction functional, T_s is the kinetic energy functional, *Exc* denotes the exchange correlation functional and *J* is the Coulomb part of the electron-electron repulsion functional. The dependency of each of these terms on the electron density, ρ, is characterized by ρ in brackets following all term.

5.2. Basis sets

The base set, the mathematical description of the orbital within the system used to do theoretical calculations. By putting a low restriction on the location of electrons in large base space,

they make a more accurate orbital estimate. When molecular calculation is done, it is common to use sophisticated finite numbers based on the atomic orbitals cantered on each atomic nucleus within this molecule. Most molecular quantum mechanical methods begin calculating with the choice of a set of base functions. The use of a substantial base set for the success of calculation is a mandatory requirement. Standard basis for electronic computation calculation uses linear combinations of geosynchronous functions of set orbit. In order to accurately represent atomic orbitals, we should use a linear combination of several codgers. Gaussian offers a wide range of predefined base sets, which can be categorized from those numbers and types of works, in which they are included.

5.3. Basic parameters derived from DFT and their application to corrosion inhibition design

5.3.1. Frontier molecular orbitals

The frontier orbitals are very important in defining the lowest unoccupied molecular orbital (LUMO) and highest occupied molecular orbital (HOMO) of molecules. Scientist Fukui [24] recognized the importance of the frontier orbitals of first time because the stereochemistry of the inhibition system and the chemical reactions were key factors in the governing of ease of reaction. A good relationship has been found between E_{HOMO} and corrosion resistance, which is often associated with the electron-sensitivity potential of the molecule. It is well known that the adsorption of the inhibitor on the surface of the metal may be on the basis of donor-acceptable interaction between the heteroatom electrons and/or π electrons and the vacant *d*-orbitals of the metal surface atoms [25]. A high value of E_{HOMO} is likely to indicate the electron donating tendency of the molecule to the vacant orbitals of acceptor molecules whereas the energy of the lower empty orbit shows the electron acceptor ability of the molecule(s). Regarding the value of the interval energy, $\Delta E = E_{LUMO} - E_{HOMO}$, the big values of energy difference mean less reactivity of a chemical species. Good inhibition efficiency will be provided in low values of energy difference, because to reduce the energy from the previously occupied orbital, there is less to donate in the correct orbital of the metal [26].

5.3.2. Dipole moment

The dipole moment is a vector quality which is most extensively used for describing the polarity of a molecule. It is a measurement of the separation of the two opposite electrical charges (positive and negative) and represented as given in Eq. (12) [27]:

$$\mu = q\ R \tag{12}$$

Where μ is a dipole moment, R is the distance between two different charges and q is the extent of the different charge. The dipole moment is applied to the distribution of electrons among the two bonded atoms. The existence of dipole moment, the difference between non-polar and polar bonds is different. With pure dipole moment, the molecule is zero or very small, bond and molecules are considered non-polar and polar molecules with pure bipolar moment. Atoms with similar electronegative values, they produce chemical bonds with very small dipole moment. Total dipole moment, however, reflects only the global prohibition of polarity

of a molecule instead of a single bond notice that the efficiency of inhibitor molecules has decreased with decreasing efficiency. The dipole moment of inhibitors [28] therefore, positive signals of coefficient of μ indicate that the inhibitors can be applied to the metal surface by the physical mechanism [29]. Obot and Obi-Egbedi [30] found a high correlation (0.999) between corrosion inhibition and dipole moment efficiency of benzimidazole and its derivatives; namely, 2-mercaptobenzimidazole and 2-methylbenzimidazole using DFT. The obtained result shows that 2-mercaptobenzimidazole, which has the highest value of dipole moment, exhibits the higher inhibition efficiency. The adsorption strength increase as high value of the dipole moment between the inhibitor molecules and the metal surface.

5.3.3. Electronegativity and the electronic chemical potential

DFT has been found to be successful in providing insight into chemical reactivity and selectivity, in terms of global molecular properties, such as chemical potential ($-\mu$) and electronegativity (χ) [31]. Thus, for an N-electron system with an external potential v(r) and total electronic energy (E) the chemical potential, has been defined as the first derivative of the E with respect to N at constant v(r) as in Eq. (13) [32]:

$$\chi = -\mu = -\left(\frac{\partial E}{\partial N}\right)_{v(r)} \tag{13}$$

According to Iczkowski and Margrave [33], it should be noted that, when assuming a quadratic relationship between E and N and in a finite difference approximation, than it can be written as represented in Eqs. (14) and (15):

$$\chi = -\mu\left(\frac{I+A}{2}\right) \tag{14}$$

$$\chi = -\frac{E_{\mathrm{HOMO}} + E_{\mathrm{LUMO}}}{2} \tag{15}$$

where A and I have the electron affinity and ionization potential, respectively, due to which the electronegative definition of Mulliken can be corrected [34]. In addition, a theoretical justification was provided for the theory of Sanderson's equation of electronegativity, which states that when two or more atoms join together to form a molecule, then their electro negativities is the same intermediate the value is adjusted from [35].

5.3.4. Global hardness and softness

There is total hardness (H) and softness properties, which also facilitate analysis of molecular selectivity and reaction. Correlation between quantum chemical quantities and corrosion inhibition is based on Pearson's hard and soft acids and bases, and the Lewis theory of acid and base [36]. Energy gap, ΔE (i.e., energy difference between E_{LUMO} and E_{HOMO}) also provides information about the reaction of inhibitor molecules. A hard molecule has a high value of ΔE denotes the hard nature of molecules, whereas a soft molecule is a small ΔE. Due to small ΔE value electrons can be easily supplied to acceptor system from soft molecules in comparison to

hard molecule. Hence, the reactive site of the molecule may be absorbed, where, σ has the highest value [37]. For the calculations of quantum chemical parameters, global hardness (Eq. (16)) and softness (Eq. (17)) the following equations can be used [38]:

$$\gamma = \frac{E_{HOMO} - E_{LUMO}}{2} \tag{16}$$

The reverse of the global hardness is written as the softness, σ has given in Eq. (17):

$$\sigma = \frac{1}{\gamma} \tag{17}$$

5.3.5. Mulliken population analysis

To identify the adsorption centers of inhibitors, Mulliken population analysis has been widely reported [39, 40]. All chemical interactions are either covalent or polar (electrostatic). Electric charge in the molecule is obviously responsible for electrostatic interaction. Local electron charge or density is important in the properties of many physical-chemical and chemical reactions of biological molecules. Thus, charge-based parameters have been widely employed as weak intermolecular interaction measures or as chemical reactive indices. Mulliken population analysis [41] is mostly used to calculate the charge distribution in a molecule. These numerical quantities are easy to obtain and provide at least a qualitative understanding of structural reactions of blocking molecules [42]. In addition, atomic charge is used to describe molecular polarization of molecules.

*5.3.6. The fraction of electrons transferred (Δ*N)

The fraction of electrons transferred (Δ*N*) has been calculated as given in Eq. (18) [43]:

$$\Delta N = -\frac{\chi_{M} + \chi_{inh}}{[2\,(\eta_m + \eta_{inh})]} \tag{18}$$

where $\chi_{inh\ and}$ χ_M and indicate the absolute electronegativity of the inhibitor molecule and metal, respectively. However η_{inh} and η_M denote the absolute hardness of the inhibitor molecule and metal. Usually, Δ*N* exhibits the inhibition efficiency generated from the electrons transferred, inhibitor molecule to the iron atom. According to Lukovitt et al. [44] if the value of Δ*N* is less than 3.6, then the inhibition efficiency of the inhibitor molecules increasing with electron releasing ability on metal surface. Improve electron releasing power, was replaced by electron-donating substance (—OCH_3 group) by altering a hydrogen atom of the phenyl ring, as in the case of MPTS, which was to improve the prohibition, but on the other hand, a decreasing effect has been observed by electron-attracting group (—Cl) in the case of CPTS.

6. Some recent studies of corrosion inhibitor using density function theory

DFT is widely used software designing new corrosion inhibitors of chemical compounds using energy of the highest occupational molecular orbital (E_{HOMO}) energy, the energy of the lowest

unoccupied molecular orbital (E_{LUMO}), ΔE (energy difference), dipole moment (μ), Mulliken population analysis, electronegativity and electronic chemical capacity (χ), global hardness (γ) and softness (σ), the transfer of electrons (ΔN) and molecular polarization potential are most important electronic parameters. As mentioned by some previous researchers [45–47], excellent corrosion inhibitors are usually those compounds that accept electrons from the metal as well as offer electrons in the empty orbital(s) of metal.

During the last two decades, computational methods have been developed as important tools in the corrosion resistance, because in the calculation, large amounts of compounds can be provided in large amounts within a reasonable time frame. The results of such studies can be further used as an appropriate starting point for experimental studies. Computational methods can also be important tools in the development of more suitable compounds used for metal protection, starting with the already available compounds and by identifying derivatives with better metal protection efficiencies through structural modifications. Recently, there are many studies in literature on computational studies of useful organic materials for metal protection. The goal of these studies is to gain insights at the molecular level on the contact of these organic matters with metal surfaces. This important approach is particularly important in the design of new and effective corrosion inhibitors for industrial applications in oil and gas fields. A recent review of some of the research has been given below. They are not enough anywhere because excellent reviews are available elsewhere [48].

6.1. Organic corrosion inhibitors studied using DFT

Using the semi-experimental AM1 method, Mahendra et al. [49], studied the inhibition efficiency of benzimidazole derivatives. Quantum chemical parameters such as E_{HOMO}, E_{LUMO}, ΔE, the fraction of electron transferred (ΔN), dipole moment (μ), and global hardness (γ) and softness (σ) were calculated, which detected a steric hindrance effect of molecules on inhibition efficiency, which was discussed. According to the results obtained (**Table 1**), E_{HOMO} was the most statistically significant term that influenced the inhibition efficiency. The more E_{HOMO}, the more prohibited efficiency was seen experimentally. Hyperchm 8.0 software was used for the use of detailed Quantum Chemical Study program package for the Inh I, Inh II, and Inh III. The experimental abilities of quantum chemical calculation and inhibitors were subject to correlation analysis. Based on HOMO and LUMO energy, HOMO and LUMO coefficients, polarizability, and Mulliken population analysis, it was concluded that considering a parameter is not enough and the synthesis of better corrosion inhibition can be achieved by controlling all the electronic properties and parameters of a selected group of molecules.

Quantum chemical calculation of commercially available drug namely grieseofulvin was calculated towards the corrosion inhibition potential of mild steel using Gaussian 9.0 software package [50]. Quantum chemical parameters has confirmed that the presence of heteroatoms and π electrons increases resistance towards corrosion of the surface of mild steel, which means that the inhibitor shows better inhibition efficiency against metal surface in aqueous solution. Various quantum chemical parameters such as energy gap (ΔE), E_{HOMO}, E_{LUMO}, dipole moment (μ) and hardness (γ) of drug molecule (**Figure 3**) has been evaluated to determine its corrosion inhibition efficiency and corresponding values are depicted in **Table 2**.

http://dx.doi.org/10.5772/intechopen.78333

Inhibitors	E_{HOMO}(eV)	E_{LUMO}(eV)	ΔE (eV)	σ (eV)	μ (D)	ΔN (e)	η (eV)
Inh I	−8.8459	0.7865	8.0594	0.2462	3.2029	0.2709	4.0297
Inh II	−8.7028	0.7392	7.9636	0.2497	3.4714	0.2896	4.1194
Inh III	−8.6541	0.7069	7.9472	0.2516	5.0267	0.2918	3.9735

Table 1. Quantum chemical parameters for the benzimidazole derivatives.

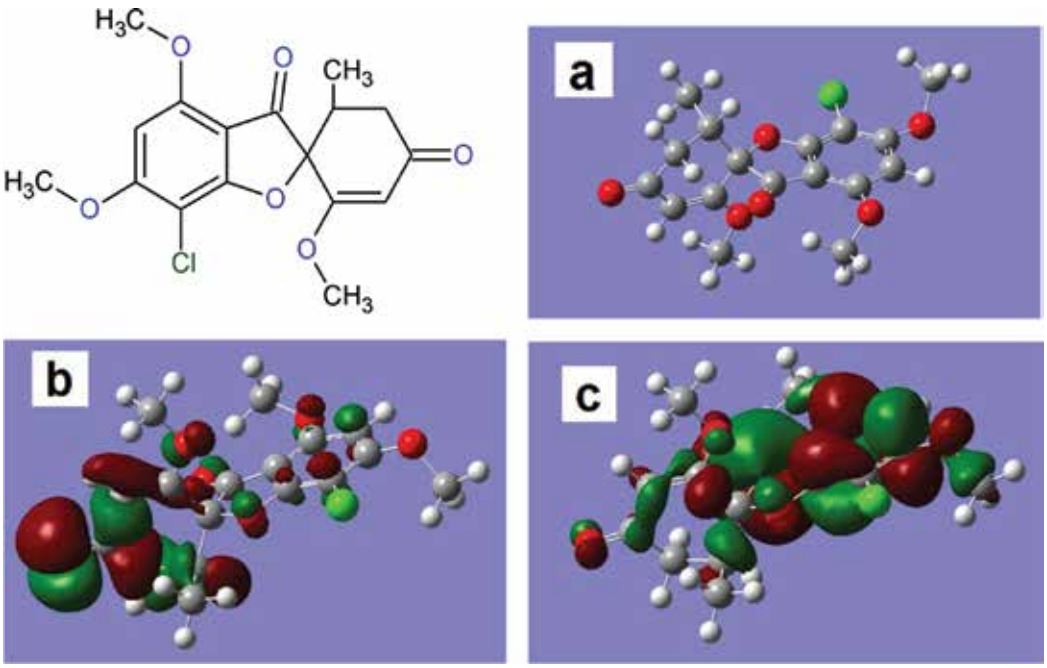

Figure 3. Molecular structure of griseofulvin with the (a) the optimized structure, (b) LUMO and (c) HOMO structures.

All parameters exhibited that griseofulvin acts as a good corrosion inhibitor towards mild steel in HCl solution.

Verma et al. [51] describes the effect of ring and ring size of three 3-amino alkylated indoles (AAIs) namely, N-((1H-indol-3-yl)(phenyl)methyl)-N-ethylethanamine (AAI-1), 3-(phenyl (piperidin-1-yl)methyl)-1H-indole (AAI-3) and 3-(phenyl(pyrrolidin-1-yl)methyl)-1H-indole (AAI-2) on mild steel corrosion acidic solution using experimental as well as theoretical calculations such as quantum chemical calculations and molecular dynamics simulations methods. Experimental results revealed that the inhibition efficiency increases with increased concentration of the corrosion inhibitors. Maximum inhibition efficiencies of 94.34% for AAI-1, 96.08% for AAI-2 and 96.95% for AAI-3 were obtained at 0.862 mM concentrations of inhibitors. Both experimental and theoretical calculations show that 3-amino alkylated indole with cyclic amino groups exhibit high corrosion inhibition efficiency compared with open-chain amino groups. Experimental results explains that resistance efficiency increases with increased

Inhibitor	E_{HOMO} (eV)	E_{LUMO} (eV)	ΔE (eV)	μ (eV)	Υ
Griseofulvin	−0.0423	−0.0059	0.0364	3.2396	0.0182

Table 2. Quantum chemical parameters for the griseofulvin.

concentration of the inhibitors. Maximum inhibition efficiency of 94.34% for AAI-1, 96.08% for AA-II and 96.95% for AAI-3 was obtained in 0.862 mm concentrations of inhibitor. Quantum chemical calculations such as dipole moment (μ), E_{HOMO}, E_{LUMO}, ΔE, the fraction of electron transferred (ΔN), global electronegativity (χ), and global hardness (γ) and softness (σ) were calculated. Optimized structure, E_{HOMO} and E_{LUMO} of inhibitors are shown in **Figure 4** and calculation values are given in **Table 3**.

6.2. Plant extracts based corrosion inhibitors studied using DFT

Emeka et al. [52] studied the Inhibition efficiency of green and sustainable biomass extract of *capsicum* on mild steel in acidic solution. Capsaicin (**Figure 5a**) is the major phytoconstituents of capsicum, whose quantum calculation has been studied extensively. Chemical computations of Capsaicin were performed using the S-Mulliken Population Analysis through the DFT electronic structure program DML^3 [40–43]. Various quantum chemical parameters like E_{HOMO}, E_{LUMO}, ΔE, dipole moment (μ), global hardness (γ), softness (σ) and Fukui functions have been studied extensively. Investigation correlation between experimental and quantum chemical calculations and inhibition efficiency was discussed at this work.

Anupama et al. [53] examine the *Phyllanthus amarus* leaf extract (PAE) as the mild steel corrosion inhibitor in 1 M HCl. Weight loss, EIS and PDP techniques used to investigate corrosion behavior of PAE under various exposure time and temperature and successfully correlated with different parameters of quantum chemical analysis. Since extracting components are adsorbed on metal surface, inhibitive efficiency increases as concentrations increased and finally reached up to >90%. Computational calculations corresponding to phyllanthin (**Figure 5b**) a major component of PAE was made in order to understand the involvement of the component in the inhibition efficiency of the plant extract. Quantum chemical parameters; ΔE, E_{LUMO}, E_{HOMO}, dipole moment (μ), the fraction of electron transferred (ΔN), global hardness (γ) and softness (σ) and global electronegativity (χ) were calculated and stabilized the effect of structural features on the electron donating ability of major component phyllanthin of PAE.

Raja et al. [54] investigated Isoreserpiline (**Figure 5c**) as active molecule against corrosion protection of mild steel. Isoreserpiline is the major component of leaves and bark extracts of *Ochrosia oppositifolia*. Quantum calculation shows that the density (HOMO and LUMO) of ISR is located within the vicinity of the aromatic indole moiety. This study shows that π electron cloud of ring and lone pair on nitrogen atom of indole ring have high electron donating ability to metal surface. This can be well correlated with FTIR analysis that shows the coordination of ISR with the mild steel surface through electron rich moieties of indole ring. An ideal corrosion inhibitor can be donated electrons in metal surface through HOMO, as well as obtaining

http://dx.doi.org/10.5772/intechopen.78333

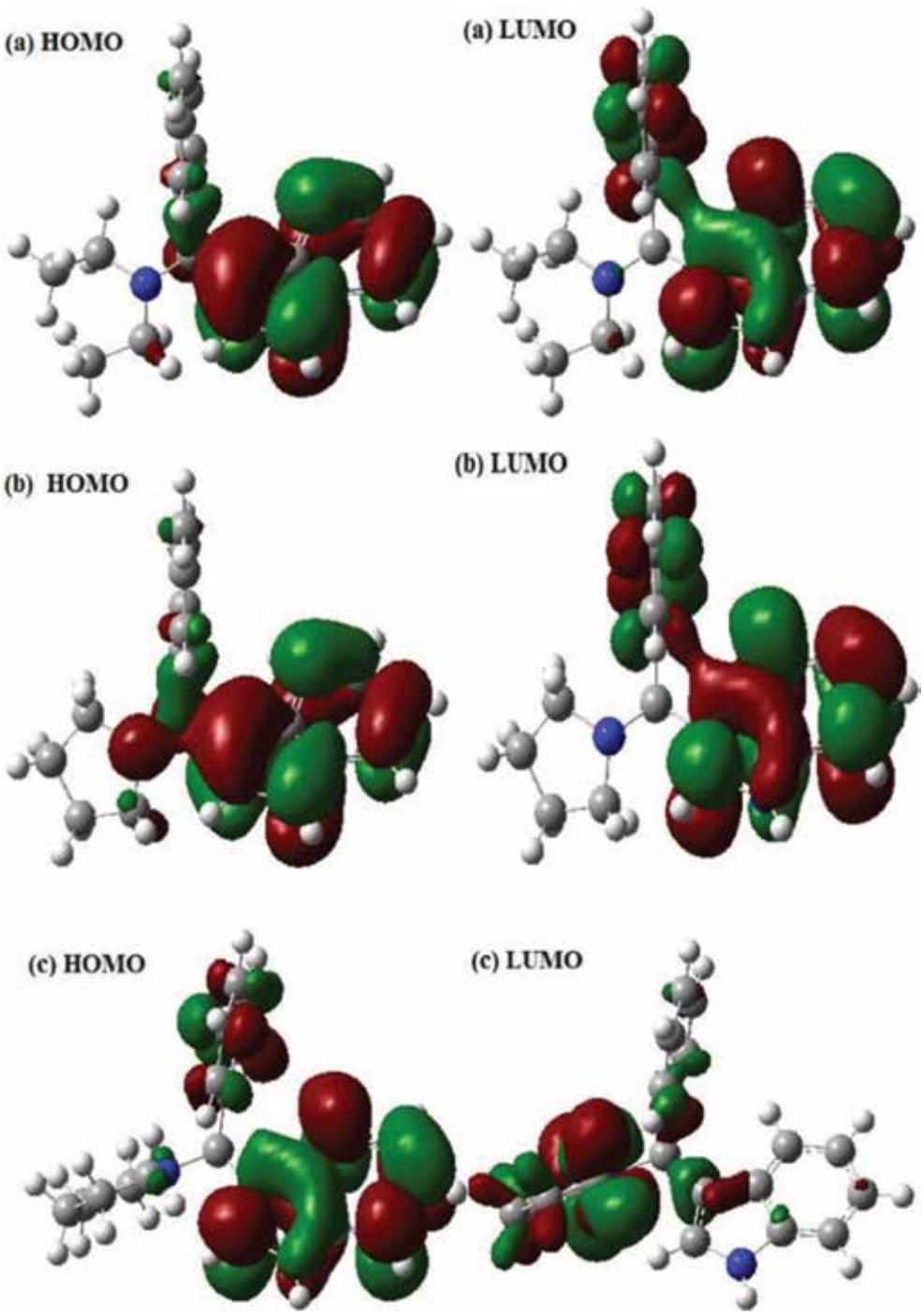

Figure 4. The frontier molecular orbital (left-hand side: HOMO; and right-hand side: LUMO) of the studied inhibitor APQDs derivatives (a) AAI-1, (b) AAI-2, and (c) AAI-3 [reprinted with permission].

Inhibitors	μ	E_{HOMO}	E_{LUMO}	ΔE	η	σ	χ
AAI-1	1.6927	−8.5748	−5.1214	3.4534	1.7267	0.57913	6.8481
AAI-2	1.9680	−8.5262	−5.2214	3.4504	1.7252	0.57964	6.8376
AAI-3	2.3671	−7.8036	−5.1236	2.6800	1.3350	0.74903	6.4636

Table 3. Quantum chemical parameters of inhibitors resultant from the B3LYP/6-31+G(d,p) method.

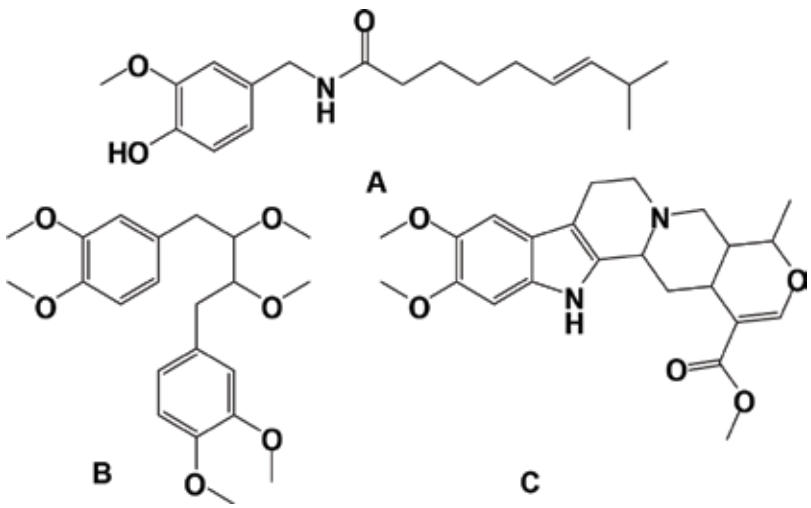

Figure 5. Molecular structure of (A) capsicum, (B) phyllanthin, and (C) Isoreserpiline.

electrons via LUMO through metal surfaces (Fe through Fe^{2+}, Fe^{3+} conversion) or bind mild steel surface strongly, which states that the ISR can donate and accept electrons through induction movement. On the other hand quantum calculation represents the energy level E_{HOMO}, E_{LUMO} and ΔE ($E_{HOMO} - E_{LUMO}$) for iron and inhibitor molecule. ΔE for ISR −0.3083 EV was found, which was more (less negative) than FE^{2+} and Fe^{3+} (−1.2178 and − 2.0712 EV); While E_{LUMO} values were found in ISR Fe, Fe^{2+} and Fe^{3+}. This result indicates that ISR can donate electrons to MS surface but in turn, MS cannot obtain donation electron from the surface. Quantum chemical analysis well supported the result of FTIR analysis and evidenced the possibility of electron transfer from inhibitor molecules to mild steel.

7. Future developments

Density functional theory (DFT) has become an attractive theoretical method, because it provides accurate, basic and important parameters for at least complex and molecules cost. Apart from this, by implementing the DFT methodology, we can understand reactionary behavior conditions of hard and soft acid/base (HSAB) principles that provide a systematic way interrupter/analysis of surface interaction and prediction. Survey of theoretical corrosion literature

presented in chapter (Sections 6.1 and 6.2) shows that density function theory (DFT) is a powerful tool to study fundamental, molecular-level processes regarding the corrosion barrier. However, it should be very careful with these calculations, these studies should be taken in planning can easily lead with inaccurate or inadequate data-sets for the wrong findings. Role of quantum chemistry in corrosion focus is likely to increase in future inhibitory studies moves towards the investigation of complex chemical mechanisms. However, due to high computational effort restrictions calculations mean that there will be no quantum chemical methods be able to replace experimental corrosion in the near future less expensive methods of study or computerized procedures regarding the corrosion inhibition.

8. Conclusion

This chapter focuses on the use of modern quantum chemical methods, primarily to describe the adsorption of corrosion-resistant molecules on a metal surface in the aqueous solution as the functional principle of density. It is evident that DFT can be used as powerful technique with a unique ability to make practical calculations on many complex bodies system, such as large organic molecules, drugs, ionic liquids those are widely used as inhibitor. Hydrophobic/hydrophilic nature of corrosion inhibitor has been identified as an important factor in determining the ability of the resistant to prevent corrosion. Finally, the idea of an important future in the design of new and effective corrosion inhibitors using DFT will identify organic structures, which have less toxicity besides having high corrosion protection capacity.

Acknowledgements

Author greatly acknowledges Dr. (Mrs) Fahmida Khan and Dr. R.N. Singh, Principal Govt. Digvijay College Rajnandgaon for their support.

Author details

Dakeshwar Kumar Verma

Address all correspondence to: dakeshwarverma@gmail.com

Department of Chemistry, Government Digvijay Autonomous Postgraduate College, Rajnandgaon, Chhattisgarh, India

References

[1] Singh AK. Inhibition of mild steel corrosion in hydrochloric acid solution by 3-(4-((Z)-indolin-3-ylideneamino) phenylimino) indolin-2-one. Industrial and Engineering Chemistry Research. 2012;**51**:3215-3223

[2] Verma DK, Khan F. Corrosion inhibition of mild steel in hydrochloric acid using extract of glycine max leaves. Research on Chemical Intermediates. 2016;**42**:3489-3506

[3] Verma DK, Khan F. Green approach to corrosion inhibition of mild steel in hydrochloric acid medium using extract of spirogyra algae. Green Chemistry Letters and Reviews. 2016;**9**(1):52-60

[4] Khaled KF, Amin MA. Dry and wet lab studies for some benzotriazole derivatives as possible corrosion inhibitor for copper in 1.0 M HNO_3. Corrosion Science. 2009;**51**:2098-2106

[5] Vosta J, Eliasek J. Study on corrosion inhibition from aspect of quantum chemistry. Corrosion Science. 1971;**11**:223-229

[6] Abdallah M, Asghar BH, Zaafarany I, Fouda AS. The inhibition of carbon steel corrosion in hydrochloric acid solution using some phenolic compounds. International Journal of Electrochemical Science. 2012;**7**:282-304

[7] Khaled MI. Evaluation of cysteine as environmentally friendly corrosion inhibitor for copper in neutral and acidic chloride solutions. Electrochimica Acta. 2007;**52**:7811-7819

[8] Oguzie EE, Li Y, Wang FH. Effect of surface nanocrystallization on corrosion and corrosion inhibition of low carbon steel: Synergistic effect of methionine and iodide ion. Electrochimica Acta. 2007;**52**:6988-6996

[9] Jing-Mao Z, Jun L. Corrosion inhibition performance of carbon steel in brine solution containing H_2S and CO_2 by novel Gemini surfactants. Acta Physico-Chimica Sinica. 2012; **28**(3):623-629

[10] Saha SK, Dutta A, Ghosh P, Sukul D, Banerjee P. Adsorption and corrosion inhibition effect of Schiff base molecules on the mild steel surface in 1 M HCl medium: A combined experimental and theoretical approach. Physical Chemistry Chemical Physics. 2015;**17**: 5679-5690. DOI: 10.1039/C4CP05614K. PMID: 25623363

[11] Hussin MH, Kassim MJ. Inhibitive properties, thermodynamic and quantum chemical studies of alloxazine on mild steel corrosion in H_2SO_4. Corrosion Science. 2011;**53**:263-275. DOI: 10.1016/j.corsci.2010.09.020

[12] Quraishi MA, Sudheer. 2-Amino-3, 5-dicarbonitrile-6-thio-pyridines: New and effective corrosion inhibitors for mild steel in 1 M HCl. Industrial and Engineering Chemistry Research. 2014;**53**:2851-2859

[13] Verma CB, Lgaz H, Verma DK, Ebenso EE, Bahadur I, Quraishi MA. Molecular dynamics and Monte Carlo simulations as powerful tools for study of interfacial adsorption behavior of corrosion inhibitors in aqueous phase: A review. Journal of Molecular Liquids. 2018; **260**:99-120

[14] NACE. Materials Performance. Conference proceeding of CORCON. Special Issue, July, Houston, Texas, USA; 2002

[15] Confederation of Indian Industry. Conference proceeding. 1st Global Corrosion Summit. New Delhi, India; 2011

[16] Sharma SK. Green Corrosion Chemistry and Engineering: Opportunities and Challenges. 1st ed. German: Wiley-VCH Verlag GmbH & Co. KGaA; 2012

[17] Koch GH, Brongers MPH, Thompson NG, Virmani YP, Payer JH. Corrosion costs and preventative strategies in the United States. Materials Performance. 2002;**42**:1-156

[18] Dogonadze RR. Theory of molecular electrode kinetics. In: Hush NS, editor. Reactions of Molecules at Electrodes. London: Inter Science Pub; 1971. pp. 135-227

[19] Geerlings P, De Proft F, Langenaeker W. Conceptual density functional theory. Chemical Reviews. 2003;**103**:1793-1873

[20] Nagy A. Density functional theory and application to atoms and molecules. Physics Review. 1998;**298**:1-79

[21] Becke AD. Density functional calculations of molecular bond energies. The Journal of Chemical Physics. 1986;**84**:4524-4529

[22] Bell S, Dines TJ, Chowdhry BZ, Withnall R. Computational chemistry using modern electronic structure methods. Journal of Chemical Education. 2007;**84**(8):1364-1370

[23] Parr RG, Donnelly RA, Levy M, Palke WE. Electronegativity: The density functional viewpoint. The Journal of Chemical Physics. 1978;**68**:3801-3807

[24] Fukui K. Role of frontier orbitals in chemical reactions. Science. 1982;**218**:747-754

[25] Khalil N. Quantum chemical approach of corrosion inhibition. Electrochimica Acta. 2003; **48**:2635-2640

[26] Bentis F, Traisnel M, Vezin H, Hildebrand HF, Lagrenee M. 2,5-Bis(4 dimethylaminophenyl)-1,3,4-oxadiazole and 2,5-bis(4 dimethylaminophenyl)-1,3,4-thiadiazole as corrosion inhibitors for mild steel in acidic media. Corrosion Science. 2004;**46**:2781-2792

[27] Atkins P, De Paula J, editors. Atkins Physical Chemistry. 8th ed. New York: Oxford; 2006

[28] Gao G, Liang C. Electrochemical and DFT studies of b-amino-alcohols as corrosion inhibitors for brass. Electrochimica Acta. 2007;**52**:4554-4559

[29] Bouklah M, Benchat N, Aouniti A, Hammouti B, Benkaddour M, Lagrenee M, Vezin H, Bentiss F. Effect of the substitution of an oxygen atom by Sulphur in a pyridazinic molecule towards inhibition of corrosion of steel in 0.5 M H_2SO_4 medium. Progress in Organic Coating. 2004;**51**:118-124

[30] Obot IB, Obi-Egbedi NO. Theoretical study of benzimidazole and its derivatives and their potential activity as corrosion inhibitors. Corrosion Science. 2010;**52**:657-660

[31] Mendoza-Huizar LH, Rios-Reyes CH. Chemical reactivity of atrazine employing the Fukui function. Journal of the Mexican Chemical Society. 2011;**55**(3):142-147

[32] Chermette H. Chemical reactivity indexes in density functional theory. Journal of Computational Chemistry. 1999;**20**:129-154

[33] Iczkowski RP, Margrave JL. Electronegativity. Journal of the American Chemical Society. 1961;**83**:3547-3551

[34] Mulliken RS. A new electroaffinity scale; together with data on valence states and on valence ionization potentials and electron affinities. The Journal of Chemical Physics. 1934;**2**:782-793

[35] Sanderson RT. Chemical Bonds and Bond Energy. New York: Academic; 1976

[36] Ogretir C, Mihci B, Bereket G. Quantum chemical studies of some pyridine derivatives as corrosion inhibitors. THEOCHEM. 1999;**488**:223

[37] Huang W, Tan Y, Chen B, Dong J, Wang X. The binding of antiwear additives to iron surfaces: Quantum chemical calculations and tribological tests. Tribology International. 2003;**36**:163

[38] Gece G, Bilgic S. Molecular-level understanding of the inhibition efficiency of some inhibitors of zinc corrosion by quantum chemical approach. Industrial and Engineering Chemistry Research. 2012;**51**:14115-14120

[39] Sahin M, Gece G, Karei E, Bilgic S. Experimental and theoretical study of the effect of some heterocyclic compounds on the corrosion of low carbon steel in 3.5% NaCl medium. Journal of Applied Electrochemistry. 2008;**38**:809-815

[40] Ozcan M, Karadag F, Dehri I. Interfacial behavior of cysteine between mild steel and sulphuric acid as corrosion inhibitor. Acta Physico-Chimica Sinica. 2008;**24**(8):1387-1392

[41] Murrell JN, Kettle SF, Tedder JM. The Chemical Bond. Chichester: John Wiley & Sons; 1985

[42] Grüber C, Buss V. Quantum-mechanically calculated properties for the development of quantitative structure-activity relationships (QSAR'S). pKA values of phenols and aromatic and aliphatic carboxylic acids. Chemosphere. 1989;**19**:1595-1609

[43] Yurt A, Ulutas S, Dal H. Electrochemical and theoretical investigation on the corrosion of aluminium in acidic solution containing some Schiff bases. Applied Surface Science. 2006; **253**:919-925

[44] Lukovits I, Klaman E, Zucchi F. Corrosion Inhibitors—Correlation between Electronic Structure and Efficiency. Corrosion. 2001;**3**:57

[45] El-Ashry ES, Senior SA. QSAR of lauric hydrazide and its salts as corrosion inhibitors by using the quantum chemical and topological descriptors. Corrosion Science. 2011;**53**:1025-1034

[46] Lesar A, Milošev I. Density functional study of the corrosion inhibition properties of 1,2,4 triazole and its amino derivatives. Chemical Physics Letters. 2009;**483**:198-203

[47] Gece G, Bilgiç S. Quantum chemical study of some cyclic nitrogen compounds as corrosion inhibitors of steel in NaCl media. Corrosion Science. 2009;**51**:1876-1878

[48] Gece G. The use of quantum chemical methods in corrosion inhibitor studies. Corrosion Science. 2008;**50**:2981-2992

[49] Yadav M, Kumar S, Sinha RR, Behera D. Experimental and quantum chemical studies on corrosion inhibition performance of benzimidazole derivatives for mild steel in HCl. Industrial and Engineering Chemistry Research. 2013;**52**(19):6318-6328. DOI: 10.1021/ie400099q

[50] Verma DK, Khan F, Verma CB, Susai R, Quraishi MA. Experimental and theoretical studies on mild steel corrosion inhibition by the grieseofulvin in 1M HCl. European Chemical Bulletin. 2017;**6**(1):21-30

[51] Verma CB, Quraishi MA, Ebenso EE, Obot IB, El Assyry A. 3-amino alkylated indoles as corrosion inhibitors for mild steel in 1M HCl: Experimental and theoretical studies. Journal of Molecular Liquids. 2016;**219**:647-660

[52] Oguzie EE, Oguzie KL, Akalezi CO, Udeze IO, Ogbulie JN, Njoku VO. Natural products for materials protection: Corrosion and microbial growth inhibition using Capsicum frutescens biomass extracts. ACS Sustainable Chemistry & Engineering. 2013;**1**:214-225

[53] Anupama KK, Ramya K, Joseph A. Electrochemical and computational aspects of surface interaction and corrosion inhibition of mild steel in hydrochloric acid by Phyllanthus amarus leaf extract (PAE). Journal of Molecular Liquids. 2016;**216**:146-155

[54] Raja PB, Fadaeinasab M, Qureshi AK, Rahim AA, Osman H, Litaudon M, Awang K. Evaluation of green corrosion inhibition by alkaloid extracts of Ochrosia oppositifolia and isoreserpiline against mild steel in 1M HCl medium. Industrial and Engineering Chemistry Research. 2013;**52**(31):10582-10593. DOI: 10.1021/ie401387s

Edited by Aidy Ali

This book covers recent advances in the method used in testing, especially in the case of structural integrity that includes fatigue and fracture tests, vibrations test and surface engineering tests that are extremely crucial and widely used by engineers and industries.

The book will provide you with information on how to apply the advanced formulation, advanced theory and advanced method of testing that are relevant to all engineering fields: mechanical, electrical, civil, materials and surface engineering. The topics are explained comprehensively, including the reliable test that one should perform in order to effectively investigate the strength and validation of the developed theory or model.

I hope that the material is not too theoretical and that the reader finds the case study, formulation, testing method and the analysis helpful for tackling their own engineering and science based studies.

Published in London, UK

IntechOpen

ISBN 978-1-83881-780-0